Thomas Solberg

Dynamic Response Analysis of a Spar Type Floating Wind Turbine

Master's thesis

Trondheim, June 2011

Norwegian University of Science and Technology
Engineering Science and Technology
Marine Technology
NTNU

NTNU
Norwegian University of
Science and Technology

NTNU
Norwegian University of
Science and Technology

Dynamic Response Analysis of a Spar Type Floating Wind Turbine

Thomas Solberg

Marine Technology
Submission date: June 2011

Supervisor:	Torgeir Moan
	Bjørn Skaare
Co-supervisor:	Zhen Gao
	Madjid Karimirad

Norwegian University of Science and Technology

NTNU Trondheim
Norwegian University of Science and Technology
Department of Marine Technology – Group of Marine Structures

MSC THESIS IN MARINE TECHNOLOGY

SPRING 2011

FOR

STUD.TECHN. Thomas Solberg

DYNAMIC RESPONSE ANALYSIS OF A SPAR TYPE FLOATING WIND TURBINE
(Dynamisk responsanalyse av en flytendevindturbin av Spar type)

Background

There is a significant potential for offshore wind energy. In deeper water it may be most cost effective to exploit this potential by using floating wind turbines. Various floating wind turbine concepts have been suggested. However it is currently no possible to demonstrate which is the best concept. Moreover the relevant concept would depend upon the water depth and environmental conditions.

The purpose of this project work is therefore to contribute information about a specific concept and contribute to a comparative study made by fellow MSc candidates in order to shed light on the relative performance of various floating wind turbine concepts.

Project tasks
The aim of this project is generally to establish a dynamic model of a wind turbine for assessing the energy production and responses relevant for assessing the structural integrity of the turbine.

1. **Introductory literature study of wind turbines**
   Review relevant literature including methods to determine the response of the wind turbine subjected to wind and wave loads; including relevant second-order sum-or difference-frequency wave loads. The software system Simo/Riflex serves as basis for the analysis.

2. **Establishing the dynamic model and load model**
   A dynamic model involving buoyancy, mass, mooring system etc should be established based on a reference model.

   The mooring system may be carried out by integrating Simo with Riflex for coupled mooring analysis. Alternatively simple springs might be used to model the mooring system. (A comparison of these alternatives would be of interest).

   The wave and wind induced loads should be modelled. A dll version of Simo should be used to model the wind force as function of wind speed at then nacelle.

3. **Validation or verification of the model**

The natural frequencies of the relevant modes of the concept should be estimated and compared with those of the reference model. Possible discrepancies should be explained. If necessary, the model should be adjusted.

Other simple checks of the model based on idealized load cases should be carried out.

4. Case study

Based on some relevant operational and survival load cases analyses should be carried out. Since these load cases should serve as basis for comparison of the three concepts the same cases should be considered. and decided in a "project" meeting. Since a comparison with Jonkman's results is also interesting Jonkman's report serves as reference for selecting load cases.

A sensitivity study should be performed to study e.g. the effect of statistical uncertainty inherent in the sampling of stochastic loads, water depth; flexibility of the tower and possible other parameters

5. Conclude and recommend further work.

The work scope could be larger than anticipated. Subject to approval from the supervisor, topics may be deleted from the list above or reduced in extent.

In the thesis the candidate shall present his personal contribution to the resolution of problem within the scope of the thesis work.

Theories and conclusions should be based on mathematical derivations and/or logic reasoning identifying the various steps in the deduction.

The candidate should utilize the existing possibilities for obtaining relevant literature.

The thesis should be organized in a rational manner to give a clear exposition of results, assessments, and conclusions. The text should be brief and to the point, with a clear language. Telegraphic language should be avoided.

The thesis shall contain the following elements: A text defining the scope, preface, list of contents, summary, main body of thesis, conclusions with recommendations for further work, list of symbols and acronyms, reference and (optional) appendices. All figures, tables and equations shall be numerated.

The supervisor may require that the candidate, in an early stage of the work, present a written plan for the completion of the work. The plan should include a budget for the use of computer and laboratory resources that will be charged to the department. Overruns shall be reported to the supervisor.

The original contribution of the candidate and material taken from other sources shall be clearly defined. Work from other sources shall be properly referenced using an acknowledged referencing system.

The thesis shall be submitted in two copies:

- Signed by the candidate
- The text defining the scope included

- In bound volume(s)
- Drawings and/or computer prints which cannot be bound should be organized in a separate folder.

Prof. Torgeir Moan
Supervisor at NTNU

Dr.Bjørn Skaare
Supervisor at Statoil

In addition dr. Zhen Gao and Mr. Madjid Karimirad serve as co-supervisors.

Deadline: June 2011

Referanser

1) Jonkman J.M. Dynamics of offshore fl oating wind turbines—model development and verifi cation. Wind Energy 2009; 12: 459–492.

2) Jonkman, J.M. and D. Matha Dynamics of offshore floating wind turbines—analysis of three concepts, Wind Energy, on-line.†

Abstract

Wind power is a large natural source for renewable energy, and many countries have shown interest in establishing floating offshore wind parks. There are many advantages with floating offshore wind turbines, but also many challenges connected to them.

This report focuses on establishing a model for wave-wind induced loading on a Spar type floating wind turbine named OC3-Hywind. The OC3-Hywind is a modified version of an original design developed by Statoil. Two fellow MSc students have developed models for a tension leg platform (TLP) and a semi-submersible, and a comparison between the three concepts have been done.

The model has been constructed by the use of the well known software tools HydroD and DeepC. In addition, a DLL extension, TDHMILL3d, was used to obtain thrust force. HydroD was used in calculations of the hydrodynamic coefficients of the floater. DeepC was used to run coupled floater and mooring analysis in time domain.

Important parameters like hydrodynamic coefficients and natural frequencies compare well to data from the literature. Simulations showed that the Spar is mostly influenced by wind loads in the operational conditions. At rated wind speed of 11.4 m/s the pitch motions of the Spar was showed to be large. To reduce these motions a simple filter was used to extend the turbine control system. In situations where wind and waves have different directions, the Spar experiences large yaw motions. Several factors that may contribute to these motions have studied. To achieve good accuracy in statistical parameters, 10 or more simulations with different seeds were needed.The original depth of 320 m was changed to 160 m. Only minor changes to the mooring system were needed to obtain similar performance as the base case.

In the comparison part typical trends of the different floaters was studied. Based on these trends, positive and negative response characteristics were discovered. The semi-submersible had the largest pitch and surge motions, while the TLP had the largest accelerations below rated. This may result in difficulties in maintenance operations. Only the Spar showed sign of excessive yaw motions. The semi-submersible had the lowest nacelle accelerations and STD for all load cases. In addition, the semi-submersible is the most versatile when it comes to water depth.

Preface

This master's thesis was conducted during my final semester of the five year Master of Science program in Marine Technology. The work has been carried out at the Department of Marine Technology at the Norwegian University of Science and Technology, under the supervision of Professor Torgeir Moan and Dr. Bjørn Skaare. Dr. Zhen Gao and Dr. Madjid Karimirad have served as co-supervisors.

I would like to thank everyone for our interesting and educational meetings during the semester. They have been most valuable. I would also like to thank Professor Torgeir Moan and Dr. Bjørn Skaare for the supervision of my project, and for providing me with an interesting and challenging topic. I also want to show my gratitude to Dr. Zhen Gao for his guidance and welcoming atmosphere whenever needed. Thanks also go out to my parents who have always been very supporting and interested in me as a person and in whatever I have done. My girlfriend, Silje Nicander Nilsen, has also given me enormous support during this semester. I really appreciate it!

Trondheim, June 16, 2011

Thomas Solberg

Contents

List of Figures

List of Tables

Nomenclature

Symbol	Description
$a_{ij}(\omega)$	Frequency dependent part of the added-mass coefficients
A	Disc area of simplified rotor model
A_k	Wave amplitude of regular wave component k
A_l	Wave amplitude of regular wave component l
$A_{ij}(\omega)$	Added-mass coefficients
$A_{\infty,ij}$	Frequency independent part of the added-mass coefficients
A_0	Initial cross sectional area
$b_{ij}(\omega)$	Frequency dependent part of the potential damping
$B_{ij}(\omega)$	Potential damping coefficients
$B_{\infty,ij}$	Frequency independent part of the potential damping coefficients
$B_{Radiation}$	Damping contribution from radiation in the 1-DOF system
$B_{Viscous}$	Damping contribution from viscous effects in the 1-DOF system
B_x	Total damping contribution of the 1-DOF system
$\mathbf{C}$	Structural damping matrix
C_{dn}	Drag coefficient on mooring lines, normal direction
C_{dt}	Drag coefficient on mooring lines, tangential direction
C_D	Drag coefficient for floater
$C_{ij}^{Hydrostatic}$	Hydrostatic restoring matrix
C_n	Configuration n

C_T	Thrust coefficient
C_0	Initial configuration
d	Element diameter
D	Diameter of the floater
$\mathbf{dF}_s^{Viscous}$	Viscous drag force on a strip
D_s	Morrison strip diameter
dz	Length of differential strip
E	E-modulus
f	Frequency
$F_i^D(t)$	Diffraction load vector
F_i^{Gyro}	Forces on the floater from gyro effect
F_i^{Hydro}	Hydrodynamic load vector
$F_i^{Inertia}$	Inertia load vector
F_i^{Lines}	Mooring line load vector
$F_i^{Platform}$	Platform load vector
F_i^R	Radiation load vector
$F_i^{Restoring}$	Restoring load vector
$F_i^{Structural}$	Total structural load vector
F_i^{SV}	Slowly varying drift forces
$\overline{F}_i^{SV}$	Mean value of slowly varying drift forces
$F_i^{Viscous}$	Viscous drag force on the floater
$F_i^{Waves,(1)}$	1st order wave excitation forces
$F_i^{Waves,(2)}$	2nd order wave excitation forces
F_i^{wind}	Wind induced forces
$\overline{F}_i^{(2)}$	Total mean drift force
F_n	Drag force normal to the line element
F_t	Tangential friction force
F_{Total}^R	Total retardation force

F_W^L	Wind force vector in local body coordinate system
F_W^{Rot}	Wind force vector in the local rotor coordinate system
g	Gravitational constant
h	Water depth
$h_i^D(\tau)$	Transfer function
$h_{ij}(\tau)$	Retardation function
$H(s)$	Transfer function
H_s	Significant wave height
I	Intensity of the wind turbulence
I_{ij}	Moment of inertia
$I_{x,r}$	Rotor moment of inertia about the x axis
k	Wave number
$\mathbf{K}$	Mooring line stiffness matrix
KC	Keulegan carpenter number
L	Length mooring line element after deformation
L_{HH}	Distance from origin to hub in 1-DOF system
L_k	Length scale parameter
L_x^{Rot}	Angular momentum in the local rotor coordinate system
L_0	Initial stress free length
m	Total weight of platform and tower
$\mathbf{M}_{Gyro}^{Rot}$	Gyro moment in local rotor coordinate system
M_{ij}	Rigid body mass matrix
M_W^L	Moments around the origin of the local body coordinate system due to wind
N	Normal force in mooring element
p	Pressure
p_a	Ambient pressure
Re	Reynolds number
s	Imaginary plane

$S(\omega_k)$	Wave spectrum
$S_{Pitch}(\omega)$	Pitch spectrum
S_w	Cross-sectional wetted surface
$S_w(f)$	Wind speed spectrum
$S_{Wave}(\omega)$	Wave spectrum
$S_{Wind}(\omega)$	Wind spectrum
$S_{Yaw}(\omega)$	Yaw Spectrum
S_0	Water plane area at the still water level
t	Time
T	Thrust force
T_{lk}^{ic}	2nd order transfer function for the difference frequency loads
T_{lk}^{is}	2nd order transfer function for the difference frequency loads
T_n	Natural period of degree of freedom n
T_p	Peak period
$T_{SP:i}$	Natural period for the spar in DOF i
$T_{SS:i}$	Natural period for the semi-submersible in DOF i
$T_{T:i}$	Natural period for the tension leg platform in DOF i
$T_{transient}$	Transient period
T_0	Thrust at a linearized point
u	Parcel velocity
u_1	Wind speed downstream
$\mathbf{v_s}$	Water particle velocity
V	Mean wind speed
V_{Hub}	Mean wind speed at the hub
V_{rel_x}	Relative water velocity in local element x direction
V_{rel_y}	Relative water velocity in local element y direction
V_{rel_z}	Relative water velocity in local element z direction
$\mathbf{V_r^{Rot}}$	Hub velocity in the local rotor coordinate system

$\mathbf{V}_{\mathbf{rel}}^{\mathbf{Rot}}$	Relative velocity in the local rotor coordinate system
V_W	Total displace volume in still water
V_w^{Rot}	Wind velocity in the local rotor coordinate system
V_0	Wind speed upstream
w	Parcel velocity
x_r^L	Vector from the origin of the local body coordinate system to the local rotor coordinate system
x	Coordinate in body-fixed coordinate system
$\dot{x}$	Hub translation velocity in 1-DOF system
x^{Rot}	Coordinate in rotor-fixed coordinate system
x_G	x-coordinate to the centre of gravity
$\dot{\mathbf{X}}_\mathbf{s}$	Strip velocity
y	Coordinate in body-fixed coordinate system
y^{Rot}	Coordinate in rotor-fixed coordinate system
y_G	y-coordinate to the centre of gravity
z	Coordinate in body-fixed coordinate system
z^{Rot}	Coordinate in rotor-fixed coordinate system
z_B	Vertical coordinate to the centre of buoyancy
z_G	z-coordinate to the centre of gravity

Greek symbols

Symbol	Description
α_1	Inertia proportional damping coefficient
α_2	Stiffness proportional damping coefficient
β	Wave direction
ε	Strain
ε_k	Wave phase angle of regular wave component k

ε_l	Wave phase angle of regular wave component l
ϕ_0	Velocity potential
φ	Phase angle
γ	Peakedness parameter of Jonswap spectrum
λ	Parameter in Kaimal spectrum
ρ_a	Air density
ρ_w	Water density
ζ	Free surface elevation
ζ_n	Damping coefficient
ζ_a	incident wave amplitude
ζ_D	Damping coefficient in the denominator of notch filter transfer function
ζ_n	Modal damping ratio for degree of freedom n
ζ_N	Damping coefficient in the nominator of notch filter transfer function
θ	Angle defined in Figure 12
θ_D	Angle defined in Figure 12
θ_N	Angle defined in Figure 12
η_1	Surge
η_2	Sway
η_3	Heave
η_4	Roll
η_5	Pitch
η_6	Yaw
$\dot{\eta}_j$	Rigid body velocity
$\ddot{\eta}_j$	Rigid body acceleration
τ	Dummy integration variable
σ	Stress
σ	Scaling factor
σ_W	wind speed standard deviation

$\boldsymbol{\omega}_B^{Rot}(t)$	Angular velocity of body in local body coordinate system
ω	Wave frequency
ω_d	Damped natural frequency
ω_k	Wave frequency of regular wave component k
ω_l	Wave frequency of regular wave component l
ω_{n_5}	Natural frequency in heave
ω_r	Rotor spin at angular speed
$\omega_{SP:i}$	Natural frequency for the spar in DOF i
$\omega_{SS:i}$	Natural frequency for the semi-submersible in DOF i
$\omega_{T:i}$	Natural frequency for the tension leg platform in DOF i
ω_0	Corner frequency of the notch filter
ω_{160m}	Natural frequency of spar at 160 m depth
ω_{320m}	Natural frequency of spar at 320 m depth
ω_+	ω_0 increased with 5%
ω_-	ω_0 decreased with 5%
$\Delta\omega$	Difference between successive frequencies
ψ_ζ	Wave phase angle

Acronyms

Symbol	Description
BEM	Blade Element Momentum theory
COB	Centre of buoyancy
COG	Centre of gravity
CS	Coordinate System
CL	Centre Line
CM	Centre of Mass

DLL	Dynamic Link Library
DnV	Det norske Veritas
DOF	Degree of freedom
Eq.	Equation
FEM	Finite element method
FFT	Fast Fourier transform
HF	High frequency
JONSWAP	Joint North sea wave project
L1, L2, L3	Line #1, #2 and #3
LHS	Left hand side
LC	Load case
LF	Low frequency
NREL 5MW	Reference wind turbine model
OC3	Offshore Code Comparison Collaboration, Phase 3
RIFLEX	Flexible Riser Analysis Program
PI	Proportional Integral
PSD	Power spectrum density
RHS	Right hand side
SP	Spar
SIMO	Simulation of marine operations
SS	Semi-Submersible
STD	Standard deviation
SWL	Still water level
TL	Total Lagrangian
TLP	Tension Leg Platform
WF	Wave frequency
2-D	Two dimensional
3-D	Three dimensional

1 Introduction

Wind power is a large natural source for renewable energy. There has been a growing engagement on establishing offshore floating wind farms to capture this valuable resource in many countries the recent years. Countries like USA, China, Scotland and Norway have vast areas suitable for wind farms and are showing their interest in this type of energy. Offshore wind is challenging the standard land based turbines in several ways. Some main advantages are that they can be placed out of sight and do not produce noise for the general public. They do not occupy land space and are suitable for large turbines since they are transported by sea. The wind field offshore is also considered more stable than on land. Downsides are that offshore structures can be exposed to more severe loading than onshore fixed turbines. The sea environment can be rough and the turbines may be difficult to get access to for maintenance and operation.

If we are to overcome the difficulties these types of wind turbines poses, good and efficient tools for analysis are essential. The analysis should include all the important couplings in the dynamics of offshore wind turbines. The importance of such tools is also essential for exploring the different concepts.

There are many offshore floating wind turbine concepts proposed today. One of them is the OC3-Hywind which is based upon the design of spar platforms. Other types are tension legged platforms, semi-submersibles and hybrids of different concepts. In this master thesis an investigation of wave and wind induced loads on the OC3-Hywind will be carried out and a comparison with both a TLP and a semi-submersible will be performed.

2 Reference Model of Spar Type Floating Wind Turbine

The OC3-Hywind (1) is a floating wind turbine concept used in the Offshore Code Comparison Collaboration (OC3) that models offshore floating wind turbines. The concept is based on Statoil's Hywind concept, which is built upon knowledge from the O&G industry and is based on a spar buoy type of platform. In 2009 a test turbine was installed outside Karmøy in Norway. The original Hywind design has been changed, since OC3-Hywind applies the NREL 5 MW turbine that differs from the one Statoil uses. To make the system work in combination with the 5 MW turbine, modifications were made to the turbine support structure.

The total system consists of the floater with a tower and a wind turbine mounted to this substructure. This spar floater is mostly static stable through ballast that moves the COG a large

distance below COB. This leads to a strong restoring moment and a high inertial resistance to pitch and roll. The deep draft of the floater limits its heave motion. The stability triangle in Figure 2 gives an indication of how different floating platforms achieve stability. The three corners symbolize concepts that only rely on ballast, buoyancy, or mooring line stabilization. The OC3-Hywind would be placed in the spot of the tethered spar buoy.

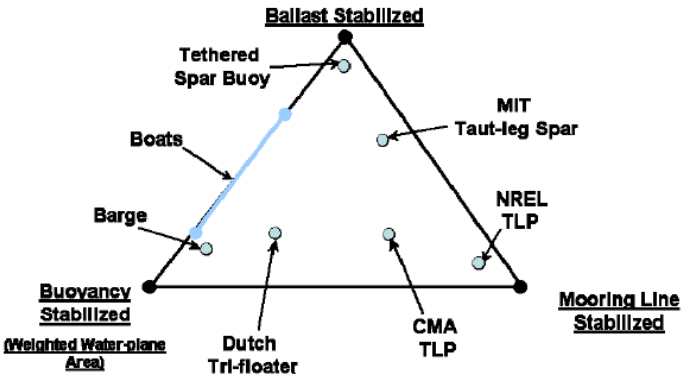

Figure 1 - Floating platform stability triangle (2)

In the end of the thesis, the spar will be compared to two different floaters. One of them is based on the NREL TLP, while the other is a semi-submersible similar to the Dutch Tri-Floater as depicted above. As can be seen in this figure these three concepts are very different in their way of achieving sufficient stability.

The mooring configuration of the OC3-Hywind consists of three catenary mooring lines anchored to the sea bed. They are mainly for station keeping purposes, but will also contribute to the structure's stability with their weight.

2.1 Tower, Nacelle and Hub Structural Properties

The wind turbine used in the modelling of the OC3-Hywind Spar is the NREL 5 MW wind turbine (3). Only the main properties relevant for the mass model will be specified here.

The tower base starts at an elevation of 10 m and extends to 87.6 m. This gives the tower a length of 77.6 m. The base of the tower has a diameter of 6.5 m which is the same diameter as the top part of the floating platform. The tower is tapered changing linearly from 6.5 m to 3.87 m at the top.

The total mass of the tower, nacelle, and hub is 696,900 kg and has its centre of mass (CM) located at $(x, y, z) = (-0.134\ \text{m}, 0\ \text{m},\ 64.210\ \text{m})$. Moments of inertia in roll and pitch around the CM of the

tower are 3,642,052 kgm^2 and for yaw 23,808 kgm^2. The mass and inertias are taken from a note by Zhen Gao (4) , which is based on the tower starting from the still water level (SWL). In the case of the OC3-Hywind the specifications given for the floating structure includes 10 m above SWL. This means that there is some mass that will be included twice when we combine these specifications. The mass model of the tower was hence changed to account for this.

Table 1 - Description of tower, nacelle and hub (1)(5)

Elevation to Tower Base (Platform Top) Above SWL	10 m
Elevation to Tower Top (Yaw Bearing) Above SWL	87.6 m
Overall Tower Mass (Including Turbine etc.)	696,900 kg
Tower Roll Inertia about Tower CM	3,642,052 kgm^2
Tower Pitch Inertia about Tower CM	3,642,052 kgm^2
Tower Yaw Inertia about Tower Centre line(CL)	23,808 kgm^2
Tower Cm	$(x, y, z) = (-0.134 \text{ m}, 0 \text{ m}, 64.210 \text{ m})$
Tower Diameter at Base	6.5 m
Tower Diameter at Top	3.87 m

2.2 Structural properties of the floating platform

The platform has a total length of 130 m and a draft of 120 m. It is symmetric in both the xz -, and the yz -plane. It is convenient to describe the platform by dividing it into an upper part, a tapered part and a lower part. The upper part is cylindrical with a diameter of 6.5 m. This part extends from 10 m above SWL and down to a depth of 4 m. From a depth of 4 m the tapered part extends down to a depth of 12 m, changing its radius linearly from 6.5 m to 9.4 m. At the base of the tapered part, the lower part continues as a cylinder with a diameter of 9.4 m. The reason for including such geometrical changes, are that having a more slender cylinder in the vicinity of the free surface reduces the hydrodynamic loads on the structure.

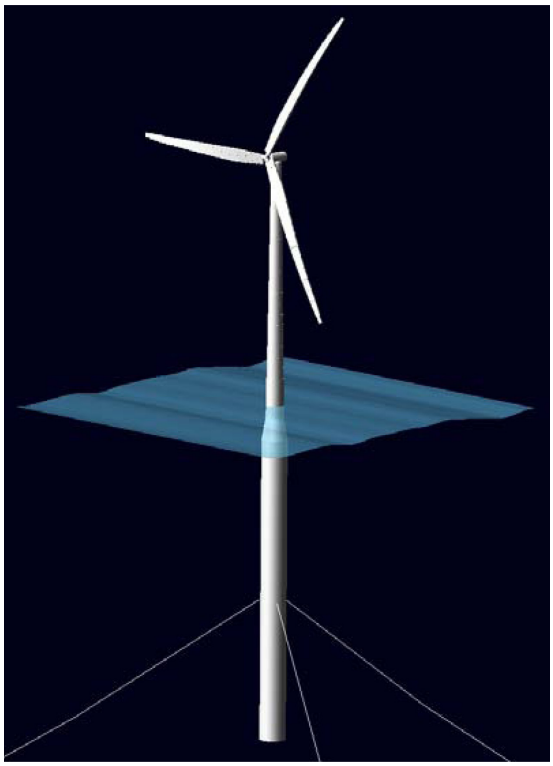

Figure 2: OC3-Hywind model (1)

The total mass of the platform is 7,466,330 kg, centred at a depth of 89.9155 m in the platform CL. This is the combined mass of the steel hull and ballast. The roll and pitch inertias about the CM of the platform are both 4,229,230,000 kgm^2, and the yaw inertia also given around the CM of the platform is 164,230,000 kgm^2.

Table 2 - Description of the floating platform (1)

Depth to Platform Base Below SWL (Total Draft)	120 m
Elevation to Platform Top (Tower Base) Above SWL	10 m
Depth to Top of Taper Below SWL	4 m
Depth to End of Taper Below SWL	12 m
Platform Diameter Above Taper	6.5 m
Platform Diameter Below Taper	9.4 m
Platform Mass, Including Ballast	7, 466,330 kg
Water Displacement	8029.21 m^3
CM Location Below SWL Along Platform CL	89,9155 m
Platform Roll Inertia about CM	4, 229,230,000 kgm^2
Platform Pitch Inertia about CM	4,229,230,000 kgm^2
Platform Yaw Inertia about Platform CL	164,230,000 kgm^2

2.3 Mooring System Properties

The OC3-Hywind is connected to three catenary lines for station keeping purposes. These lines are attached at a depth of 70 m below SWL and with a radius of 5.2 m from the CL. To increase the mooring yaw stiffness, the lines are attached through so called crowfoots (delta connections). The effects of these are modelled as an extra yaw stiffness of 98,340,000 Nm/rad. The connection points are spread equally around a circle with a radius of 5.2 m, with the first point located at the positive x-axis. This leads to an angle of 120 degrees between each connection point. The lines have an unstrecthed length of 902.2 m, a diameter of 0.09 m, a mass per unit length of 77.7066 kg/m, and an extensional stiffness of 384,243,00 N. The anchors are positioned at a radius of 853.87 m from CL , at a depth of 320 m.

Table 3 - Description of the mooring system from (1)

Number of Mooring Lines	3
Angle Between Adjacent Lines	120 deg
Depth to Anchors Below SWL (Water Depth)	320 m
Depth to Fairleads Below SWL	70 m
Radius to Anchors from Platform CL	853.87 m
Radius to Fairleads from Platform CL	5.2 m
Unstrecthed Mooring Line Length	902.2 m
Mooring Line Diameter	0.09 m
Equivalent Mooring Line Mass Density	77.7066 kg/m
Equivalent Mooring Line Weight in Water	698.094 N/m
Equivalent Mooring Line Extensional Stiffness	384,243,000 N
Additional Yaw Spring Stiffness	98,340,000 Nm/rad

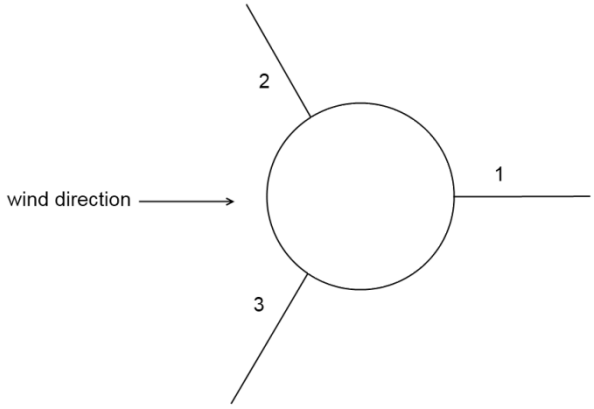

Figure 3 - Sketch of mooring line configuration

3 Theoretical Background on Loads and Analysis of Offshore Wind Turbines

In this chapter, what is considered the governing loads on a typical offshore floating wind turbine will be reviewed. It is important to get an overview of how these loads are described in the applied code, so that important assumptions can be emphasized and a good discussion of the results can be made possible. Detailed theory will not be presented on the different subjects, so the reader is referred to textbooks, manuals and literature for more detailed clarifications (6)(7).

Offshore floating wind turbines are constructed to operate in harsh environments and they are subject to many types of environmental and accidental loads. These loads include waves, wind, current, ice, tides, and marine growth. Not all of these loads have been accounted for in this thesis.

The following sections will describe the different components of the force vector given below.

$$F_i^{Platform} = F_i^{Structural} + F_i^{Hydro} + F_i^{Lines} + F_i^{Wind} \tag{1}$$

The index i reefers to the platform degrees of freedom (DOF),
$i \in (1,2,3,4,5,6) = (Surge, Sway, Heave, Roll, Pitch, Yaw)$ and will be defined in the next section.

In the following sections the Einstein notation will be used, which means that if there is a term with a repeated index, then we are to sum over all possible combinations of 1 to 6 (e.g.
$\mathbf{a} = \mathbf{b} + \mathbf{Mc} \rightarrow a_i = b_i + M_{ij}c_j$ (8))

3.1 Floater Kinematics and Coordinate Systems

To get an overview over the motions and coordinate references used in this rapport, a formal definition is given here. A number of right-handed Cartesian coordinate systems (CS) is used, where all rotations about the axis are defined as positive in the counter-clockwise direction.

- A global earth fixed CS (X, Y, Z), where the XY-plane coincides with the SWL, and positive Z axis is pointing upwards against gravity.
- A body-fixed CS (x, y, z) is placed at the body CL at the undisturbed free-surface with the positive z axis pointing upwards.
- A rotor-fixed CS $(x^{Rot}, y^{Rot}, z^{Rot})$ is placed at the origin of the nacelle, following the body motions. The origin of this rotor fixed CS is located at $(0, 0, 90)$, measured from the origin of the body-fixed CS.

The rigid body motions of the floater consist of 6 DOFs. Three of them are translatory, while the other three are rotational. They are defined relative to the body-fixed CS. The translatory DOFs are; surge (η_1) along the x-axis, sway (η_2) along the y-axis, and heave (η_3) along the z axis. The rotational displacements are; roll (η_4) about the x-axis, pitch (η_5) about the y-axis and yaw (η_6) about the z axis.

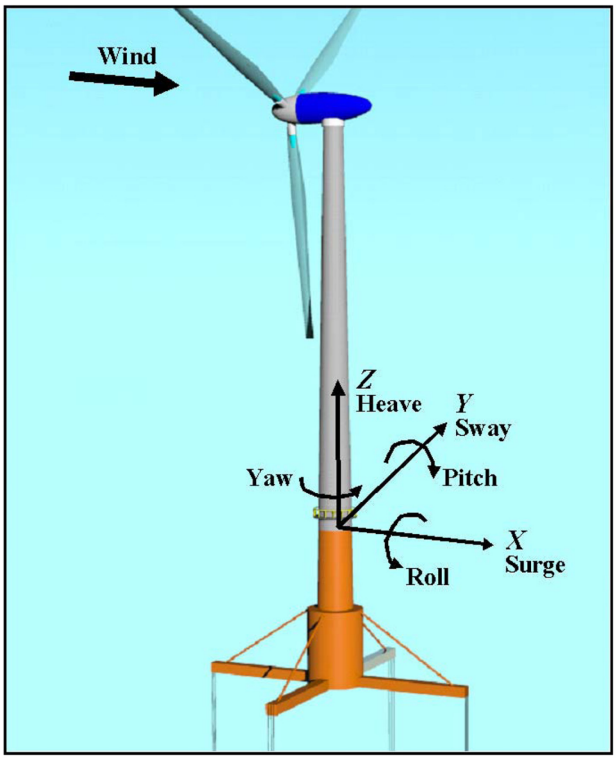

Figure 4 - Rigid body motions (5)

Some loads are applied in different CS's than mentioned here. These will be explained in the subsequent chapters together with the relevant loads.

The equation of motion for the floater rigid body motions are derived through Euler's laws (linear momentum), taken about the origin of the body-fixed CS, which is considered an inertial reference system. The derivations are lengthy and will not be presented here, but can be viewed in the SIMO Theory manual (9).

Since a rigid body is being studied the translations of different points other than the origin have a unique connection to the origin, and can be directly calculated based on the motions of the origin (6):

$$\mathbf{s} = \begin{bmatrix} \eta_1 + z\eta_5 - y\eta_6 & \eta_2 - z\eta_4 + x\eta_6 & \eta_3 + y\eta_4 - x\eta_5 \end{bmatrix} \quad (2)$$

where η_i are the different rigid body modes defined earlier and x, y, z defines the point we want to translate the motions to. This expression can be useful when we look at the motions and accelerations of the nacelle.

3.2 Structural Loads

The components that define the structural load vector, $F_i^{Structural}$ are given in Eq. (3),

$$F_i^{Structural} = F_i^{Inertia} + F_i^{\mathrm{Re}storing} + F_i^{Gyro} \tag{3}$$

The different load components will be defined in the subsequent chapters.

The inertia and restoring load vectors in $F_i^{Structural}$ are normally not presented in this way, but are the terms on the left hand side (LHS) of the equation of motion. The goal here is not to present the fully written equation of motion, but merely to categorize and clarify which loads that are acting on the floater. Therefore this specific way of presentation has been chosen.

3.2.1 Inertia Loads

The tower and platform structure are both assumed to be rigid. The rigid body mass matrix M_{ij} is found from the linear and angular momentum rigid body dynamics: (10).

$$M_{ij} = \begin{bmatrix} m & 0 & 0 & 0 & mz_G & -my_G \\ 0 & m & 0 & -mz_G & 0 & mx_G \\ 0 & 0 & m & my_G & -mx_G & 0 \\ 0 & -mz_G & my_G & I_{11} & I_{12} & I_{13} \\ mz_G & 0 & -mx_G & I_{21} & I_{22} & I_{23} \\ -my_G & mx_G & 0 & I_{31} & I_{32} & I_{33} \end{bmatrix} \tag{4}$$

m is here the total weight of the platform and tower, (x_G, y_G, z_G) are the coordinates of the centre of gravity (COG) for the total system taken from the SWL, and I_{ij} are the moments of inertia ($i, j \in [1,3]$). The inertia load vector can be expressed by,

$$F_i^{Inertia} = -M_{ij}\ddot{\eta}_j \tag{5}$$

Due to the location of the floater COG all terms involving y_G will be zero. The position of COG will have a small non-zero x_G term, since the turbine COG is not precisely located at the CL. This also causes the cross-terms I_{13} and I_{31} to be non-zero.

3.2.2 Restoring Forces

The restoring load vector presented here includes both restoring forces from hydrostatics and gravitational forces. Restoring forces are proportional to the floater displacements:

$$F_i^{\mathrm{Re}storing} = -C_{ij}^{Hydrostatic}\eta_j \tag{6}$$

$C_{ij}^{Hydrostatic}$ is called the hydrostatic restoring coefficient matrix, and η_j represents the DOFs described earlier.

If the platform is perturbed in all its DOFs, dynamic equilibrium considerations will give hydrostatic restoring contributions as shown in Eq. (7) (10). The coefficients have been linearized through the assumption of small angles. Since the platform is symmetric about the xz - and yz -planes in the body fixed CS, the final hydrostatic restoring matrix will take the following form (6):

$$C_{ij}^{Hydrostatic} = \begin{bmatrix} 0 & 0 & 0 & 0 & 0 & 0 \\ 0 & 0 & 0 & 0 & 0 & 0 \\ 0 & 0 & \rho_w g S_0 & 0 & 0 & 0 \\ 0 & 0 & 0 & \rho_w g\left(\iint_{S_0} y^2 dS + V_W z_B\right) - mgz_G & 0 & -mgx_G \\ 0 & 0 & 0 & 0 & \rho_w g\left(\iint_{S_0} x^2 dS + V_W z_B\right) - mgz_G & 0 \\ 0 & 0 & 0 & -mgx_G & 0 & 0 \end{bmatrix} \tag{7}$$

where ρ_w represents the water density, g is the gravitational constant, S_0 is the water plane area at the SWL, V_W is the total displace volume in still water, and z_B is the vertical coordinate to the centre of buoyancy(COB).

The $C_{33}^{Hydrostatic}$ entry states that if the platform is perturbed in the vertical direction, the displaced volume will change. Consequently the vertical buoyancy force will also be changed. Due to the fact

that the platform has a radius that varies with depth, this expression will only be valid for a region of vertical displacements. Using the radius at the SWL to calculate S_0 restricts this region to approximately ± 4 m (neglecting rotations). Due to the long draft of the floater, the vertical excitations are assumed to be small, and $C_{33}^{Hydrostatic}$ is assumed to be valid for all the load case studied. $C_{44}^{Hydrostatic}$ and $C_{55}^{Hydrostatic}$ provide restoring moments when the platform pitches and/or rolls. The integral term captures the effect of stiffness because the different parts of the platform will be submerged or raised from the water when the platform pitches or rolls. The last term in $C_{44}^{Hydrostatic}$ and $C_{55}^{Hydrostatic}$ is due to the change of stiffness when the platform is perturbed in roll or pitch, the vertical position of the COB will change.

The terms associated with gravitation and COG will provide restoring in roll and pitch. Since the COG does not coincide with the CL, there is also two coupling terms with yaw ($C_{46}^{Hydrostatic}$, $C_{64}^{Hydrostatic}$). However, the effect of these terms will be small since $x_G = 0.01$ m for the total system.

3.2.3 Gyro Moments

When the turbine is active, the constant rotor spin at angular speed ω_r will create an angular momentum L_x^{Rot} about the x^{Rot}-axis as given by:

$$\mathbf{L}^{Rot} = \begin{bmatrix} I_{x,r}\omega_r & 0 & 0 \end{bmatrix}^T \tag{8}$$

$I_{x,r}$ is here the rotor moment of inertia about the x axis. Both $I_{x,r}$ and ω_r are assumed to be constant throughout a simulation.

Wind and waves will make the floater rotate with an unsteady angular velocity. In the rotor-fixed CS this angular velocity will be $\boldsymbol{\omega}_B^{Rot}(t)$.Due to this angular velocity, there will be a change of momentum inducing what is called a gyro moment (11):

$$\mathbf{M}_{Gyro}^{Rot} = \frac{d}{dt}(\mathbf{L}^{Rot}) = \boldsymbol{\omega}_B^{Rot} \times \mathbf{L}^{Rot} \tag{9}$$

This means that we can in general have a gyro moment about the y^{Rot}- and z^{Rot}-axis in the rotor-fixed system, when the floater experiences rotational motions about the z^{Rot}- and y^{Rot}-axes, respectively, while the rotor spins around the x^{Rot}-axis. The gyro moment is calculated in the DLL extension TDHMILL3D to SIMO.

3.3 Hydrodynamic Loads

The total force vector from hydrodynamic loads and moments on the 6 DOFs of the floater can be expressed by,

$$F_i^{Hydro} = F_i^{Waves,(1)} + F_i^{Waves,(2)} + F_i^{Viscous} \tag{10}$$

where $F_i^{Waves,(1)}$ and $F_i^{Waves,(2)}$ are the 1st order and 2nd order wave forces, respectively, and $F_i^{Viscous}$ constitute the contribution from viscous effects on the hull.

3.3.1 Regular Wave Theory

The waves are described using Airy wave theory. This theory describes the waves as linear long-crested sinusoidal components, and it is based upon potential theory. When applying potential flow theory, there are some basic assumptions about the fluid that need to be satisfied. The fluid needs to be inviscid, irrational, and incompressible. According to the Airy wave theory, we can express the velocity potential ϕ_0 for these regular waves as:

$$\phi_0 = \frac{\zeta_a g \cosh k\left(z+h\right)}{\omega \cosh kh} \cos\left(-\omega t + kx + \psi_\zeta\right) \tag{11}$$

where ζ_a, k, ω and ψ_ζ are the incident wave amplitude, wave number, wave frequency and wave phase angel, respectively. Further, g is the gravitational constant, z and x are the vertical and horizontal coordinates, respectively, h is the water depth taken from the SWL, and t is the time.

ϕ_0 satisfies the linearized boundary value problem explained in Faltinsen (6). The boundary conditions (BC) include: fluid particles on the free-surface must remain there (Kinematic BC), and that the pressure should be equal to the ambient pressure p_a at the free-surface (Dynamic free-surface BC).

From the free-surface dynamic condition an expression for the free surface elevation can be found(6):

$$\zeta = -\frac{1}{g}\left(\frac{\partial \phi_0}{\partial t}\right)_{z=0} = \zeta_a \sin\left(\omega t - kx + \varphi\right) \tag{12}$$

$\varphi = -\psi_\zeta$ is now what we will call the phase angel.

Linear theory also leads to a dispersion relationship that describes the relation between the wave frequency and the wave number. The dispersion relationship for finite water depths is given by,

$$\omega^2 = kg\tanh(kh) \tag{13}$$

Relations for the parcel velocities can be found directly from the definitions of the velocity potential:

$$\frac{\partial \phi_0}{\partial x} = u,\ \frac{\partial \phi_0}{\partial z} = w \tag{14}$$

All conditions for applying Bernoulli's equation are satisfied in potential theory. The Bernoulli's can thus be used to find the pressure:

$$p - p_a = \underbrace{-\rho_w g Z}_{\text{static}} \underbrace{-\rho_w \frac{\partial \phi}{\partial t} - \frac{1}{2}\rho_w (\nabla \phi)^2}_{\text{dynamic linear and quadratic}} \tag{15}$$

3.3.2 Irregular Wave Theory

To more correctly describe a physical sea state a random irregular sea is needed. Such a sea can be described by superimposing many linear regular waves with different heights, frequencies, directions, and phase angles. The direction parameter is not accounted for in this thesis, so all wave components are assumed to travel along the same horizontal path.

The expression for the surface elevation ζ can then be expressed by the sum of N numbers of different regular waves, ζ_k.

$$\zeta(t,x) = \sum_{k}^{N} \zeta_k = \sum_{k=1}^{N} A_k \sin(\omega_k t - k_k x + \varphi_k) \tag{16}$$

A_k is here the incident wave amplitude of wave component k, and the phase angle φ_k is sampled from a uniform distribution over $[-\pi, \pi]$. It can be shown that the wave amplitude A_k can be expressed by a wave spectrum as (6):

$$\frac{1}{2}A_k^2 = S(\omega_k)\Delta\omega \tag{17}$$

where $S(\omega_k)$ is the wave spectrum and $\Delta\omega$ is the constant difference between successive frequencies. The harmonic wave component A_k is generated through Fast Fourier Transform (FFT), and the total wave elevation is calculated before the analysis starts.

$S(\omega_k)$ is described in this rapport using a three parameter Joint North sea wave project (JONSWAP) specter shown in Eq. (18). A sea state can then be uniquely described in terms of the significant wave height H_s, the peak period T_p ,and a peakedness parameter γ:

$$S_\zeta(\omega_k) = \frac{5.061 H_s^2 (1 - 0.287 \ln \gamma) g^2}{T_p^4 \omega_k^{\,5}} \exp\left[-1.25 \left(\frac{2\pi}{T_p \omega_k} \right)^4 \right] \gamma^{\exp\left(-\frac{\left(\frac{T_p \omega_k}{2\pi} - 1 \right)^2}{2\sigma(\omega)^2} \right)} \tag{18}$$

The scaling factor σ varies with incident wave frequency:

$$\sigma(\omega) = \begin{cases} 0.07 \text{ for } T > T_p \\ 0.09 \text{ for } T < T_p \end{cases} \tag{19}$$

The peakedness parameter γ is set to 3.3 for all cases considered in this report.

3.3.3 1st Order Wave Forces

The contribution to the 1st order wave forces acting on the body is split into two terms:

$$F_i^{Waves,(1)} = \underbrace{F_i^R}_{Radiation} + \underbrace{F_i^D}_{Diffraction} \tag{20}$$

These two terms constitute the solution of the hydrodynamic linear potential flow problems of diffraction and radiation. How the solution to the potential flow problem is found can be seen in section 6.1. An important factor regarding the solution is that it consists of transfer functions that are frequency dependent. Due to the frequency dependence, these functions cannot be used directly in the time domain analysis performed. The two subsequent sections will explain how these forces are implemented in the time domain analysis.

3.3.3.1 Radiation Forces and Moments

The radiation problem is related to hydrodynamic loads on the body due to forced oscillations of the body in all its DOFs radiates outgoing waves which results in hydrodynamic forces acting on the body, including added mass- and damping forces. The solution of the radiation problem is the frequency dependent added-mass $A_{ij}(\omega)$ and potential damping $B_{ij}(\omega)$ coefficients. As the names indicate, the added mass force is proportional to the floater accelerations, while the potential damping force is proportional to the velocity.

$A_{ij}(\omega)$ and $B_{ij}(\omega)$ can be split into the summation of their asymptotic values at infinite frequency ($A_{\infty,ij}$ and $B_{\infty,ij}$) and their frequency dependent parts ($a_{ij}(\omega)$ and $b_{ij}(\omega)$):

$$A_{ij}(\omega) = A_{\infty,ij} + a_{ij}(\omega), \quad B_{ij}(\omega) = B_{\infty,ij} + b_{ij}(\omega) \tag{21}$$

The asymptotic value $B_{\infty,ij}$ of the potential damping can be shown to be zero (9). By taking the inverse Fourier transform of the radiation forces in the frequency domain, the total force can be described in time domain by:

$$F_i^R(t) = -A_{\infty,ij}\ddot{\eta}_j - \int_0^t h_{ij}(t-\tau)\dot{\eta}_j(\tau)\,d\tau \tag{22}$$

where $h_{ij}(\tau)$ is the retardation function found from a transform of the frequency-dependent added-mass and damping as shown below:

$$\begin{aligned} h_{ij}(\tau) &= \frac{1}{\pi}\int_0^\infty \left[b_{ij}(\omega)\cos\omega\tau - \omega a_{ij}(\omega)\sin\omega\tau \right] d\omega \\ &\underset{\substack{\text{Causality} \\ h_{ij}(\tau)\equiv 0,\tau<0}}{=} \frac{2}{\pi}\int_0^\infty b_{ij}(\omega)\cos\omega\tau\, d\omega = -\frac{2}{\pi}\int_0^\infty \omega a_{ij}(\omega)\sin\omega\tau\, d\omega \end{aligned} \tag{23}$$

The term involving potential damping is used in SIMO to calculate the retardation functions.

If we study the retardation force term $-\int_0^t h_{ij}(t-\tau)\dot{\eta}_j(\tau)\,d\tau$ of Eq. (22) we can see that the history of the motion in all the previous time steps needs to be accounted for. The total retardation force F_i^R at time t can be seen as the summation of the part force impulse responses, from all the previous steps value at time t (e.g. for a 1-dof system in surge: $F_{Total}^R \approx \sum_{k=0}^{N-1} F_k^R = \sum_{k=0}^{N-1} h(t-t_k)\dot{\eta}_1(t_k)\Delta t$). This introduces what is a called a memory effect.

3.3.3.2 Diffraction, Wave Excitation Forces and Moments

The 1st order wave excitation forces and moments are related to what we call the diffraction problem. In the diffraction problem we assume that the body is fixed and interacting with incident waves. This interaction leads to a varying fluid pressure on the mean body wetted surface, which cause hydrodynamic loads, called wave excitation loads.

The solution to the diffraction problem is, as for the radiation problem, solved in the frequency domain by the use of HydroD. The wave excitation loads are given in terms of force and moment transfer functions:

$$F_i^D(\omega_k, \beta) = H_i^D(\omega_k)\tilde{\zeta}(\omega_k) \tag{24}$$

where $H_i^D(\omega_k)$ is the complex 1st order wave force transfer function and $\tilde{\zeta}(\omega_k)$ the complex harmonic wave component. With complex it means that e.g. for the harmonic wave component:

$$\tilde{\zeta}(\omega_k) = A_k e^{j(\omega_k t - k_k x + \varphi_k)} \tag{25}$$

and the surface elevation, ζ can be found from taking the real part of $\tilde{\zeta}$.

To represent these forces for an irregular wave field and in time domain simulations, a similar transformation as for the retardation force is done. First the inverse Fourier transform is taken of the transfer function in Eq.(24):

$$h_i^D(\tau) = \frac{1}{2\pi}\int_{-\infty}^{\infty} H_i^D(\omega) e^{i\omega\tau} d\omega \tag{26}$$

Then the excitation load is expressed as the convolution between h_i^D and ζ.

$$F_i^D(t) = \frac{1}{2\pi}\int_{-\infty}^{\infty} h_i^D(\tau)\zeta(t-\tau) d\tau \tag{27}$$

As can be seen from Eq. (27), the wave excitation forces do not depend on the motion of the floater. The wave excitation forces can then be pre-calculated before time simulation for different headings (β) so that yaw motion can be accounted for. In the simulations the excitation forces are applied at the calculated static position of the floater.(9)

3.3.4 2nd Order Wave Forces

As mentioned earlier, the 1st order wave forces only consider terms which are proportional to the wave-amplitude. When incident waves become steeper ($k\zeta_a$) the higher order terms become more important for good estimates of loads and motions. Including terms up to second order will better enforce the impermeability of the body at its instantaneous configuration, and the pressure will be made atmospheric at the instantaneous free surface. In addition, the normal fluid velocity at the free surface will be closer to the free-surface normal velocity. The 2nd order forces are generally much smaller than the 1st order forces. Still, they may be very important for some structures, since they may cause resonance excitations due to difference and sum frequency effects. Not all of the 2nd order forces have been included here, but a simplified model has provided the slowly varying drift

forces. The main reason to include the slowly varying wave forces is that for moored platforms they will induce resonant motion in surge, sway and yaw. 2nd order sum frequency effects are not considered relevant for the floater, since there are no natural periods in the frequency range above the wave frequencies.

3.3. 3.1 Mean and Slowly Varying Drift Forces

The mean drift forces are the time independent portions of the 2nd order forces. In general, there will be 6 mean drift forces/moments, one for each different DOF. The mean loads are due to the body capability of generating waves (6).

As will be discussed in section 6.1, the mean drift forces were obtained through conservation of momentum calculated in HydroD. This provides the mean wave drift coefficients $\bar{H}_i^{(2)}(\omega_k)$ in surge, sway and yaw in terms of incident wave frequency ω_k. $\bar{H}_i^{(2)}(\omega_k)$ is proportional to the wave amplitude squared and for an irregular sea state, we can then find the total mean drift force $\bar{F}_i^{(2)}$ as:(6)

$$\bar{F}_i^{(2)} = \sum_k^N \bar{H}_i^{(2)}(\omega_k) A_k^2, \text{ where i = 1, 2, 6} \tag{28}$$

A general formula for the slowly varying drift forces in an irregular sea state can, according to Faltinsen (6), be written as:

$$F_i^{SV} = \sum_{l=1}^N \sum_{k=1}^N A_l A_k \left\{ T_{lk}^{ic} \cos\left[(\omega_l - \omega_k)t + (\varepsilon_l - \varepsilon_k)\right] + T_{lk}^{is} \sin\left[(\omega_l - \omega_k)t + (\varepsilon_l - \varepsilon_k)\right] \right\} \tag{29}$$

where A_l, A_k, ω_l, ω_k, ε_l, ε_k, are the amplitude, frequency and phase angle of regular wave component l and k, respectively. N is the total number of wave components, and T_{lk}^{ic}, T_{lk}^{is} are the 2nd order transfer functions for the difference frequency loads. The i in the superscript ic and is represents loading in direction i, while c and s refer to the coefficients of the cosine and sine terms, respectively.

It can be shown that the mean value of Eq. (29)is given by:

$$\bar{F}_i^{SV} = \sum_{k=1}^N A_k^2 T_{kk}^{ic} \tag{30}$$

Both Eq.(28) and Eq.(30) describe the same mean value so T_{kk}^{ic} is equal to the $\bar{H}_i^{(2)}(\omega_k)$ of Eq. (28).

By taking advantage of the Newman's approximation (6), the 2nd order wave force transfer function can be approximated by only using values along the line $\omega_k = \omega_l$. The consequence of this approximation is that the slowly varying drift forces can be calculated based on the mean drift force coefficients provided from HydroD and there is no need to find the full 2nd order transfer functions.

The method depicted above has been applied to generate time series of the slowly varying forces. How the implementation is done in time-domain will not be discussed here. The important part was to show that the slowly varying drift forces can be calculated only based on $\bar{H}_i^{(2)}(\omega_k)$, which is the input to SIMO. The forces are, as for the 1st order wave excitation forces, pre-generated with FFT for different headings at the static position of the floater.

3.3.5 Viscous Drag

Potential theory is based on the assumption of inviscid fluid. This assumption does not always hold in the true sea environment. Viscous effects can for many cases contribute to large loads, and they induce damping to the platform motions.

An important viscous load for the floater is the drag force. The drag force works in-line with the incident wave and current direction in the cross-sectional plane. The force is cause by flow separation and shear stress along the body surface. This force will be included by using the quadratic drag term in the relative Morrison's equation. Eq. (31) gives the drag force in a local strip CS. The total drag forces and moments are then found by integration over the wetted body to the mean surface or the free surface.

$$\mathbf{dF}_s^{Viscous} = \frac{1}{2}\rho_w C_D D_s dz \left(\mathbf{v_s} - \dot{\mathbf{X}}_\mathbf{s}\right)\left|\mathbf{v_s} - \dot{\mathbf{X}}_\mathbf{s}\right| \tag{31}$$

where ρ_w is the water density, C_D is a non-dimensional drag coefficient, D_s is the strip diameter, dz is the length of the differential strip, $\dot{\mathbf{X}}_\mathbf{s}$ is the strip velocity, and $\mathbf{v_s}$ is the water particle velocity in the local strip CS.

In general, the drag on the strips may cause viscous damping forces and moments on the floater ($F_i^{Viscous}$) in surge, sway, pitch and roll. There is no yaw moment, because of the floater symmetry, and no vertical force from the Morrison equation, since it is not valid in that direction (5). The particle velocities are calculated before simulation. This causes this formulation to be strictly valid for small displacements only.

It can be shown that, with an assumption of deep water linear incident waves, the drag force will be largest near the free surface, and it will decrease with depth. This gives the resultant an attack point close to the free surface. The application of linear wave theory gives us an error of the undisturbed velocity distribution under a wave crest, since nonlinear effects are important there. In reality the drag force should actually go to zero, since we need to recover the atmospheric pressure at the wave crest (6). Based on this, the drag force will only be integrated to the mean surface, so that we are in validation with linear theory.

The reference model (1) uses a drag coefficient of 0.6 and base this choice on Reynolds Number exceeding 10^5 in the moderate and severe sea conditions. Calculations of Reynolds Number have also been done here for our defined sea states (Table 9) to check if we are in the same region.

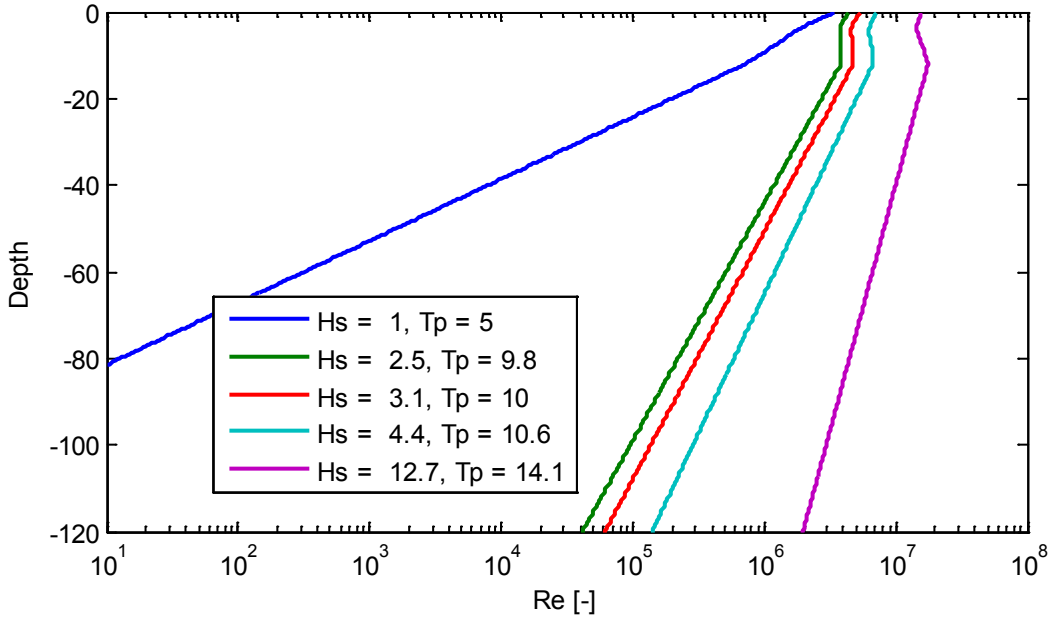

Figure 5- Reynolds number for the different load cases (1)

As can be seen from the figure above Re only exceeds 10^5 for the two most severe load cases. These two cases are also the basis for our moderate and severe sea states and $C_D = 0.6$ will be used.

3.4 Mooring and Mooring Line Loads

Mooring systems are applied for station keeping purposes. When the floating platform is displaced from its equilibrium position, due to external forces as wind and waves, the mooring lines will provide restoring forces and moments, as well as inertia and damping effects. The reference model utilizes a catenary mooring system, which contributes with stiffness through two different types of effects. The first contribution is stiffness due to the catenary shape of the mooring line itself. When the floater is displaced, the tension at the fairlead will change due to the change of catenary shape

leading to a restoring force. The second contribution is from elastic deformation of the mooring line. This depends highly on the material of the mooring line, and it is in most cases small compared to the catenary effect. Restoring through elastic deformations is more important for taut mooring systems. Besides stiffness, mooring lines also contributes to inertia and damping forces on the floating platform. The catenary equations can be viewed in Faltinsen (6).

To understand the basic assumptions and loads that apply to the mooring lines, an introduction to the theory behind the modelling is needed. For detailed derivations of relations and expressions, the reader is referred to RIFLEX manual (12).

In the numerical code applied a finite element method (FEM) approach is used. The lines are modelled with 3-D bar elements. Such bar elements consist of a node with 3 spatial DOFs at each element end (Figure 6). Using bar elements and not beam elements, which has 3 additional rotational DOFs, involves neglecting the bending stiffness of the lines. This is often considered a valid assumption for most catenary lines. The motion of the nodes is described by a total Lagrangian formulation, which involves referring the displacements in configuration C_n back to the initial undeformed configuration C_0.

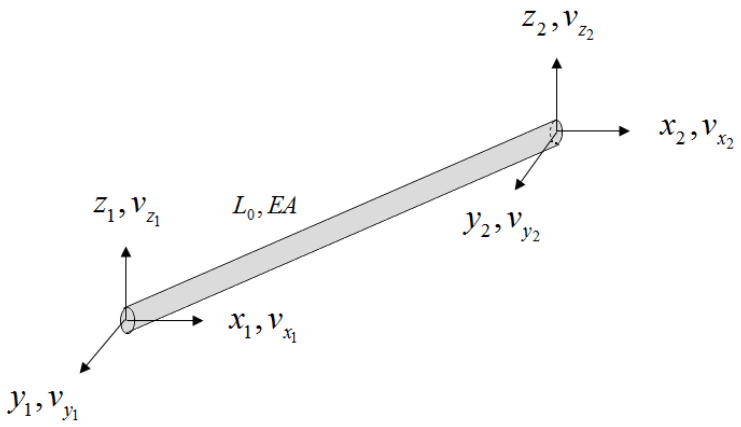

Figure 6 - Bar element

In the formulations of strains the assumption of small strains are applied. The cross terms in the Lagrangian (Green) strain tensor can therefor be neglecting. This gives us the following expressions for strain ε and stress σ:

$$\varepsilon = \frac{L - L_0}{L_0}, \ \sigma = \frac{N}{A_0} \tag{32}$$

L_0 is here the initial stress free length, and L is the length after deformation. N is the normal force in the element, and A_0 is the initial cross-sectional area.

The constitutive law applied is Hook's law for linear elastic materials:

$$\sigma = \varepsilon E \tag{33}$$

where E is the elastic modulus of the material applied.

In the finite element formulation, linear displacement functions are used and the equation of motion is found using an incremental form of virtual work.

The mooring lines are subject to loads due to weight, buoyancy, sea bed contact, and structural damping. They are also subject to hydrodynamic loads and forced displacements due to vessel motions.

The seabed tangent is modelled as a linear vertical stiffness at the seafloor.

Structural damping is included by the use of Rayleigh mass and stiffness proportional damping:

$$\mathbf{C} = \alpha_1 \mathbf{M} + \alpha_2 \mathbf{K} \tag{34}$$

$\mathbf{M}$, $\mathbf{K}$ and $\mathbf{C}$ are the mass, stiffness and damping matrices, respectively, of the total mooring line system. α_1 and α_2 are the inertia and stiffness proportional damping coefficients, respectively, that can be chosen to approximate the structural damping of the mooring lines.

Only the stiffness proportional α_2 term is applied, and this factor will affect all DOFs of the mooring system. A standard value in RIFLEX of $\alpha_2 = 0.001$ was chosen. Due to both α_2 and the mooring line stiffness being small, the Rayleigh damping is assumed to have small impact on the global motions.

The mooring lines will also be subject to viscous effects. These effects include a tangential friction force (F_t) and a drag force (F_n) normal to the line element. When defining the drag force, it is assumed that the instantaneous drag force direction is always parallel to the instantaneous transverse relative velocity component. The viscous forces acting on the elements can then be expressed as:

$$F_t = \frac{1}{2}\rho_w S_w C_{dt} V_{rel_x} \left| V_{rel_x} \right|, \qquad F_n = \frac{1}{2}\rho_w d C_{dn} \left(V_{rel_y}^2 + V_{rel_z}^2 \right) \tag{35}$$

where ρ_w is the water density, S_w is the cross-sectional wetted surface, d is the element diameter, C_{dt} and C_{dn} are drag coefficients in tangential and normal direction, respectively, and V_{rel_x}, V_{rel_y} and V_{rel_z} are the relative water velocity in local element x-, y- and z-directions.

The reference model does not specify detailed mooring line information. Based on the recommended practices of position mooring from DnV (13)drag coefficient in the normal direction was chosen as 1.2 and the tangential coefficient as zero.

In addition to these mentioned loads, the mooring lines will also feel the effect of added mass. This contribution is added to the elements of the mass matrix. The value is assumed to be $0.25\pi\rho_w d^2$, which is the weight of the displaced fluid of a cylindrical cross-section. This is a typical value found in the literature (14).

The connection between mooring lines and the rigid floater is described with constraints (master-slave technique).

3.4 Aerodynamic Loads

3.4.1 Thrust

If we simplify a rotor into an ideal permeable disc, as depicted in Figure 7, a simple expression for the thrust force can be derived. The assumptions behind an ideal disc include frictionless flow over the disc and that there will be no rotational velocity component in the wake. The application of Bernoulli's equation from far downstream to the rotor, and from just behind the rotor to far downstream in the wake, shows that the wind flow over the rotor causes a discontinuous pressure drop at the rotor plane. This pressure drop results in a thrust force T acting against the flow, reducing the wind speed from V_0 upstream to u_1 downstream. The rotor will hence feel the thrust force pushing it downstream. The resulting expression for the thrust force is given by: (7)

$$T = \Delta pA = \frac{1}{2}\rho_a A\left(V_o^2 - u_1^2\right) \tag{36}$$

where A represents the disc area, ρ_a is the air density, and the velocities are similar as described above.

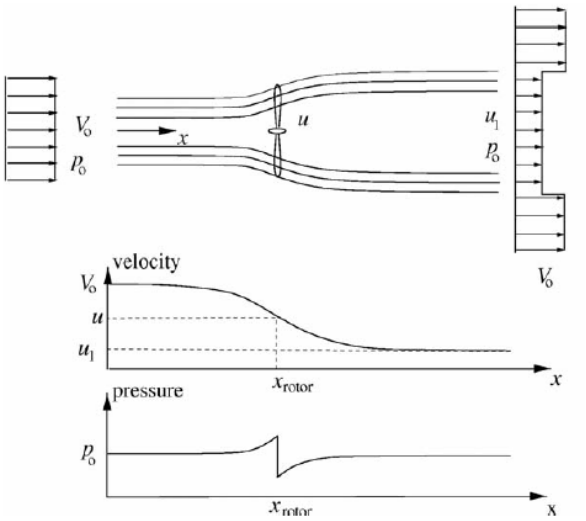

Figure 7 – Simplified wind rotor model (7)

Typically we define the thrust coefficient C_T when expressing the thrust force T.

$$T = \frac{1}{2}\rho_a A C_T V_0^2 \tag{37}$$

The thrust coefficient is found through calculations and/or experiments. In this study the thrust coefficients are obtained by steady state blade element momentum (BEM) theory.

BEM theory is basically an extension of the momentum theory explained above to 2-D, taking into account local events at the actual blades. There are also many extensions to this theory that corrects assumptions applied in the BEM theory (15). When using this procedure, C_T can be calculated based on the shapes of specific airfoils and on how it will vary with different angles of attack.

The values of C_T used here are based on the reference wind turbine (3). The resulting thrust curve applied can be seen in Figure 11.

3.4.2 Wind field

The loads on a wind turbine are highly dependent on a realistic description of the wind flow. Wind has both spatial and temporal variations, and these variations should be described correctly. The variations can be due to factors like wind shear, turbulence, obstacles, and wind/tower interactions.

Wind shear is related to how the mean wind speed increases with the height above the sea surface. This increase is related to surface roughness and atmospheric stability. A typical description of the variation due to surface roughness is made through a power law profile.

$$V_0(z) = V_0(z_0)\left(\frac{z}{z_0}\right)^{\alpha} \tag{38}$$

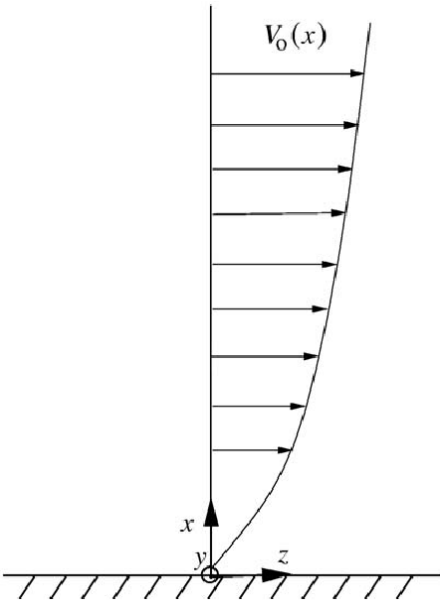

Figure 8 – Wind shear (7)

For standard wind turbine classes, according to IEC61400-1, an exponent of $\alpha = 0.2$ should be used for onshore locations and an exponent of $\alpha = 0.14$ for offshore locations. Corrections in order to include atmospheric stability variability as well can be done.(16)

Atmospheric turbulence will cause time dependent variations in the wind speed. A turbulent wind speed can be seen as a speed that fluctuates around a mean value. The intensity of the turbulence is measured as the ratio between the standard deviation and the mean of the wind speed during a measuring ($I = \sigma_W / V$). Another type of fluctuating phenomena is gusts causing large loads for a short period of time, due to sudden increase in wind speed over a short time period.(16)

The time series of the wind field are generated by the use of a Kaimal wind spectrum:

$$S_W(f) = 4{\sigma_W}^2 \frac{L_k / V_{Hub}}{\left(1 + 6f\frac{L_k}{V_{Hub}}\right)^{\frac{5}{3}}} \tag{39}$$

where V_{Hub} is the mean wind speed at the hub, f is the frequency, σ_W is the wind speed standard deviation, and L_k is a length scale parameter that depends on the height of the hub. The scale parameter and standard deviation are typically defined as below:

$$\sigma_W = I\left(0.75V_{Hub} + 5.6\right), \quad L_k = 8.1\lambda \tag{40}$$

For hub elevations above 60m, λ is usually set to 42 m, which is the value used here (10). Wind time series are generated before time domain simulations starts.

3.4.3 Thrust Implementation

First we define the total load vector caused by the wind F_W^{Rot} in the local rotor CS.

$$F_W^{Rot} = \begin{bmatrix} T & 0 & 0 \end{bmatrix}^T \tag{41}$$

This defines the thrust force as a force that attacks the origin of the local rotor CS with direction always normal to this moving CS.

The magnitude of the thrust force is found by replacing V_0 in Eq. (37) with the x component of the relative velocity V_{rel}^{Rot} between wind and hub. The thrust coefficient C_T will also be calculated based on this velocity from the input values shown in Figure 11. The relative velocity is defined as the difference between the wind velocity V_w^{Rot} and the hub velocity V_r^{Rot} in the local rotor CS.

$$V_{rel}^{Rot} = V_w^{Rot} - V_r^{Rot} \tag{42}$$

In general V_{rel}^{Rot} may have three nonzero components. The loads that may occur due to wind flow over the rotor in the y - and z -directions are not considered.

Regarding the discussion of the results in the later sections it is important to emphasize that the thrust force will lead to moments around the origin of the local body CS. If we define a vector x_r^L going from the origin of the local body CS to the local rotor CS, these moments can be expressed as:

$$M_W^L = x_r^L \times F_W^L \tag{43}$$

where M_W^L is the moments around the origin of the local body CS, due to the forces F_W^L at the hub.

In the load case analysis in section 7.4, M_W^L will contribute to large motions in both roll and yaw when we have a skew of wind and wave directions.

The implementation of the thrust forces and thrust induced moments is done through the DLL extension TDHMILL3D to SIMO.

3.5 Control Systems

The reference wind turbine model used is the NREL 5MW wind turbine (3). This section will present a summary of the reference model control system and an extension of this system applied in this thesis.

The NREL 5MW baseline control system utilizes an independently working generator torque and blade pitch controller. Both control systems take only the generator speed measurements as feedback inputs. To suppress high-frequency oscillations, this measured speed goes through a low-pass filter.

There are a total of 5 different control regions (1, 1 ½, 2, 2 ½ 3) applied in the control scheme. Region 1 is below cut-in speed, where the torque is zero. This is a start-up region, and the wind is accelerating the rotor. Region 1 ½ is a transition between 1 and 2. In region 2 an optimized power capture scheme based on the generator torque is applied. This involves varying the generator torque, so that a constant tip speed ratio is maintained. This tip speed ratio will lead to a peak power coefficient. The blade pitch angle is zero throughout this region. Region 2 ½ is a transition region between 2 and 3 that limits tip speed and noise emissions at rated power. The blade pitch controller is active in region 3. The computations of suitable blade pitch angles are based on a proportional-integral (PI) control on the speed error between the filtered and the rated generator speed. This region utilizes the blade pitch controller to achieve constant generator speed, which leads to constant power.

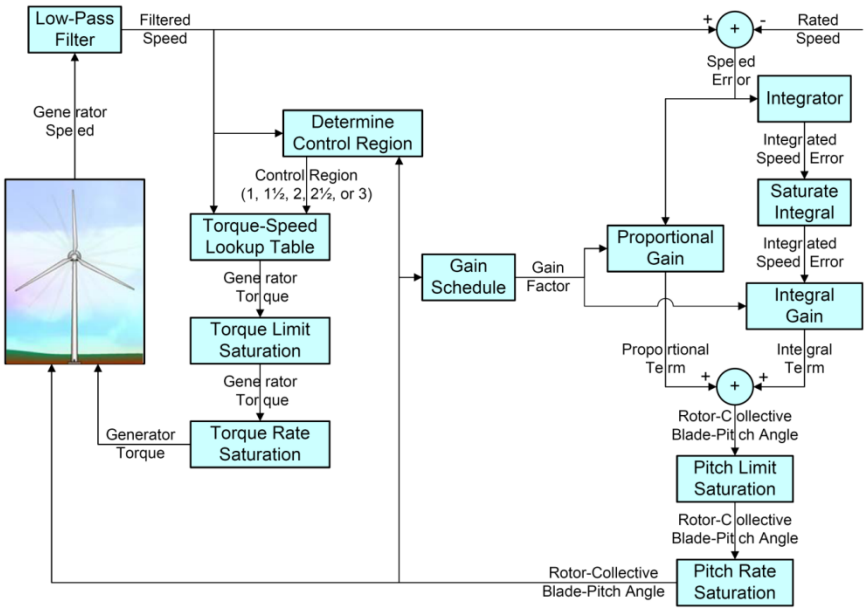

Figure 9 – Wind turbine control system (3)

The resulting steady state output from the NREL 5MW turbine was found in (3) by running a series of simulations with steady uniform wind speeds.

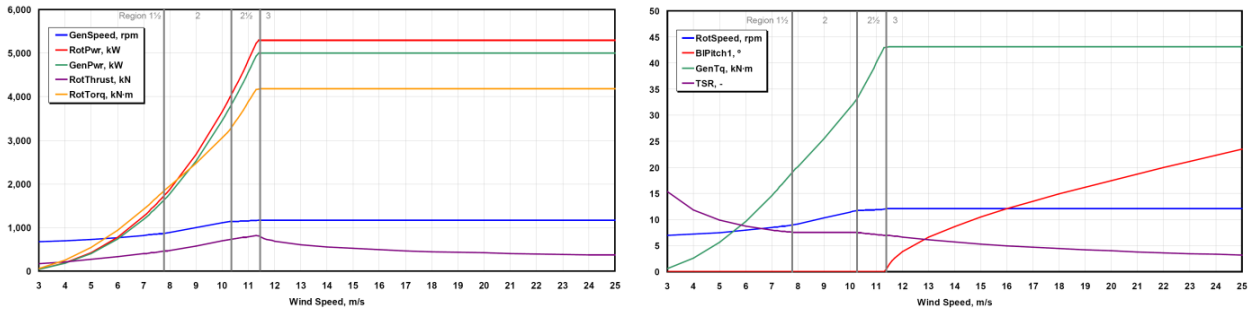

Figure 10 – Steady state results from the NREL 5MW wind turbine(3)

The simplified wind turbine model in TDHMILL3D takes the thrust and power curve presented above as input. The curves are both related to relative wind speed. The thrust curve is modified to also include the effects of wind speeds above cut-off at 25 m/s. At those high wind speeds the turbine is shut off with the blade chord direction parallel to the wind.

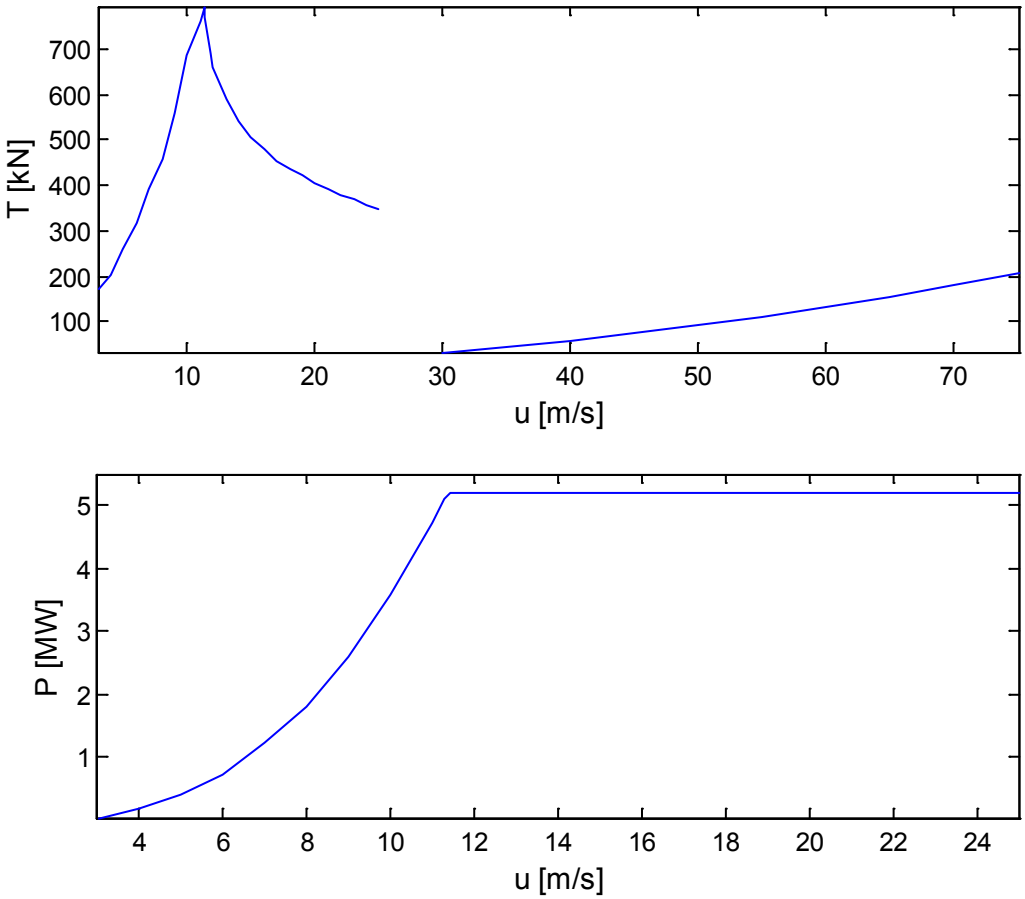

Figure 11 – Thrust and power curve

The effect of only having the thrust curve from the steady state simulations as input and not taking into account the whole wind turbine dynamics with controller is that we assume quasistatic conditions. Obviously, when we are simulating with turbulent wind, this assumption may not hold completely. However, the simplified model is considered adequate for this comparison study.

An extension to the baseline control system described has also been applied by the use of a notch filter that works on the translational velocity of the hub, $V_{r_x}^{Rot}$.

Filters are generally applied to remove or attenuate certain frequencies or band of frequencies from a signal. The notch filter or band reject filter that is used here can be described with the transfer function (17):

$$H(s) = \frac{s^2 + 2\zeta_N \omega_0 + \omega_0}{s^2 + 2\zeta_D \omega_0 + \omega_0} \tag{44}$$

This transfer function describes a system with two poles and two zeros (the roots of the numerator are the zeros and the roots of the denominator are the poles). The location of the poles and zeros in

the complex plane can be found by solving for the roots in Eq.(44), or directly in the terms of the parameters defined in Figure 12 (18) .

$$\theta = \sin^{-1}\zeta, \quad \sigma = \zeta\omega_0, \quad \omega_d = \omega_0\sqrt{1-\zeta^2} \tag{45}$$

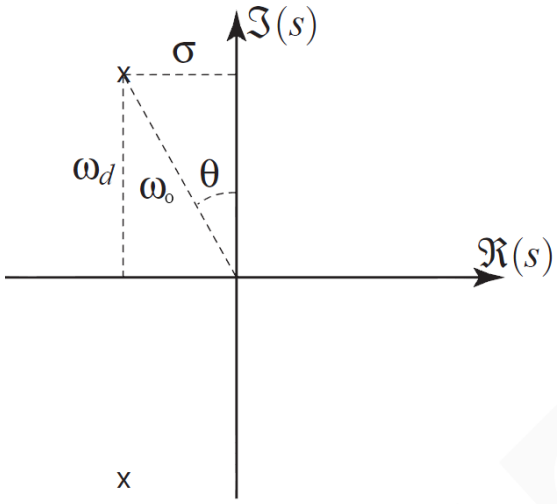

Figure 12 – The locations of the roots of $H(s)$ in the s-plane.

The parameters of Eq. (45) are only valid for $\zeta \leq 1$, when the solution to the roots of $H(s)$ are complex conjugates (19).

It is the location of the poles and zeros and how these are located compared to each other that determines the 'shape' of the notch (See Figure 17). The filter will be cornered around the platform pitch natural frequency.

The effect of the notch filter is that the relative velocity contribution from the translation motion of the hub will be reduced both at and around the cornered frequency. The blade pitch control will react differently. There can still be frequencies in the wind velocity around the pitch natural frequency. The effects of the notch filter can be viewed in section 7.5. The filter is implemented in the time domain, but the details around how this is done will not be discussed here.

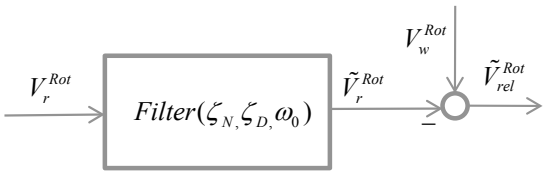

Figure 13 - Block diagram of filter

The reason for introducing this filter is due to the negative slope of the thrust curve above rated speed. This negative slope may contribute to negative damping of the platform pitch motion. Jonkman (5) gives a good explanation of this effect, presenting the problem by simplifying the equation of motion to only a 1-DOF system for the rigid pitch motion. By transforming the pitch motion at the SWL to translation motion at the hub ($x = L_{HH}\eta_5$, Eq.(2)), and by applying a Taylor series expansion, he shows that the thrust force can be written as:

$$T(t) = T_0 - \frac{\partial T}{\partial V}\dot{x} \tag{46}$$

where T_0 is the thrust at a linearized point, and V is the wind speed. We are here only considering variations in thrust due to hub speed. The total damping contribution looking at the translation motion of hub will then be:

$$B_x = \frac{B_{Radiation} + B_{Viscous}}{L_{HH}^2} + \frac{\partial T}{\partial V} \tag{47}$$

Since the term $\frac{\partial T}{\partial V}$ being negative in the region above rated, motion amplifications occur if the term is large. The notch filter is therefore tuned on the pitch natural frequency.

If we were to augment this 1-DOF system with yaw and roll, the yaw DOF would also be affected by $\frac{\partial T}{\partial V}$, since the thrust force T gives a moment about the z axis if the platform rolls (Eq. (43)). Due to limited time left when this was discovered, this influence on yaw has not been investigated further.

6 Modelling

A number of different types of software have been used in the modelling iteration, as well as some self made post-processing code and support code for generating the needed input files for the simulations. The figure below gives an overview over the modelling process.

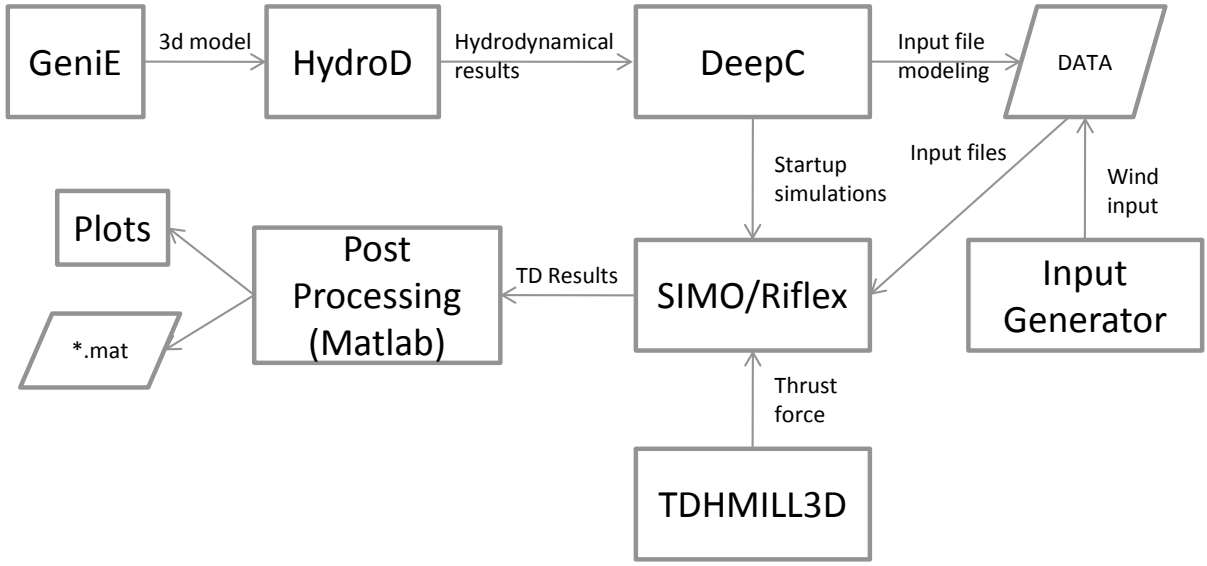

Figure 14 - Descriptive figure of the modelling cycle

First a 3-D panel model of the floating platform was constructed in GeniE. Only the part below the water line was constructed. This model was imported to HydroD, which, based on the geometry and meshed panels of the model, calculates the hydrodynamic properties of the floater. DeepC takes in all the results from HydroD and the 3-D model for visualization purposes. DeepC supports the SIMO/RIFLEX code with a graphical user interface. The mooring system was modelled in DeepC. This included positioning of the fairleads and anchors, and connecting the lines to the floater. The delta lines was modelled a simple spring stiffness in $C_{66}^{Hydrostatic}$.

A visual presentation of the model in DeepC is depicted below.

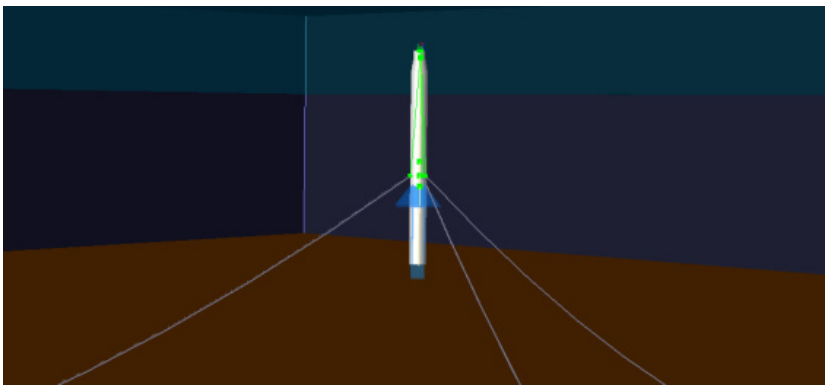

Figure 15 - Spar wind turbine in DeepC

Viscous elements on the floater were also defined together with all the wave environment data. When all the main properties of the model had been defined, DeepC generated the necessary input files for wave analysis in SIMO/RIFLEX. The wind generation and wind turbine part is taken care of by TDHMILL3D, which is a DLL extension to SIMO. Additional input parameters had to be included manually to the input files generated by DeepC to include TDHMILL3D. Due to the many load cases and the need for iteration processes in the modelling, a small executable program was created to automatically insert the necessary inputs for each project in DeepC to include the wind part. This executable was later modified to also include the ability to modify the input files, so that line tensions were saved during simulations, and the ability to copy specific command files that import data to post processing in Matlab. When all input files had been successfully made, start up of simulations was done in DeepC. SIMO/RIFLEX then ran time domain simulations in connection with TDHMILL3D. After the end of the simulation, the results could easily be imported to Matlab for further post-processing.

6.1 Hydrodynamic Model

HydroD was used to solve the hydrodynamic linear potential flow problems of diffraction and radiation. HydroD utilizes the Wadam code which is based on linear methods for marine hydrodynamics solved in the frequency domain. It uses a 3-D panel method to evaluate velocity potentials and hydrodynamic coefficients. HydroD was also used to calculate the mean drift coefficients. This was done through far-field integration (Momentum conservation) in the three horizontal DOFs, surge, sway and pitch.

The output used from HydroD was:

- The solution to the radiation problem which is the frequency dependent added-mass $A_{ij}(\omega)$ and damping $B_{ij}(\omega)$
- The solution to the diffraction problem which is the 1st order wave excitation forces in form of the transfer functions $H_i^D(\omega)$.
- Result of far-field integration which is the mean drift coefficients $\bar{H}_i^{(2)}(\omega)$.

The reader is referred to the HydroD (20) and Wadam (21) user manuals for more theory about solution procedure of the code applied.

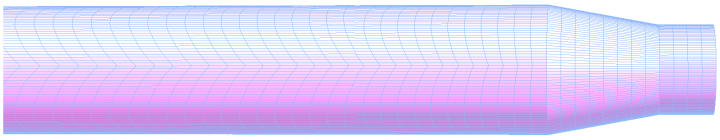

Figure 16: Cut out of the meshed spar in HydroD

The 3D panel model of the floating platform was made in the program GeniE. Only the part under the mean water line was needed to be modelled, since only the hydrodynamic parameters is calculated based on the panel model. Taking advantage of the Spar's planes of symmetry in the xz-and the yz-planes, results in that we only need to model a quarter of the structure. The structure was divided into 3528 elements within a quarter of the body with a denser element distribution near the free surface. This was done to more accurately capture that the fluid pressure has a larger variation near the free surface (ref. Potential theory). The large number of elements is a consequence of the need of sufficiently small element sizes to capture the impact from smaller waves. The number of elements chosen was also based on matching the model of the reference model (1) where 3900 elements were used. Different types of elements available in GeniE were studied to find the best estimates of body geometry and displaced volume. Second order rectangular elements were found to represent the body best, since these elements gave a more correct calculated volume in HydroD compared to regular triangular elements. With this discretization and calculating for 36 frequencies ranging from 0.025 rad/s to 2.05 rad/s and 7 directions ranging from 0 degrees to 90 degrees the computing time was about 8000 seconds.

6.2 Finding Notch Filter Parameters

There are many possible configurations on how the notch filter mentioned in section 3.5 can be tuned. Therefore a study on the filter performance and sensitivity to parameter changes has been done.

The notch filter can be described in the s-plane (or frequency plane if $s = j\omega$) as in the transfer function of Eq.(44). If we let $\omega_0 = \omega_{n_5}$ (natural frequency in pitch) we will always be a constant distance from the origin of the s plane, (Figure 12)

From Eq. (45) we see that an increasing angle θ from the imaginary axis corresponds to larger damping coefficient ζ. We will not study angles outside the region $\theta \in [0, 90]$. For θ between 90 and 180 degrees we will have the same solutions as for 0 and 90 since the solutions are complex conjugates. If we use angles between 180 to 360 degrees (negative values of ζ) we will get poles located at the RHS of the imaginary axis. These poles are unstable and may lead to amplified motions. The cases where $\zeta > 1$ is not of interest either. This is because the solutions will have real parts only and are overdamped which may lead to unwanted frequency filtering.

A summary of the different filter configurations chosen can be seen in Table 4 with the corresponding frequency and phase response and pole-zero locations in Figure 17. As we can see choosing any of the configurations C2-C3 will have the property of cancelling out the notch frequency totally with a zero gain and also give a unit gain at zero frequency ($H(j0) = 1$). With increasing θ from C2 the notch become wider and attenuates more frequencies around the pitch natural frequency. This could be beneficial since the calculations of the pitch natural frequency has uncertainties and is affected by damping. Also nearby frequencies may cause large responses. C5 and C6 do not have zero gain at ω_0 and unit gain at zero frequency and attenuates a large band of frequencies. The poles at the real axis for both C4 and C6 are double. C1 is the configuration with no notch filter.

Table 4 - Definition of cases for the notch filter study

	ζ_N	θ_N	ζ_D	θ_D
C1	-	-	-	-
C2	0	0 deg	0.0785	4.5 deg
C3	0	0 deg	0.7071	45 deg
C4	0	0 deg	1	90 deg
C5	0.1	5.74 deg	0.8	53 deg
C6	0.1	5.74 deg	1	90 deg

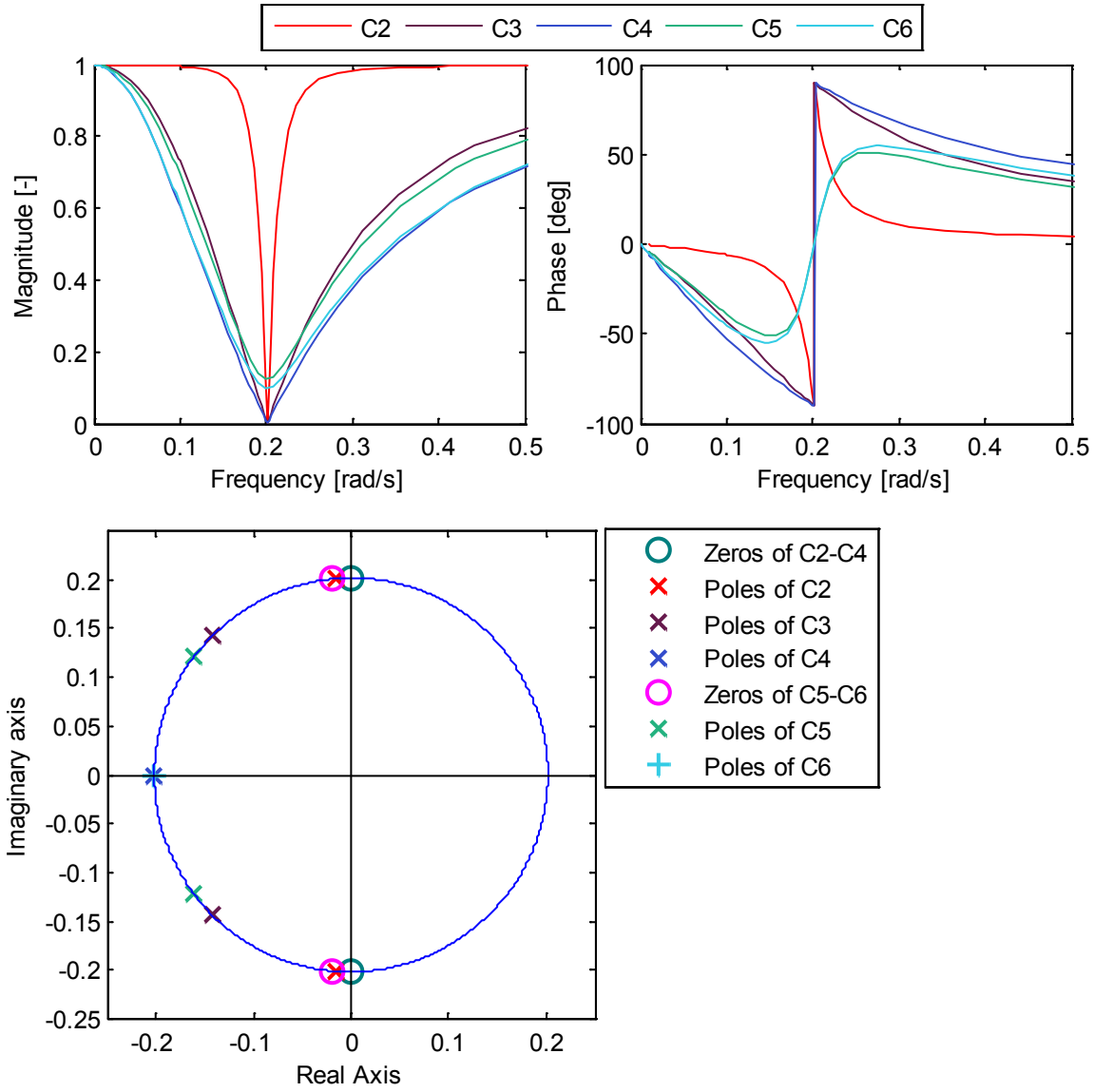

Figure 17 - Pole-zero plot with corresponding frequency & phase plot for each configuration.

All the cases C1-C6 was run for two different load cases (LC3 & LC4 of Table 9) with wind only. As indicators of filter performance the STD of pitch, nacelle acceleration and thrust have been chosen. STD is used because we are trying to lower the dynamic motions and STD measures how much the responses vary around the mean. The results are presented as fraction over the case when we have no notch filter.

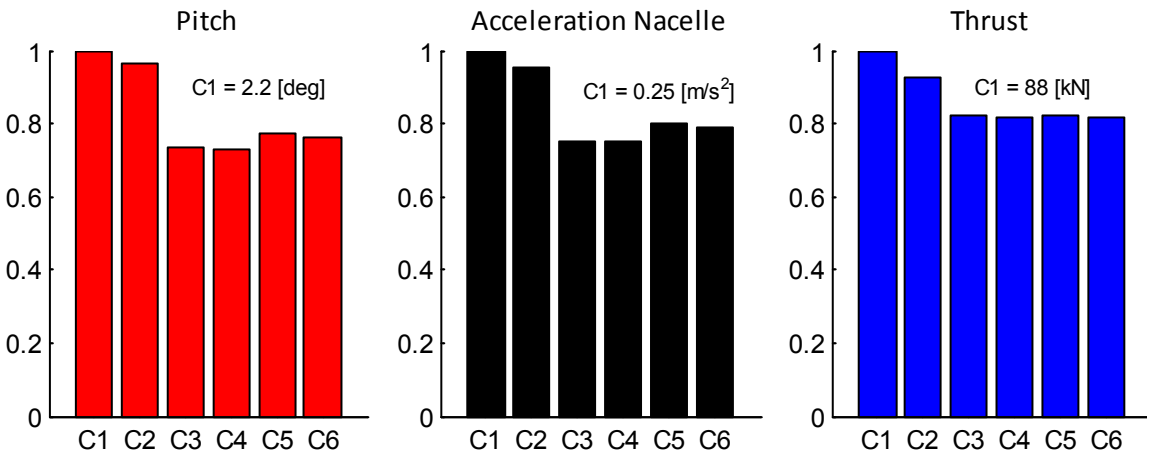

Figure 18 - STD_{Ci}/STD_{C1} **for LC3**

As can be seen from Figure 18 all cases with notch filter damps the floater responses in LC3. The best effect is seen for C3 and C4. C4 is here marginally better than C3. The worst case is C2 with the narrow notch. Cases 5 and 6 where there is a non-zero gain at ω_0 does not perform as well as cases 3 and 4 but the differences are small.

At LC3 the wind is at rated speed and the relative velocity may switch from going into the region where we have positive damping (left of rated) and the region with negative damping (right of rated)(Figure 11). This may possible lead to loss of damping when we are in the left region with an active notch filter. The control system notch filter should perhaps be switched off when this happens, which may give better performance at rated speed.

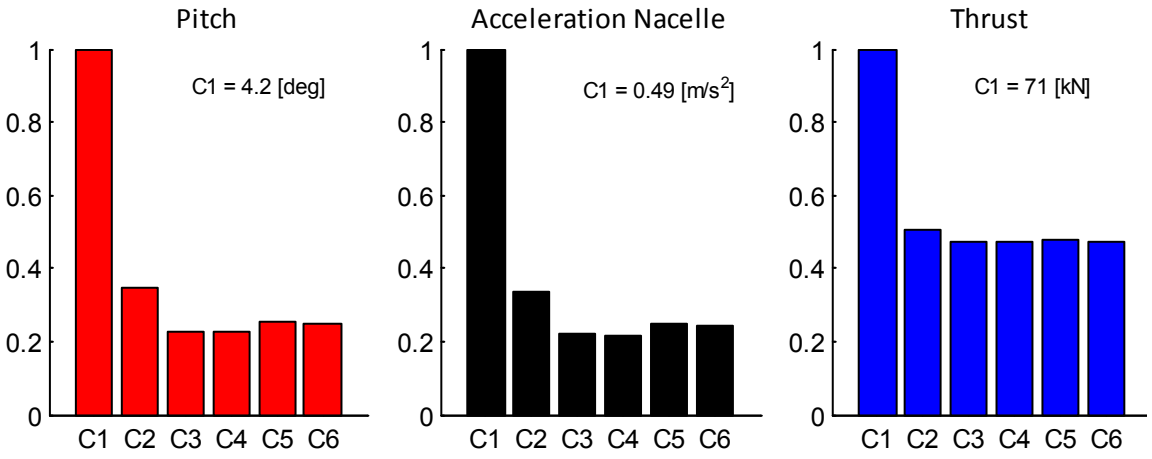

Figure 19 - STD_{Ci}/STD_{C1} **for LC4**

The results from LC4 give a clearer view of the efficiency of the filter. In LC4 we are always in the right side of the thrust curve. All configurations lower both the STD of pitch, and acceleration with over 60 %. We also see that the thrust force STD is considerably lowered. The performance ranking of

the different configurations follows the same sequence as for LC3, with C4 giving the largest decrease in STD for the different DOFs.

The results from this study indicate that it may be preferable to have a filter with a zero gain at ω_0 and some attenuation of the surrounding frequencies.

Since there may be uncertainties in the calculations of the pitch natural frequency it may be valuable to see the effect of varying the corner frequency ω_0 . The following results were obtained by increasing and decreasing ω_0 by 5 % in LC4.The results are presented as ratio increase or decrease in STD for pitch, compared to the ω_0 value used earlier.

Table 5 - Sensitivity of pitch STD with corner frequency

	C2	C3	C4	C5	C6
ω_+	1.93	1.01	1.01	1.01	1.01
ω_-	2.26	1.00	1.00	1.00	1.00

As can be seen the changes in pitch STD are small for C3-C6. The interesting thing is to see how sensitive C2 is to corner frequency. The STD increases around a factor of 2 when the corner frequency differs from the pitch natural frequency. This shows that a too narrow notch is very sensitive to hitting the correct frequency. Still it should be noted that the STDs are reduced from C1 where the filter is not active.

Based on the study presented here the values from C4 will be applied to all load cases where the notch filter is active.

6.3 Time Domain Parameters

The equation of motion is solved in RIFLEX. RIFLEX utilizes an implicit time stepping scheme of the Newmark β family. In addition, Newton Rhapson iterations at every time step assure equilibrium between external and internal forces.

The time integration time step is an important factor and must be chosen based on the specific need of the problem at hand. The Nyquist frequency tells which frequencies that can uniquely be captured using a given time step. The Nyquist frequency corresponds to half the sampling frequency f_s. A time step of 0.2 s was chosen. This gives the ability to capture signals of at most 15.7 rad /s.

It was decided to run one hour simulations. To also account for transient start-ups the simulations was augmented with 1000 s which has been removed from every simulation. The total simulation time was then 4600 s.

The slowest varying loading off significant magnitude on the platform is from the wind. The simulation length sets the limit for the most slowly varying signal we can capture. For our one hour simulations the slowest signal is $2\pi / 3600 = 0.0017$ rad/s which is seen adequate.

The natural frequencies of the floater are placed well beyond these two outer limits. To be sure that the chosen time step was good enough, also smaller time steps have been tested with no notable effects on the results.

The loads cases that will be studied are presented in Table 9 in section 7.3. The table below shows the peak wave periods of the load cases and number of periods the 'peak' wave will undergo during a one hour simulation. Also shown is the number of resonant periods we may see during a one hour period (see Table 7 for natural periods).

Table 6 - Number of wave and motion samples during a one hour simulation

	T_p [s]	# wave periods
LC1	5	720
LC2	9.8	367
LC3	10.1	356
LC4	10.6	340
LC5	14.1	255

	# DOF periods
Surge	29
Sway	29
Heave	115
Roll	116
Pitch	116
Yaw	438

The number of samples during one hour may not be adequate in all cases for calculating reliable statistics especially since we also have wind loads which are more slowly varying than the waves.

7 Results & Discussion

7.1 Hydrodynamics and Structural Results

When combining the properties of the platform and tower structure the resulting COG became,

$$(x_{COG}, y_{COG}, z_{COG}) = (-0.0107\ \text{m}, 0\ \text{m}, -77.6550\ \text{m}).$$

Based on the input data the hydrostatic restoring matrix was calculated as,

$$C_{ij}^{Hydrostatic} = \begin{bmatrix} 0 & 0 & 0 & 0 & 0 & 0 \\ 0 & 0 & 0 & 0 & 0 & 0 \\ 0 & 0 & 3.3355x10^{2}\ \text{kN/m} & 0 & 0 & 0 \\ 0 & 0 & 0 & 1.705x10^{6}\ \text{kNm} & 0 & -8.4794x10^{2}\ \text{kNm} \\ 0 & 0 & 0 & 0 & 1.705x10^{6}\ \text{kNm} & 0 \\ 0 & 0 & 0 & -8.4794x10^{2}\ \text{kNm} & 0 & 9.8340x10^{4}\ \text{kNm} \end{bmatrix}$$

Further the total mass matrix at the origin was calculated to,

$$M_{ij} = \begin{bmatrix} 8.1116x10^{3}\ \text{tonne} & 0 & 0 & 0 & -6.2991x10^{5}\ \text{tonne}\cdot\text{m} & 0 \\ 0 & 8.1116x10^{3}\ \text{tonne} & 0 & 6.2991x10^{5}\ \text{tonne}\cdot\text{m} & 0 & -8.6794x10^{1}\ \text{tonne}\cdot\text{m} \\ 0 & 0 & 8.1116x10^{3}\ \text{tonne} & 0 & 8.6794x10^{1}\ \text{tonne}\cdot\text{m} & 0 \\ 0 & 6.2991x10^{5}\ \text{tonne}\cdot\text{m} & 0 & 6.8234x10^{7}\ \text{tonne}\cdot\text{m}^2 & 0 & 8.424x10^{3}\ \text{tonne}\cdot\text{m}^2 \\ -6.2991x10^{5}\ \text{tonne}\cdot\text{m} & 0 & 8.6794x10^{1}\ \text{tonne}\cdot\text{m} & 0 & 6.8221x10^{7}\ \text{tonne}\cdot\text{m}^2 & 0 \\ 0 & -8.6794x10^{1}\ \text{tonne}\cdot\text{m} & 0 & 8.424x10^{3}\ \text{tonne}\cdot\text{m}^2 & 0 & 1.8787x10^{5}\ \text{tonne}\cdot\text{m}^2 \end{bmatrix}$$

Figure 20 and Figure 21 show the results from the diffraction analysis done in HydroD. The results are for incident waves propagating along the positive x-axis and both the magnitude and phase are shown as a function of wave frequency. The only non-zero components are the forces in surge and heave direction and the pitch moment. Force in sway and moments in roll and yaw are zero due spar symmetry. The excitation forces and moments have peaks around 0.5 rad/s and drops as the frequency increases.

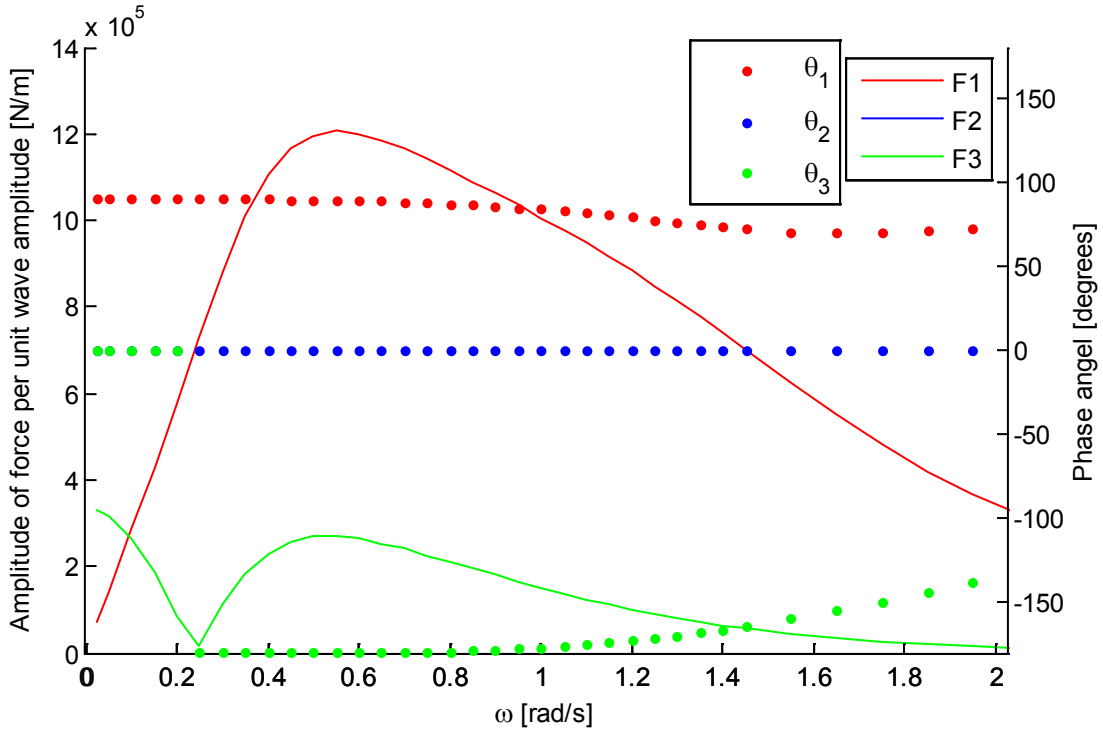

Figure 20- Excitation forces per unit wave amplitude

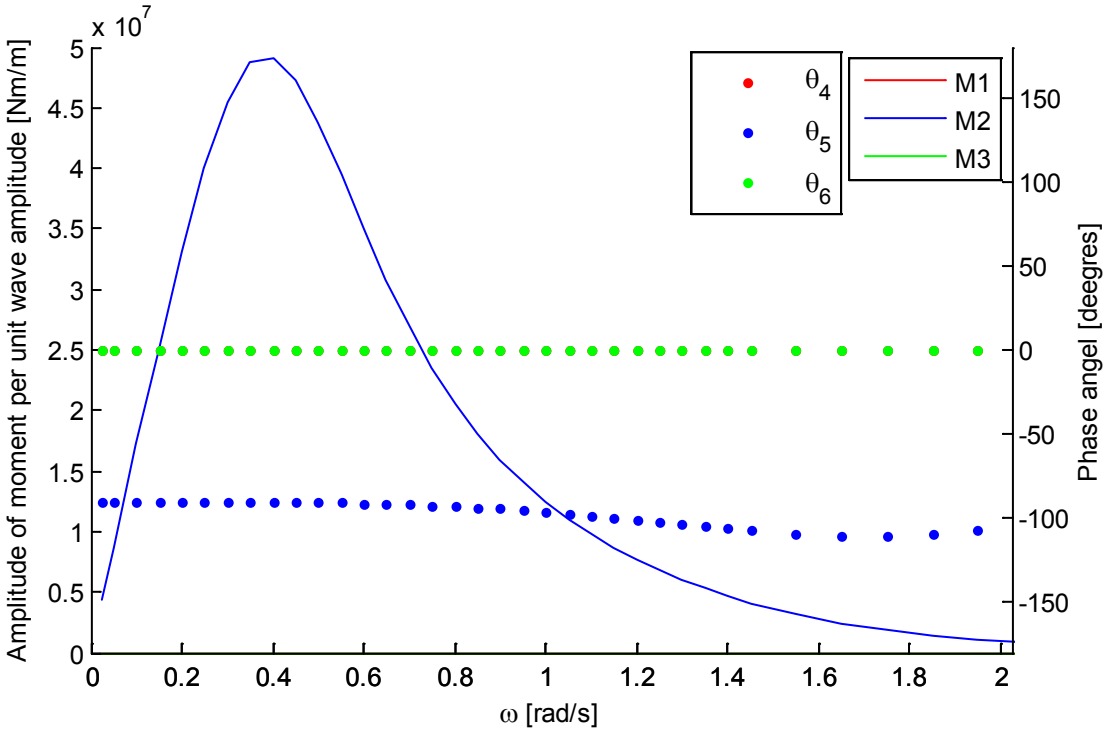

Figure 21 - Excitation moments per unit wave amplitude

I have also included the second order drift forces for the same wave direction. The wave-drift in surge has maximum amplitude at 1.8 rad/s and is zero for frequencies smaller than 0.6 rad/s. Both the sway and yaw components are zero.

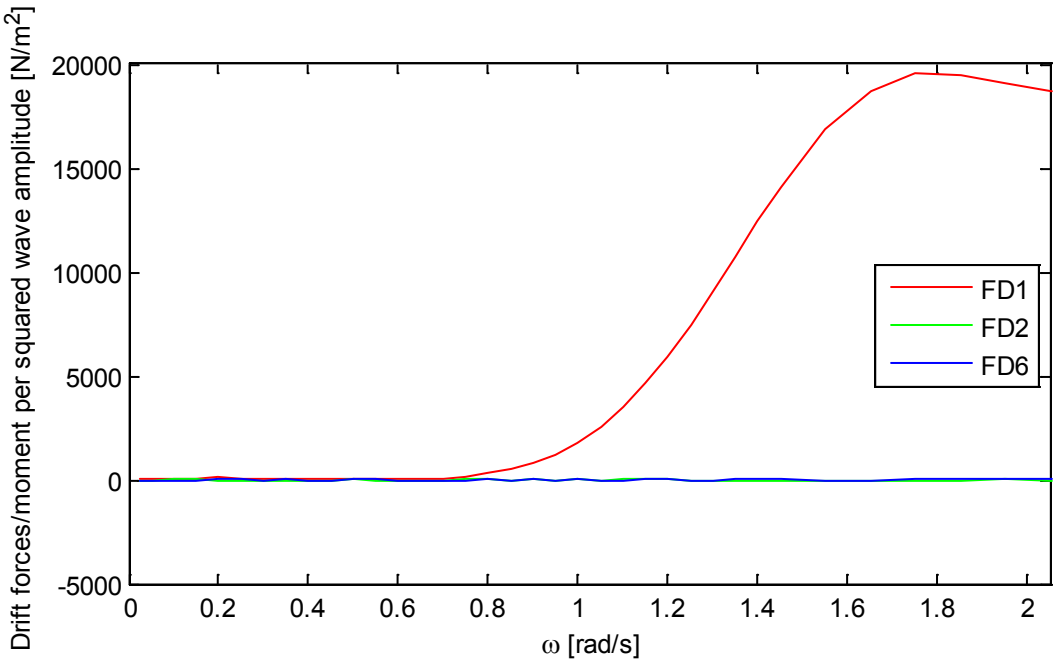

Since the platform is symmetric about the x-z and y-z planes the added mass and damping coefficients in surge due to forced oscillation in surge are the same as for sway due to forced oscillations in sway. The same is true for pitch-pitch and roll-roll. Zero forward speed and current leads to the matrices being symmetric (6). The only non-zero components in both the added mass and damping matrices are the diagonal components and the coupling terms in surge-pitch and sway-roll. The diagonal and the non-zero components above the diagonal are shown next.

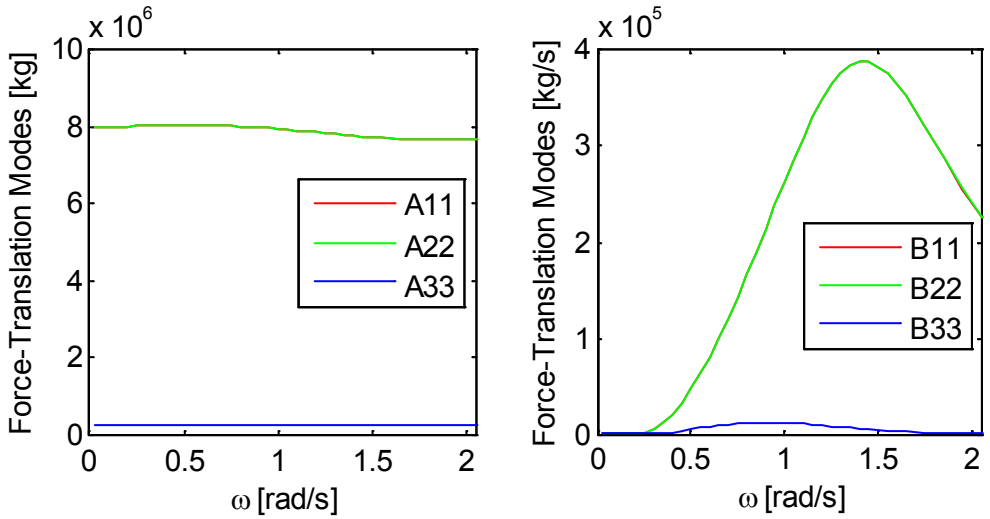

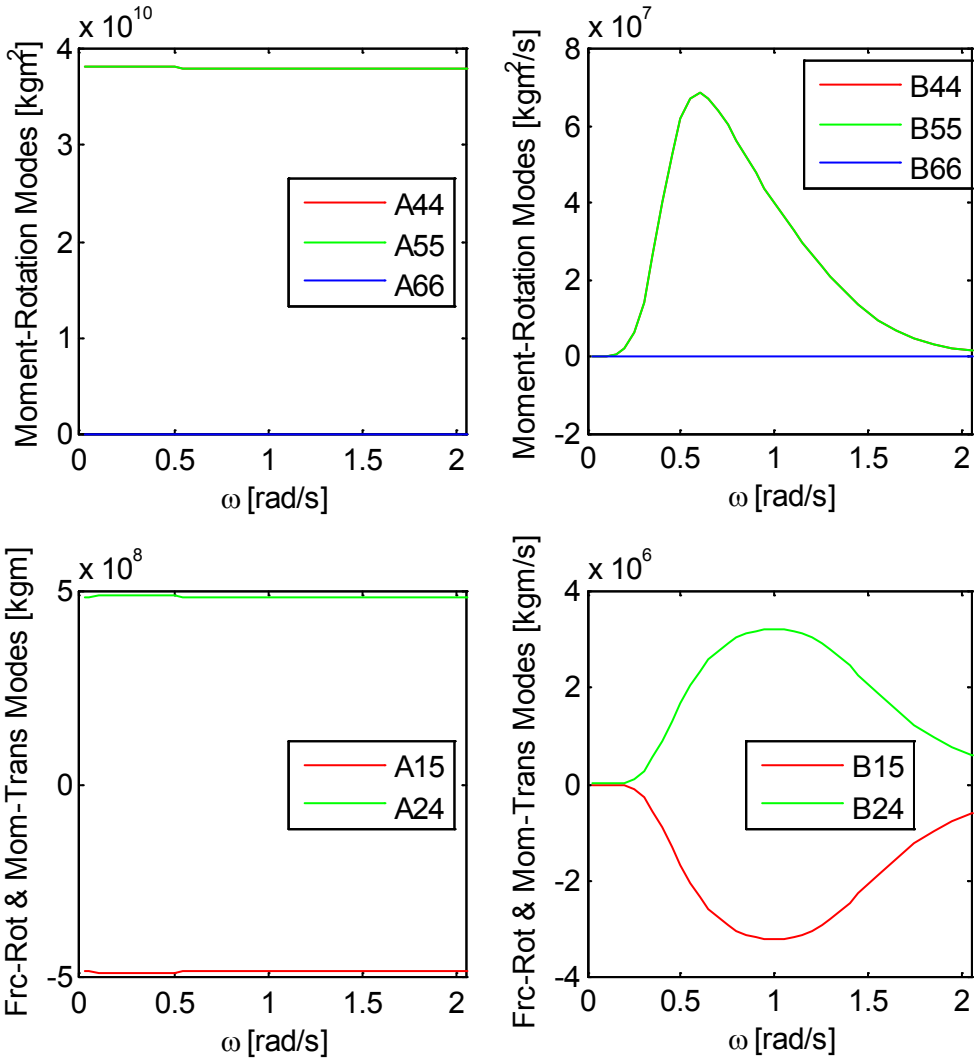

Figure 22 - Added mass and potential damping

The hydrodynamic added mass, damping, restoring matrix and the excitation forces/moments were given in the OC3-Hywind report by J. Jonkman(1). The results in the report and the results presented here compare very well. In the report the hydrostatic restoring matrix is not augmented with the restoring moment $-mgz_G$ in $C_{ij}^{Hydrostatic}$ since the software Jonkman uses account for these components elsewhere. If we remove the restoring moment from $C_{ij}^{Hydrostatic}$ we find the same values as in the report.

7.2 Free Decay Tests

A free decay test is usually performed to find the natural periods and damping coefficients of a dynamical system. The decay test is done by moving the system out of its equilibrium position in one of its degrees of freedoms and releasing it. The system will then oscillate around the original equilibrium position with a damped natural period until the system again reaches an equilibrium

state. By the use of logarithmic decrementation (22) an estimate of the system damping ratio can be found. This estimated value will be an equivalent linear damping ratio for the specific DOF, since our system consists of both linear and nonlinear damping mechanisms. The damping mechanisms involved in our model is linear potential damping and viscous damping from both mooring system and body. The decrementation δ is given by,

$$\delta = \frac{1}{n}\ln(\frac{x_0}{x_n}) \tag{48}$$

where x_0 is an initial amplitude and x_n an amplitude n peaks away. The damping ratio ζ_n is then found through the following relation,

$$\zeta_n = \frac{1}{\sqrt{1+\left(\frac{2\pi}{\delta}\right)^2}} \tag{49}$$

The period of oscillation in the free decay tests are the damped natural periods since no external forces are applied. When the damping ratio is know we can find the undamped natural period ω_n.

$$\omega_n = \frac{\omega_d}{\sqrt{1-\zeta^2}} \tag{50}$$

The decay test was done in DeepC with the fully coupled body and mooring system in still water. To get the system out of equilibrium a constant force was applied at the vertical position of the fairlead in the platform CL for a short duration. The force was directed along the negative x-axis for the decay testing in surge, along negative y-axis for yaw and positive z-axis for heave. For the rotational DOFs a moment had to be applied to perform the tests. This moment was modelled as a small force applied a large distance from the body. Another possibility of modelling a moment would be to apply two forces with opposite direction a distance apart. The former way was chosen because it influenced the other DOFs the least.

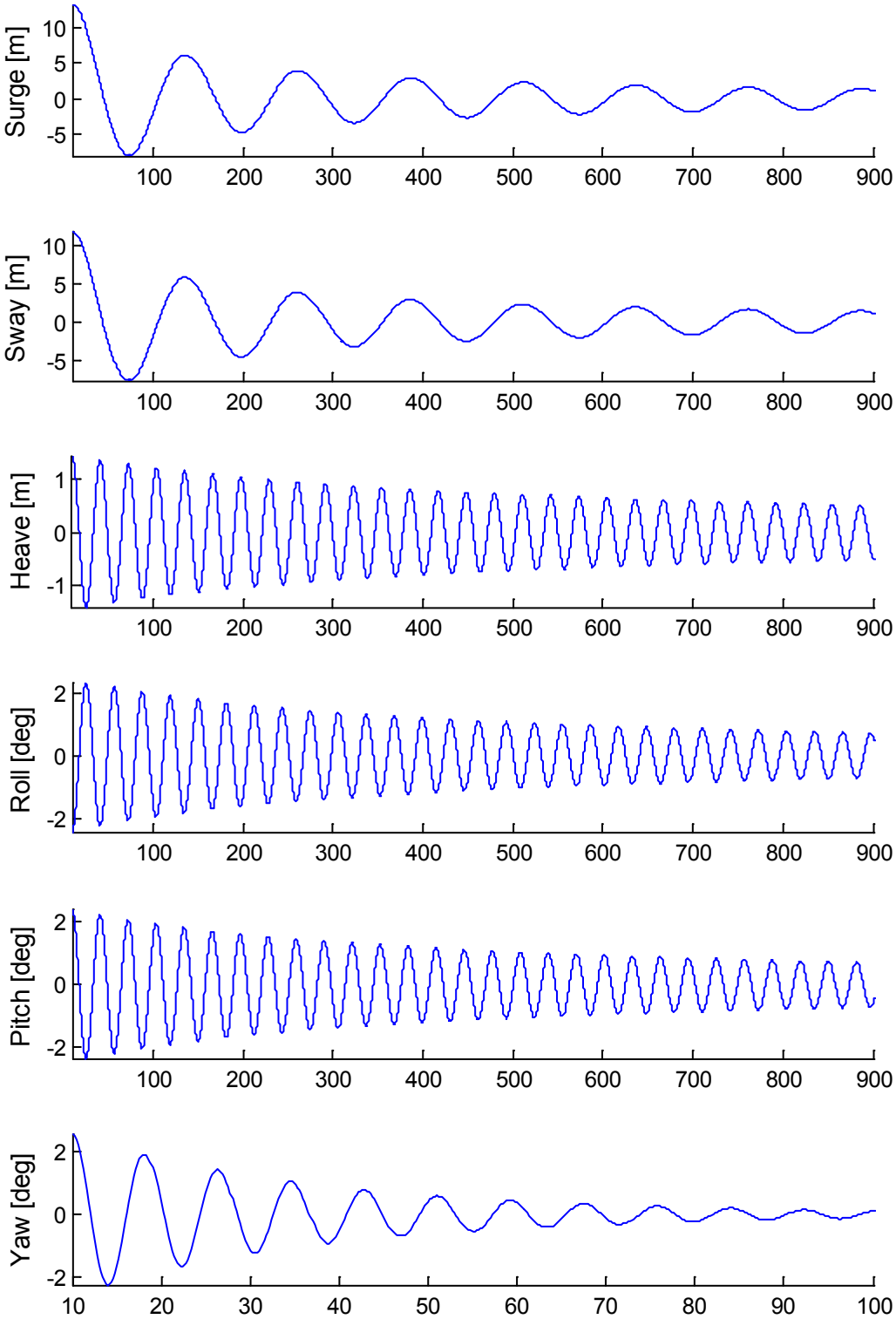

Figure 23 - Time series of decay test

Calculations of the damped natural periods and undamped natural periods showed that the damping ratio is too low to significantly introduce any differences between them.

Table 7 - Natural frequencies of the rigid body modes

	ω_n [rad/s]	T_n [s]	ζ_n [-]
Surge	0.0502	125.27	0.0326
Sway	0.0502	125.20	0.0318
Heave	0.2007	31.30	0.0053
Roll	0.2017	31.15	0.0062
Pitch	0.2018	31.14	0.0062
Yaw	0.7644	8.22	0.0416

The OC3-Hywind rapport (1) did not state the natural frequencies of the reference model, but these were obtained from the master thesis of Matha (23), who reports the results J. Jonkman has found for the OC3-Hywind. The table below shows small discrepancies for most of the frequencies except for roll and pitch where there is over 6 % difference. One reason for these discrepancies can be that the FAST code applied in (23) has flexible tower structure.

Table 8- Discrepancy between natural frequencies

	ω_n ,DeepC	ω_n ,Matha	% discrepancy
Surge	0.0502	0.0503	0.28
Sway	0.0502	0.0503	0.23
Heave	0.2007	0.2036	1.40
Roll	0.2017	0.2149	6.13
Pitch	0.2018	0.2155	6.37
Yaw	0.7644	0.7603	-0.54

7.3 Environmental Load Cases

To study the dynamic response of the floater suitable environmental conditions must be applied. The conditions need to be realistic and span through different severities of sea and wind states.

The environmental parameters is based upon (24) which uses data of simultaneous wind and wave measurements covering the years from 1973-1999 from the northern North Sea.

The chosen load cases are presented in Table 9. In total there are 11 different cases that span a wide region of sea and wind conditions. There are variations in wind speed at the hub (V_{hub}), wind

turbulence (I), significant wave height (H_s), peak period (T_p) as well as different directions of wind and waves. The 0 degree direction is defined so that the wave and wind are moving along the positive x-axis. The directional angles are defined positive in the counter-clockwise direction.

Table 9 - Load case table

	V_{hub} [m/s]	I [-]	H_s [m]	T_p [s]	Wind/wave directions [deg]	Notch filter
LC1	4	0.15	1	5	0 / 0	No
LC2	8	0.15	2.5	9.8	0 / 0	No
LC3	11.4 (rated)	0.1	3.1	10.1	0 / 0	Yes
LC4	18	0.1	4.4	10.6	0 / 0	Yes
LC5	50	0.1	12.7	14.1	0 / 0	No
LC30-3	11.4 (rated)	0.1	3.1	10.1	0 / 30	Yes
LC30-4	18	0.1	4.4	10.6	0 / 30	Yes
LC30-5	50	0.1	12.7	14.1	0 / 30	No
LC90-3	11.4 (rated)	0.1	3.1	10.1	0 / 90	Yes
LC90-4	18	0.1	4.4	10.6	0 / 90	Yes
LC90-5	50	0.1	12.7	14.1	0 / 90	No

The corresponding wave and wind spectres for all LCs are plotted in Figure 24. The wave spectrum values for LC5 have been reduced by 40 % in the figure to get a clearer view of the other cases.

LC1 and LC2 are considered mild conditions and wind speed is below rated. Motions are expected to be small for both these cases. This is especially visible when looking at the wave and wind spectrums for those cases compared to the more severe states.

LC3 is situated at the rated wind speed with 0.1 turbulence intensity. The wind speed at the hub will vary below and above rated. The thrust curve of Figure 11 shows that thrust is at its maximum for this mean wind speed. A significant wave height of 3.1 m is still not considered large and the wave spectral density is mostly concentrated around the same frequency ranges as for LC1 and LC2.

LC4 is above rated wind speed. The maximum thrust here is less than for LC3, even though wind speed is higher. Wave heights have increased. By inspection we can see that the wave spectrum for this case spans a much larger area and frequency range than compared to the other cases discussed.

LC5 is our extreme load case with significant wave heights as high as 12.7 m and wind speeds of 50 m/s. The rotor is parked in this condition with the blade chord parallel to the wind direction. Both the wind and wave spectrum are much larger in size and with significant energy spread around a large frequency range.

The remaining load cases consider occurrences where there is an offset in wind and wave directions. As will be shown later these cases contribute to large motions for the floater.

Figure 24 also shows approximate locations of the six natural frequencies of the floater rigid body motions. The effect of their location will be discussed more in the details in the different load analysis studies. See Table 7 for more accurate values of the natural frequencies.

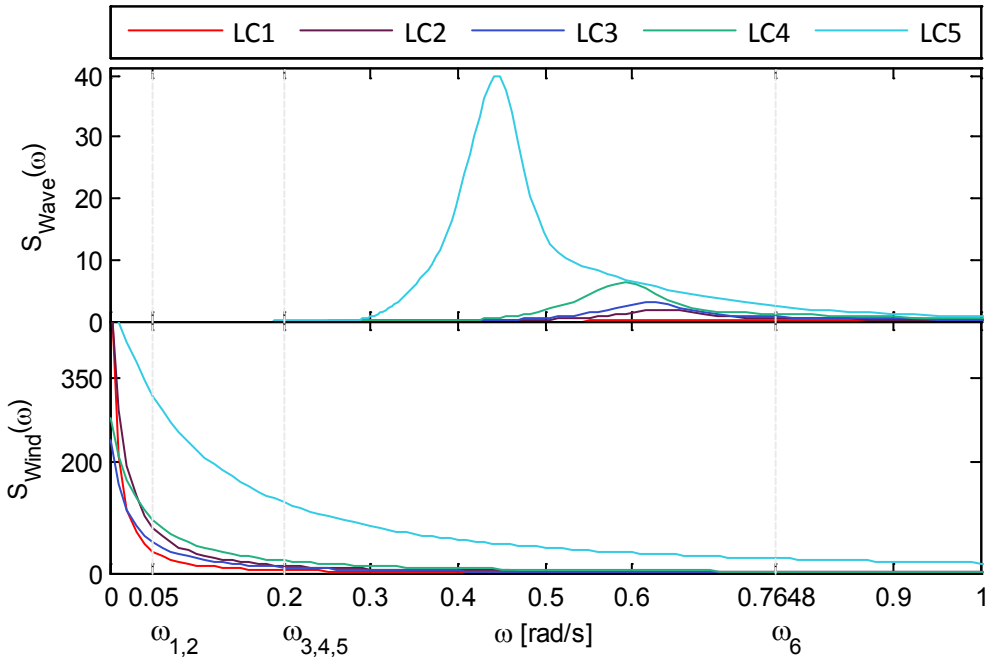

Figure 24 - Wave & wind spectrums for all LCs with approx. positions of natural frequencies

7.4 Load and Response Analysis

Following is the statistical results of a selection of DOFs for all the different load cases. In addition, time series and spectrums from LC3 to LC5 and LC30-3 can be found in appendix 1. A DVD containing all the time series and spectrums for all defined load cases is also included in the report.

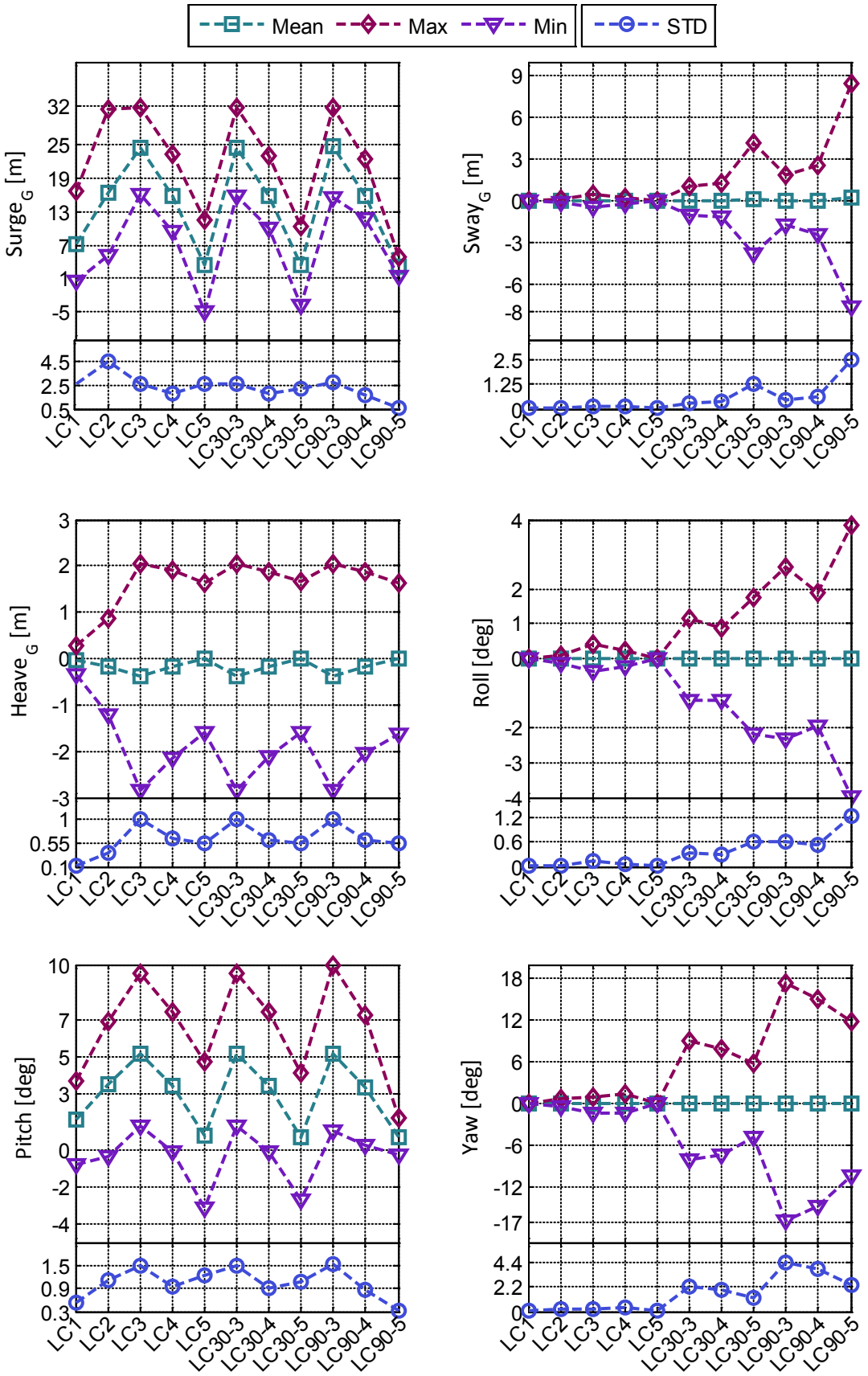
Mean
Max
Min
STD
Surge$_G$ [m]
Sway$_G$ [m]
Heave$_G$ [m]
Roll [deg]
Pitch [deg]
Yaw [deg]
LC1
LC2
LC3
LC4
LC5
LC30-3
LC30-4
LC30-5
LC90-3
LC90-4
LC90-5

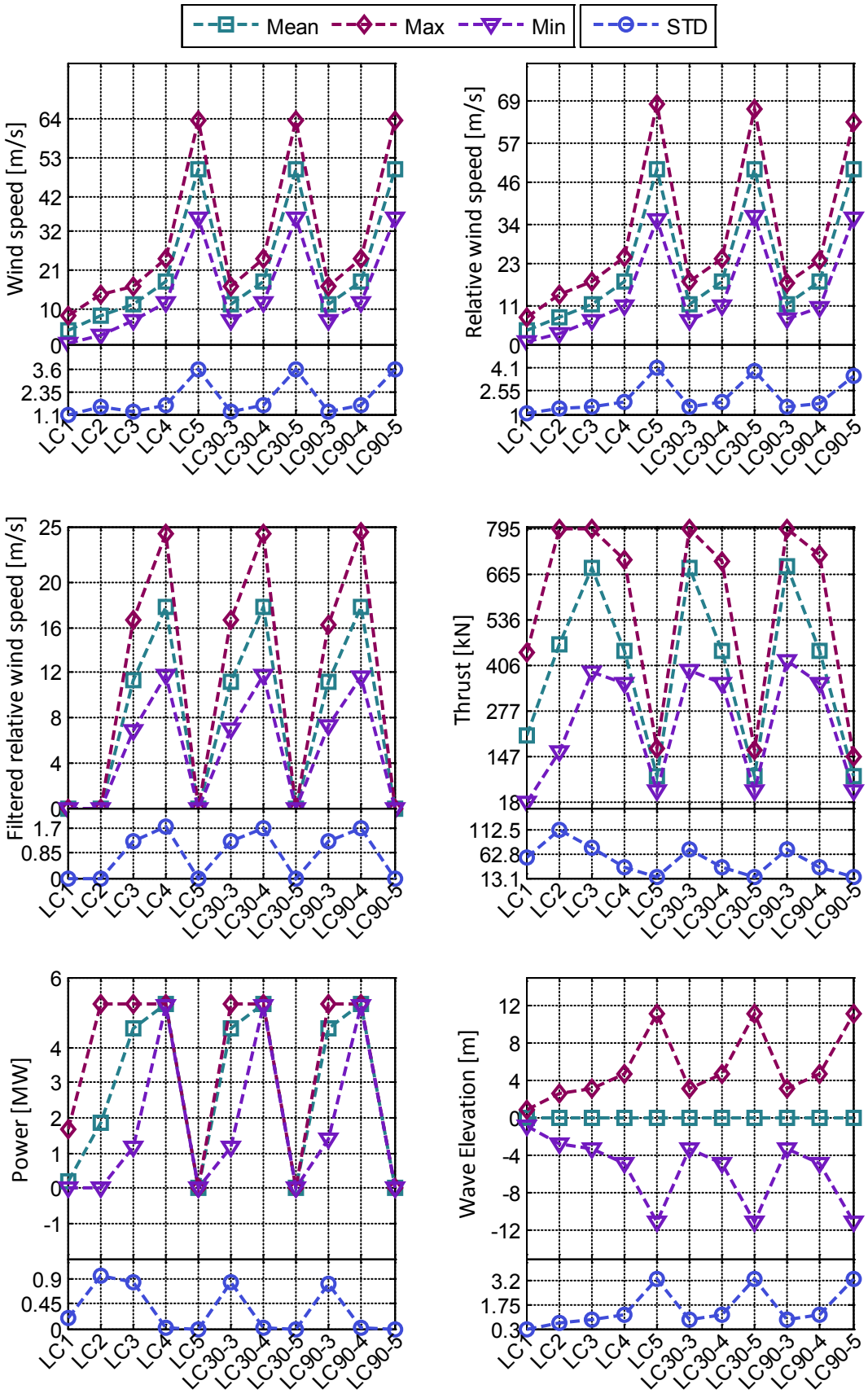
Mean
Max
Min
STD
Wind speed [m/s]
Relative wind speed [m/s]
Filtered relative wind speed [m/s]
Thrust [kN]
Power [MW]
Wave Elevation [m]
LC1
LC2
LC3
LC4
LC5
LC30-3
LC30-4
LC30-5
LC90-3
LC90-4
LC90-5

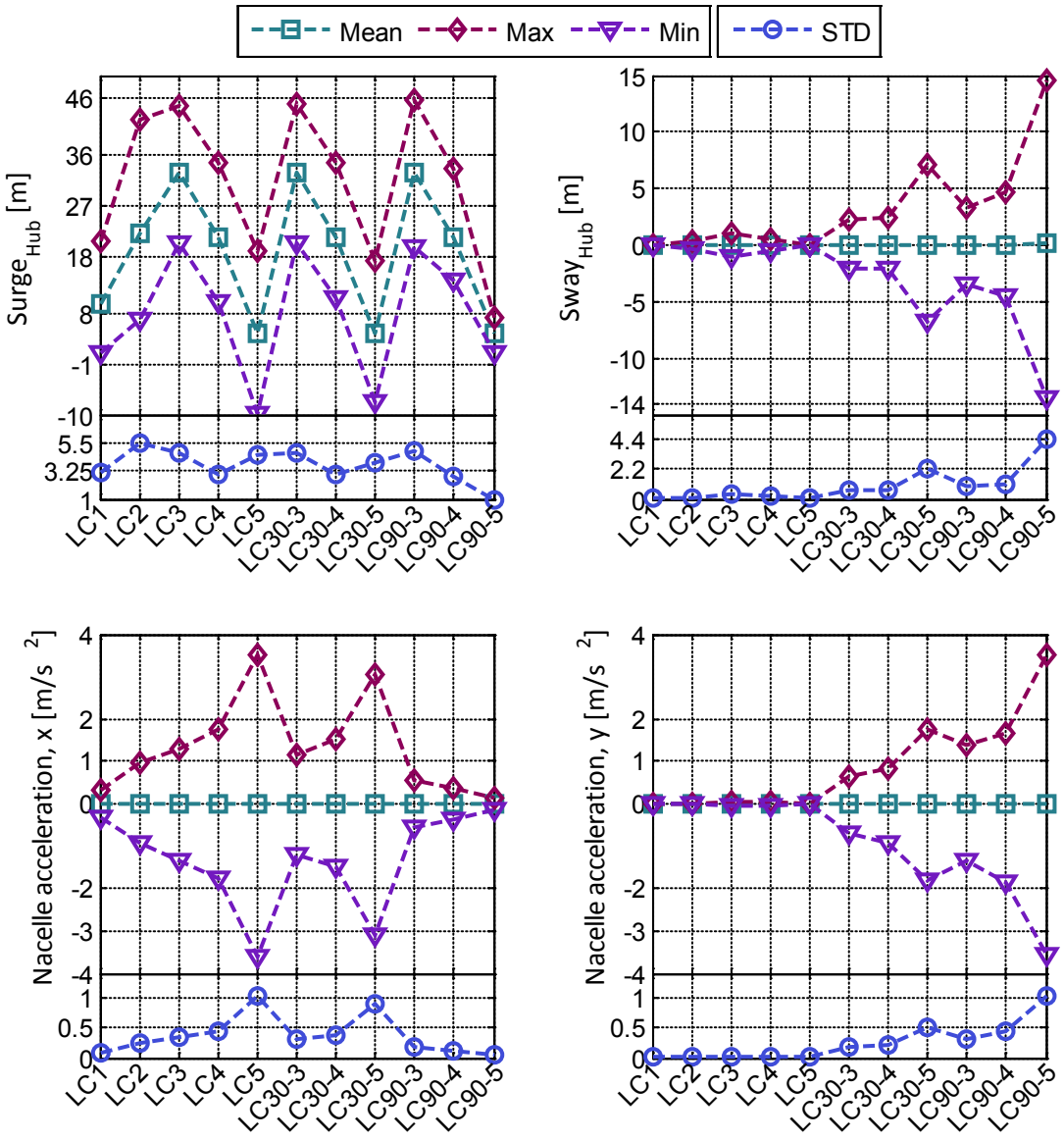
Mean
Max
Min
STD
Surge$_{Hub}$ [m]
Sway$_{Hub}$ [m]
Nacelle acceleration, x [m/s^2]
Nacelle acceleration, y [m/s^2]
LC1
LC2
LC3
LC4
LC5
LC30-3
LC30-4
LC30-5
LC90-3
LC90-4
LC90-5

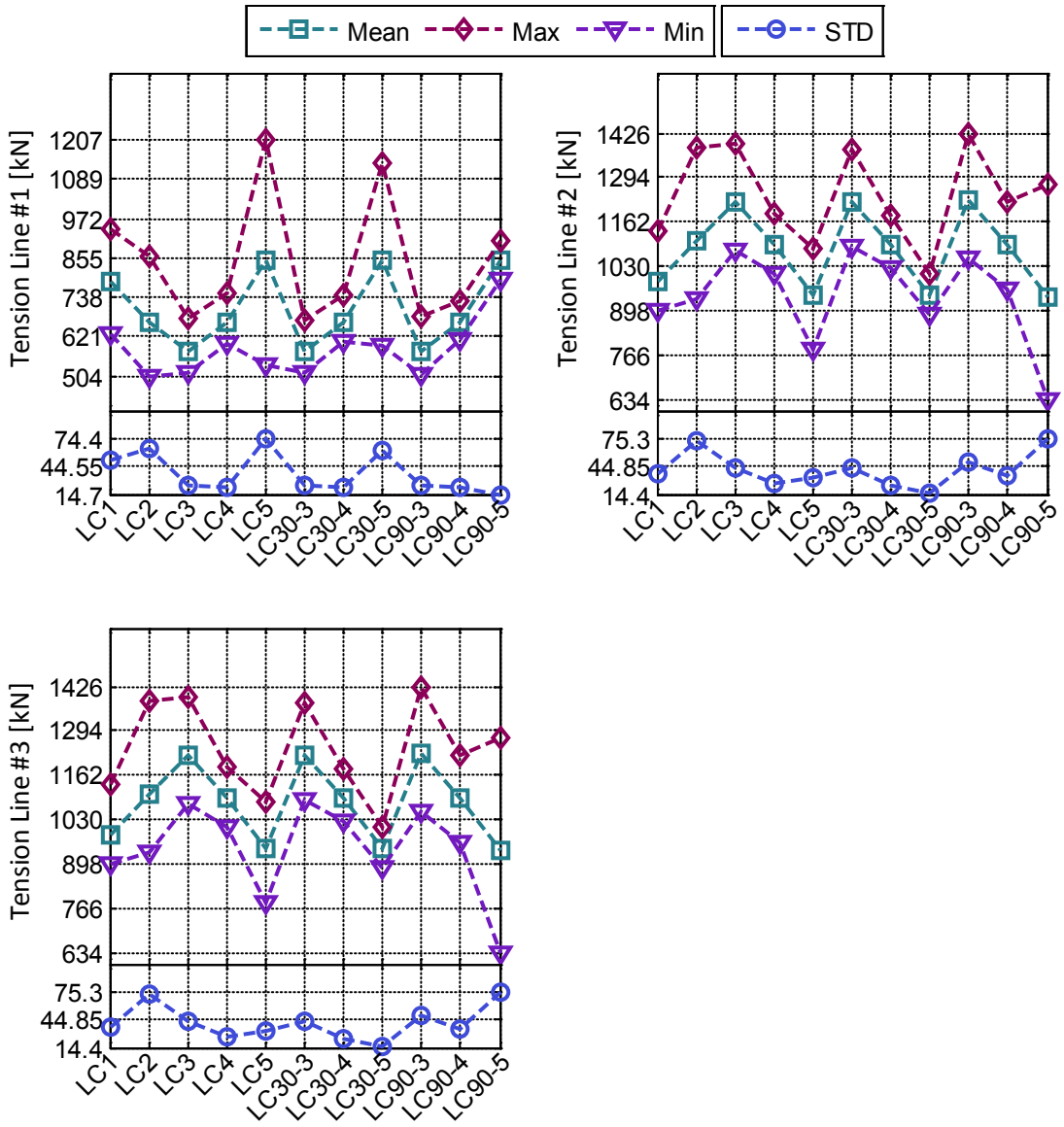
Mean
Max
Min
STD
Tension Line #1 [kN]
1207
1089
972
855
738
621
504
74.4
44.55
14.7
Tension Line #2 [kN]
1426
1294
1162
1030
898
766
634
75.3
44.85
14.4
Tension Line #3 [kN]
1426
1294
1162
1030
898
766
634
75.3
44.85
14.4
LC1
LC2
LC3
LC4
LC5
LC30-3
LC30-4
LC30-5
LC90-3
LC90-4
LC90-5

7.4.1 Discussion of Non-Directional Cases

In the following discussion three abbreviations will be used. LF, WF and HF. WF stands for wave frequency, LF for low frequency, and HF for high frequency. WF is defined as the frequency region where waves have significant spectral density. LF includes all frequencies below WF, while HF includes all frequencies above WF. Thrust is mainly in the LF region, but may also have components for some cases in the WF region. The slowly varying wave forces may excite in the LF region for surge and sway.

The results from the load and response analysis, where waves and wind are propagating in the positive x - direction, will be discussed in this section. This includes the results of load cases LC1 through LC5.

The mean surge and pitch positions are dominated by the mean thrust force given by the mean relative velocity in each load case. Due to the floater having a low COG (-77.65 m), a large portion of the surge motion at the origin is due to pitch. There is a steady increase in the mean surge and pitch position with increasing environmental state severity up to LC3 at rated speed. The mean thrust force is at its greatest at rated (681 kN) and declines for relative wind speeds above rated. This explains the drop in mean positions above LC3. In LC5 the rotor is parked, but there is still a wind force acting on the blades. The mean thrust force is only about 92 kN in this condition, which is much lower than for the other state, resulting in a small mean position of 3 m and 0.73 degrees in surge and pitch, respectively.

Figure 24 shows that the waves in LC1-LC5 have no significant energy around the floater natural frequencies, except for yaw. Since the floater is symmetric, there will be no wave forces/moments that can directly excite this motion. The wind speed spectrum, on the other hand, has significant density for all cases 1 through 5 situated around all the natural frequencies.

The thrust force STD increases from 54 kN in LC1 to a maximum of 112.5 kN in LC2. In the surge spectrum in LC1 and LC2 there are excitations around the surge natural frequency with some small contributions around pitch natural frequency, due to the coupling at the origin mentioned. The excitations from the waves are very small compared to the LF region for both LC1 and LC2. Since the slowly varying drift forces are relatively small for low wave heights, most of the contributions surge LF part is believed to be thrust induced, and the surge motion STD peaks in LC2. The turbulence intensity is 0.15 with mean wind speed of 8 m/s for LC2. This leads to large spectrum densities in the LF region, where the thrust mainly excites, and at and around ω_1, with following surge resonance excitations. Pitch excitations follow a similar pattern as surge, with thrust being the dominant contributor for LC1 and LC2.

Further, the surge STD drops for LC3 and LC4, while pitch STD increases to a maximum in LC3. The turbulence intensity is for these two cases reduced to 0.10, and we have wind speeds of 11.4 m/s and 18 m/s. The sea state severity has also increased, and the density spectrums of the waves are larger with the spectrum peak situated at lower frequencies (Figure 24). Excitations in surge are still thrust dominated for both cases, but there is now a large increase in surge motion due to the coupling in pitch. This is especially visible in LC3. As can also be seen, the excitations around the surge natural frequency are lower than for LC2 in both cases. This can be related to the reduction in density of the thrust spectrum (See decrease in thrust STD), especially around the surge natural frequency. The total effect is that surge excitations are reduced from LC2 through LC4.

As mentioned, the pitch STD does not follow the same pattern as for surge, and it increases from LC2 to LC3. There is some wave induced pitch motion in the WF part for LC3, but this is still small compared to the thrust in the LF part, and of similar size as in LC2.The spectrum density of wind speed in LC2 is actually higher for all frequencies, including around the pitch natural frequency, than for LC3, and the thrust STD decreases from 112.5 kN to 74 kN. The important difference here is the density of thrust around pitch natural frequency. The density has increased from the combined effect of the thrust curve being at its maximum and that the relative velocity, which is highly dependent on the pitch motion, has large resonance excitations. The reason for these high pitch excitations can be related back to the discussion in section 3.5. The thrust slope above rated speed is so that it may contribute to negative damping of pitch, leading to amplified motions. LC4 has a similar spectrum in pitch as LC3, but with a small increase in the WF part and lower values around pitch natural frequency. The reduction here is a combination of the notch filter working efficiently, since we are always on the above rated side of the thrust curve, and that the thrust magnitudes are lower than for rated speed in LC3.

Figure 24 shows that LC5 is much more severe than the other cases, at least with respect to waves. The spectrum density values are spread out around a large band of frequencies for both wind and waves. The wind spectrum has large densities in the WF part for this environmental condition, but looking back at the thrust curve in Figure 11, the thrust magnitudes are low. There is, as mentioned before, a strong correlation between which frequencies the highest thrust densities are situated at, and the frequency components in the relative velocity. For LC5 it is mostly waves that contribute to the motions at the hub, and the thrust will therefore be large in the WF part (Study thrust spectrum, LC5). The total STD in surge is here lower than for all other cases, except for LC4. Pitch STD also increases from LC4 to LC5. This is as for surge, related to the effect of the larger 1^{st} order wave forces/moments combined with thrust (mainly drag in LC5) excitations. There are still some resonance excitations around pitch natural frequency, but the peak value is significantly smaller than for LC3 and LC4, where pitch was influenced by negative damping.

The floater experiences small excitations in heave for all the load cases, even though there is low damping for this DOF. The non-zero mean position in heave, for some cases, may be influenced by

the coupling to pitch and roll at the origin. The largest heave motions are in LC3 at rated, and even when the waves are at their largest in LC5, the motions are still limited.

As mentioned before, there are no wave forces that can directly cause the platform to yaw. This is also the case for sway and roll, when the waves are propagating along the positive x axis in LC1-LC5. Still, the results show some sway, roll, and yaw excitations for all load cases, besides LC5. There are several effects that can give moments around the z -axis of the floater, resulting in excitations in yaw. The first one is the gyro moment from the spin of the rotor, when the floater has an angular velocity around the y -axis (floater is pitching). Secondly, if the floater rolls, there will be an arm from the position of the thrust force to the origin of the body, resulting in a yaw moment (Refer to Eq. (9) and Eq.(43)). Also the asymmetric mooring configuration can contribute to moments around the z - axis. This will be discussed further in the directional cases. The sway, roll and yaw motions in the non-directional cases appear because, at simulation start, the floater will begin to pitch, resulting in an angular velocity around the y -axis with a following yaw moment from the gyro effect. This causes the floater to yaw, and some roll motion will occur, resulting in a yaw moment from the thrust. The sway motions that occur are results of coupling to roll at the origin, and of thrust applied in positions where the floater has non-zero yaw angles, since thrust follows the rotor plane (follower force). The thrust induced yaw moment is believed to be the largest contributor to these yaw motions. The floater in LC5 does not experience any sway, roll, or yaw, since the rotor is shut off so that no gyro moments will start the coupled motions, and the loads on the mooring lines are purely symmetric.

A small discussion around mooring line tension is also valuable. Figure 3 shows the mooring line configuration. In LC1-LC4 it is line #2 (L2) and line #3 (L3) which are the lines that are experiencing the highest tensions and line #1 (L1) in LC5.

The largest tension STD for the operational cases is in LC2. This is also when surge STD is at its max. In the tension spectrum it is the LF part that is the main contributor for LC1-LC4, and specifically around surge natural frequency. The largest tension is found in LC3, when the mean value is at its highest. This is also when the thrust mean force is at its highest. In LC3 and LC4 there seems to also be some influence around pitch natural frequency. In LC5 the floater has its lowest mean position. L1 is now the mooring line that has the largest tension and STD. It is now the WF part that dominates. Over all the load cases, LC5 has the largest tension STD, LC3 the max tension.

7.4.2 Discussion Directional Cases

The discussion in this section relates to the cases where wind and waves come towards the floater from different directions.

Mean positions in surge and pitch are basically unchanged from their corresponding non-directional cases, since it is mainly the mean thrust force that influences theses DOFs. The mean positions of sway and roll are nearly zero for all the directional cases. A small sway mean position of 0.2 m is noticeable in LC90-5. The mean position of heave is unchanged for the directional cases.

The STD of surge and pitch are not very influenced by directionality in LC3 and LC4. The small changes are in the WF part, and they are reduced with increased wave attack angle. Since these DOFs are mainly influenced by thrust in LC3 and LC4, the changes in STD are small. For LC5 there is a more pronounced drop in STD with directionality, since the surge and pitch are mainly induced by waves in LC5. It is also interesting to see that the thrust contributions in the WF part mentioned earlier disappear for LC5 when directionality is increased.

Heave motion is, as before, not excited much, and there are no large differences in statistics between non-directional and directional cases.

The sway and roll DOFs are naturally more involved when waves are no longer propagating along the positive x-axis. It can be seen that yaw motion is also excited in these cases. The STDs in both sway and roll increase with increasing directionality for a given load case. This is related to increase of the WF part, since waves are not only along the x-axis in these cases. Small contributions around the sway natural frequency, due to the slowly varying drift force in sway, are visible in the directional cases.

Yaw motions are largest in LC90-3 with a STD of 4.36 degrees and maximum angles around 17 degrees. Studying the spectrums in roll, pitch and yaw for LC3, LC30-3 and LC90-3, two contributions in yaw are visible. There is the double peak around 0.2 rad/s, and the larger WF region, which also stretches around yaw natural frequency of 0.76 rad/s (Figure 24). The spectrum values around yaw natural frequency show that the yaw DOF is experiencing resonance oscillations. Considering this part it can be noted that for LC90-3 pitch does not oscillate with frequencies in the WF region, while roll do. Due to these roll motions, the thrust force induces moments about the z-axis at these frequencies and at the natural frequency in yaw, resulting in amplified yaw motions. The double peak around 0.2 rad/s in LC3 is also present in both directional cases, but it is not visible, since it is the WF part that dominates there. The peak coincides with the roll and pitch natural frequency. The contributions of density around 0.2 rad/s are likely to be a combined effect of coupling in yaw through, the gyro moment with pitch and thrust with roll. Another effect that may also be contributing to yaw motions is the mooring system. Running LC90_4 with wave's only results in yaw motions. The motions were small with STD of 0.09 degrees and max angles of about 0.3 degrees. Calculating the horizontal decomposed force of the line tensions gives a non-zero force in the x-direction in this case. This force can induce a moment about the z- axis if the platform pitches or

rolls. Even though the motions are small, but this illustrates that also the mooring lines contribute to yaw motions, and that this DOF is coupled in many ways.

In a later section, the effect of increasing yaw stiffness and moving the yaw natural frequency further away from the WF part will be studied.

For the offset cases it is L2 and L3 that experiences the largest tensions in all the load cases except in LC30_5. The general trend is for LC3 and LC4, that the changes in tension STD is not large between 0 and 30 degrees, but increase when there is a 90 degree offset. In LC5, L1 has the largest STD for the 0 and 30 degree cases, but not for 90 degrees

7.5 Notch Off

Running the load cases with the filter off also for wind and waves gives a good understanding on how it influences the pitch motions.

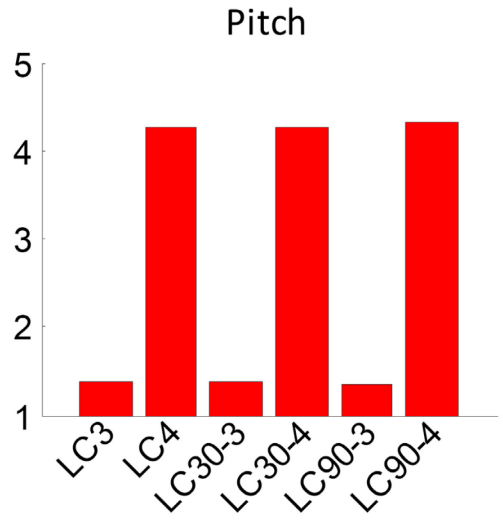

Figure 25 - $STD_{\text{Notch Off}} / STD_{\text{Notch On}}$ **for the relevant load cases**

The largest difference in pitch STD is in LC4. Running the turbine without the notch filter results in a pitch STD over 4 times larger than the same case with the filter active. The pitch excitations are not reduced or amplified more in the directional cases.

Figure 26 shows the difference in spectral density for the case with notch filter off and on, around the pitch natural frequency. There is clearly a reduction of spectral density around pitch natural frequency due to the filtering of relative velocity.

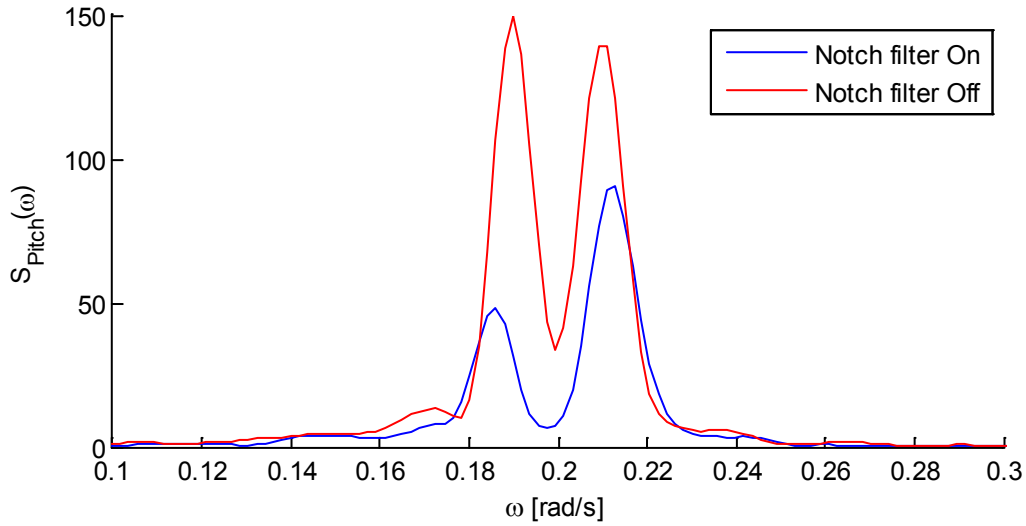

Figure 26 - Difference in spectral density around pitch natural frequency for LC3

7.6 Stochastic Variance

There will be uncertainties in the statistics of a time domain simulation since there are many coupled effects, and a change in say phasing of the waves would result in a different time history for the motions. This is the motivation for running multiple simulations with different random seeds for the same load case scenario of wind and wave. The more simulations computed the better convergence is the basic assumption.

10 simulations for LC3 and LC4 have been conducted here. Referring back to Table 6, our sample populations will now be 10 times larger for these DOFs providing more reliable sample statistics.

The statistical results for each DOF are plotted as cumulative averages. This type of average is given as (25):

$$CA_i = \frac{x_1 + \ldots + x_i}{i}, \quad CA_{i+1} = \frac{x_{i+1} + iCA_i}{i+1}, \text{ where } CA_0 = 0 \tag{51}$$

The reason for using this type of average is that it will show how the x_i values converge with increasing i .

The standard statistical descriptions mean, STD, max and min are well know, but kurtosis and skew will also be introduced here. Short described, skewness measures to which degree a distribution departs from symmetry. A positive skewed distribution has a tail which is pulled in the positive direction and negative skew in the negative direction. Kurtosis measures the degree of peakedness of a distribution. A standard Gaussian distribution has 0 skewness and kurtosis of 3 (26).

Linear waves are generated as zero mean Gaussian processes. If we were only considering linear theory and waves, the motions of the floater would also be Gaussian distributed (27). Since we have introduced non-linear effects and thrust, it would be interesting to see how good the DOFs fit a Gaussian distribution.

The results for the 6 body DOFs are presented in appendix 2. The results can easy be misinterpreted since the magnitude of the values on the y-axis provides different number of significant digits for different DOFs and statistical measure. This may provide the feeling of the curve to be diverging in some cases. If these curves are studied closer, for most cases the difference between the y values for each horizontal step is small, and have in fact converged to at least 1 significant digit (e.g. for 0.01234 3 significant digits are 1,2 and 3 and for 1234.5 1, 2, 3). The concept of significant digits will be important here since different DOFs have very different magnitudes (28) (1000 kN compared to 0.5 degrees). A good way to study these graphs is through visual inspection. Convergence will here be defined as when the cumulative average has at least 1 constant significant digit for the last 3 seeds.

The strategy chosen for investigating this convergence criterion has been to:

- By visual inspection go through all the statistics for each DOF and mark those cases where the slope from seed 8 to 10 is large.
- For the marked cases study the values for the seeds 8 through 10 and study if there is convergence.

A small discussion is presented around the results in the following.

Mean values

The mean values do not vary much from each simulation. By visual inspection 5 seeds in LC3 and about 7 seeds in LC4 are needed to get a mean value with at least 3 significant digits.

Standard deviation

For estimation of STD more samples are needed than for means. LC3 seem to need at least 5 seeds to get 2 significant digits and LC4 need at least 10 seeds to at least show some stable values for most DOFs. Roll motion in LC4 does not converge to at least one digit. Since roll motion is small for this

load case it is not considered important. Another interesting observation is the STD of pitch and heave, which have a very steep slope and only convergence to 1 significant digit.

Max values

For the max values many DOFs was marked due to their large and unstable slopes, but closer inspections revealed that most values had converged to 2 significant digits for LC3 and 1 digit for LC4. By just looking at the marked cases it seems that the heave motion sets the base for how many seeds are needed. For 2 or more significant digits one should use 10 seeds or more if one wants to be sure, that the results are stable in both load cases. Scrolling through the max values the trend seems to be lower max values with increased seeds in the cumulative averages.

Min values

Min values seem stable for LC3 except for the filtered relative velocity with only convergence to 1 significant digit. In LC4 heave is again marked. As for max values, 10 or more seeds are advisable.

Skew

Skew need large samples and this is reflected in many DOFs being marked. For most DOFs there is convergence to 1 significant digit. Other DOFs like surge, sway, sway at the hub, acceleration in y-direction and roll does not converge for LC3. All these DOFs except surge, have values close to zero.

Kurtosis

Many cases that were marked had converged to 2 significant digits. Only pitch and roll of the 6 body modes had less than 2 significant digits for LC3. It is likely that at least 10 seeds are needed for convergence to at least 1 significant digit for both load cases.

As a final presentation in this section the results of skew and kurtosis for the 6 DOFs will be shown.

Table 10 - Skew and kurtosis for 6 DOFs in LC3 and LC4

	LC3		LC4	
	Skew [-]	**Kurtosis [-]**	**Skew [-]**	**Kurtosis [-]**
Surge	-0.15	2.90	0.07	2.95
Sway	0.00	2.60	0.00	2.59
Heave	0.01	2.45	0.01	2.76
Roll	0.00	2.62	-0.01	2.66
Pitch	-0.04	2.71	0.05	3.11
Yaw	-0.08	3.14	-0.03	3.13

None of the DOFs totally fulfils the mentioned properties of a Gaussian distribution. The closest to a Gaussian distribution is surge in LC4 with a skew of 0.07 and kurtosis of 2.95.

7.8 Depth Change

The reference model was originally designed for a depth of 320 m. To also check the feasibility of the concept in shallower waters the system was taken from 320 m to 160 m. The main change to the system for this new depth is the mooring setup. The hydrodynamics of the floater are assumed to not change considerably, so the same hydrodynamic results have been used in this study.

The strategy chosen in changing the mooring system was to try keeping the dynamical responses as similar as possible to the original depth. To get similar responses it was determined to change the mooring line system so that it preserved the natural frequencies it had for the original depth. This will give similar responses for smaller displacements (linear region).

The same type of mooring lines was used. This means that the line stiffness, hydrodynamic coefficients and weight/length was kept constant. The changes done to the mooring system were:

- Changing the vertical anchor position from 320 m to the new seabed at 160 m.
- Changing the unstrecthed line length.
- Changing floater ballast until still water position is reached.

The total line length was iterated on until the new catenary shape provided a stiffness that resulted in a similar natural frequency in surge. The iteration procedure resulted in a new length of 868.19 m which is about 96 % of the original value. The resulting and original natural frequencies are summarized below.

Table 11 - Natural frequencies at new depth

	$\omega_{160\,\mathrm{m}}[\mathrm{rad/s}]$	$\omega_{320\,\mathrm{m}}[\mathrm{rad/s}]$	$\omega_{160\,\mathrm{m}} / \omega_{320\,\mathrm{m}}$
Surge	0.0492	0.0502	0.98
Sway	0.0516	0.0502	1.03
Heave	0.2023	0.2007	1.01
Roll	0.2014	0.2017	1.00
Pitch	0.2015	0.2018	1.00
Yaw	0.7363	0.7644	0.96

As Table 11 shows the surge natural frequency differs from the value at the original depth by 2 %. Further iteration on the line length did not give a closer value due to the natural frequency being very sensitive to changes in line length.

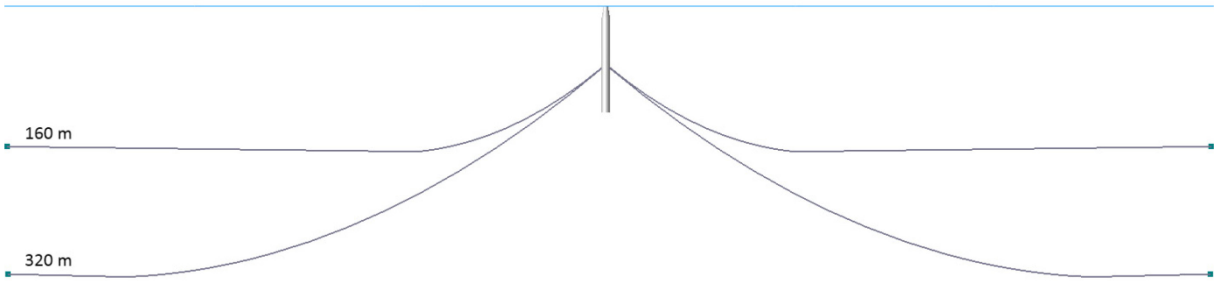

Figure 27 - Sketch of the two mooring system. Only two out of three mooring lines are shown.

The mooring line configuration sketch in Figure 27 shows two very different catenary shapes for the two cases. A much larger portion of the new mooring system is resting at the sea bed. Further iteration could be done on the system by e.g. moving the horizontal position of the anchor closer to the still water position of the floater. This would reduce the line length and could reduce the mooring line costs considerably without changing system stiffness. This type of optimization was not conducted here since the main goal is to show that the concept may also be suitable in shallower waters.

All the load cases of Table 9 were run at the new depth. To illustrate the performance at this depth a few key parameters are presented for the first five load cases. Blue is original and grey new depth.

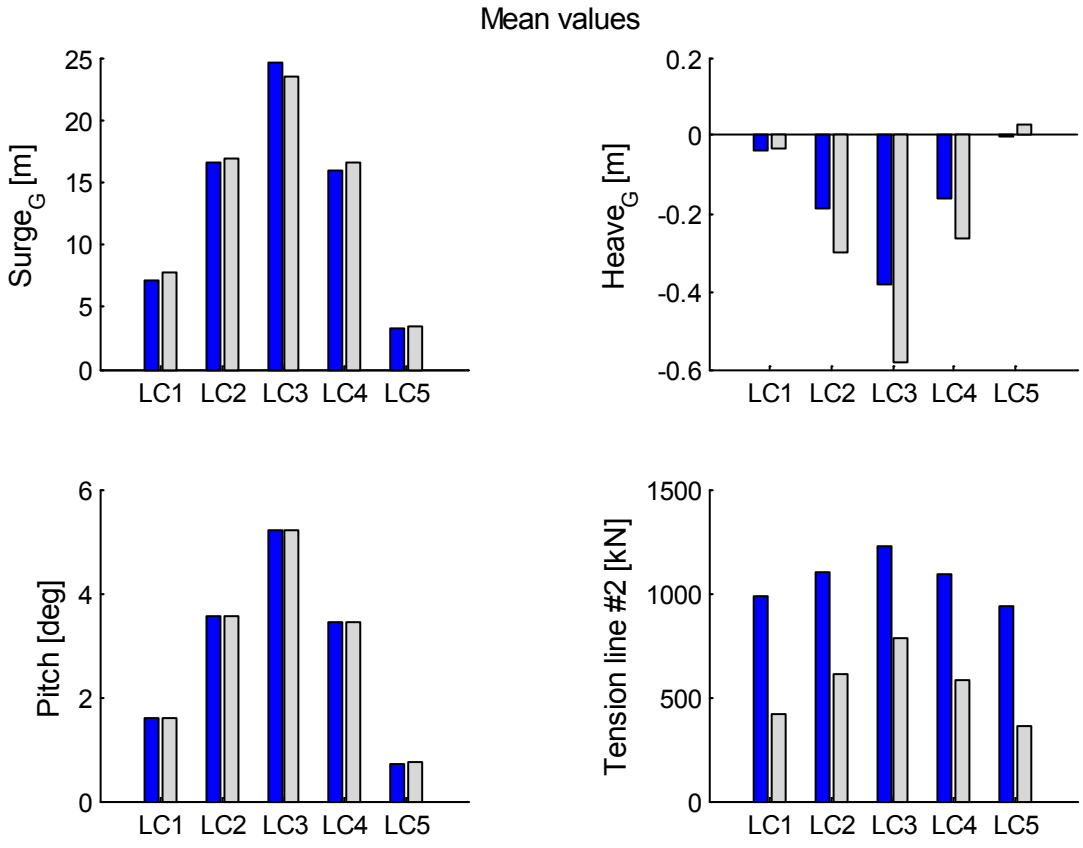

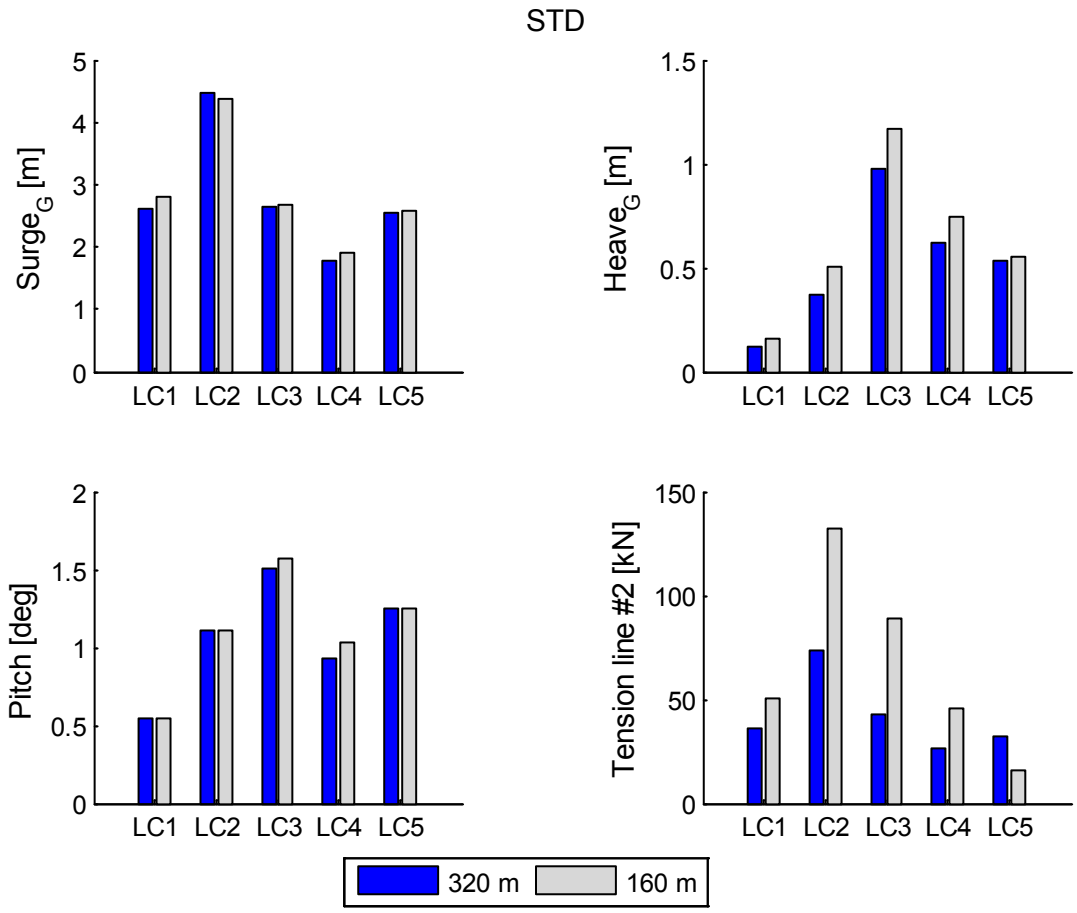

Figure 28 - Key parameters from new depth

There are no significant changes in the mean values of surge, heave and pitch. Mean tension on the other hand is considerably lower at the new depth. In LC1 the mean tension is more than 50% lower. Changes in surge STD are also small with a 10 % increase for LC4. There are some larger excitations in heave, but the oscillations are still small. That pitch motion is not affected by the mooring lines is noticeable when we see that pitch STD is relative unchanged. STD in tension has noticeable increased for all cases, except LC5. This increase in STD could result in decreased lifetime of the mooring lines due to fatigue. The mooring lines have been designed for 320 m so if the same line is to be used at 160 m the max tension here should preferably not exceed the values for 320 m so we are sure that we are below maximum strength.

Table 12 - Max tension [kN] for wind ward line

	LC1	LC2	LC3	LC4	LC5
320 m	1136	1381	1397	118	1083
160 m	636	1113	1065	741	439
Ratio	0.56	0.81	0.76	0.62	0.41

As Table 12 shows the maximum tensions at 160 m is below maximum tensions for 320 m case.

7.9 Yaw Motions Sensitivity to Yaw Stiffness

The load and response analysis showed that large yaw motions occurred when the floater experienced roll motion due to waves. If we were to increase the stiffness in yaw, the yaw natural frequency will be moved further to the right and away from the WF region. The model uses a linear stiffness contribution in $C_{66}^{Hydrostatic}$ to represent the yaw stiffness from the delta lines. Two new values for $C_{66}^{Hydrostatic}$ has been used here to change the natural frequency in yaw. If it is possible to realize this stiffness physically has not been investigated, so these analyses should be looked upon only as a sensitivity study on the placements of the yaw natural frequency. The results from running the load case LC4-30 ($T_p = 10.6$ s) with the two new systems, C1 and C2 including the original system are presented next.

Table 13 - Results from increased yaw stiffness

	Original	C1	C2
$C_{66}^{Hydrostatic}$ **[kNm/rad]**	98340	165040	273440
ω_6 **[rad/s]**	0.76	0.98	1.26
T_6 **[s]**	8.2	6.4	5.0
STD Roll	0.28	0.20	0.18
Max Roll	0.87	0.71	0.66
STD Pitch	0.62	0.57	0.55
Max Pitch	2.46	2.49	2.43
Std Yaw	1.97	0.77	0.33
Max yaw	7.78	2.91	1.54

The floater has strongly coupled DOFs so changing one parameter leads to different time history of others. This is also infuenced by the thrust being dependent upon floater motions. The STD in roll and pitch is reduced, but the angles are still small. The largest changes can bee seen for yaw. Maximum yaw angles are lowered by a factor of 2.7 and 5 for C1 and C2 compared to the original values respectively. To illustrate the effect time series and spectrum plots of the three different cases are presented below.

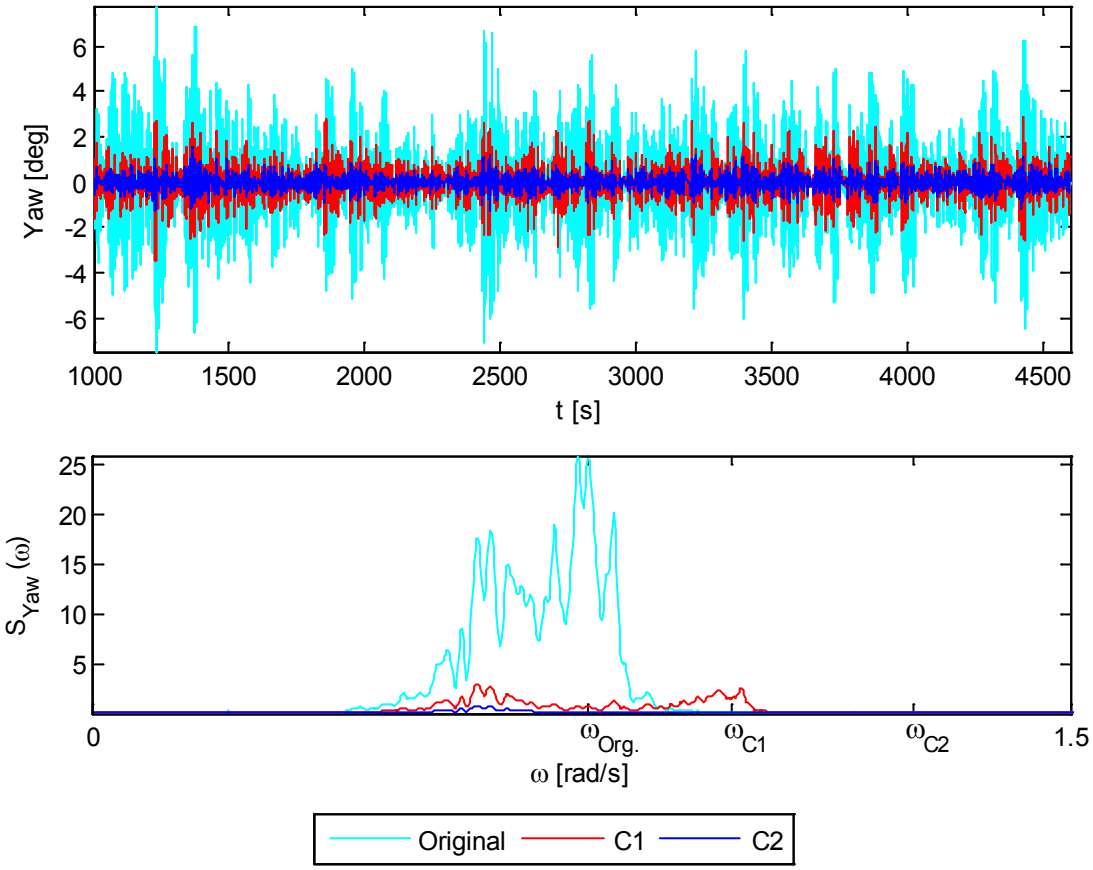

Figure 29 - Time series and PSD of yaw with different stiffness

The spectrum plot clearly shows how the yaw motions reduce when its natural frequency is moved away from the WF range. Due to this just being an example study for one load case, there is no guarantee that the yaw motions will be less for other conditions.

8 Comparisons of Three Concepts

Two fellow master students have also been studying offshore floating wind turbines, but have been working on different floater concepts. These concepts include a tension leg platform (TLP) and a semi-submersible (SS).

All concepts have been modeled in the same manner by using the same software. Results are hence based on the same theory and are applicable for comparison. The analyses have been performed with the same random seeds, resulting in equal time series of wave heights and wind speeds.

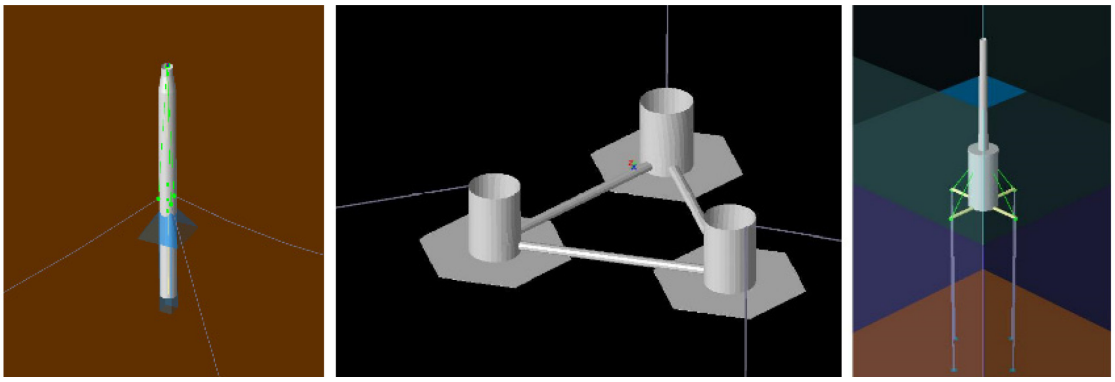

Figure 30 -The three concepts as modelled in DeepC

8.1 Tension Leg Platform

The TLP is based upon NREL's modification of a TLP design from MIT (23). The platform is cylindrical and ballasted with concrete. The mooring system consists of 8 vertical tendons mounted in pairs at the ends of two spokes at the bottom of the structure.

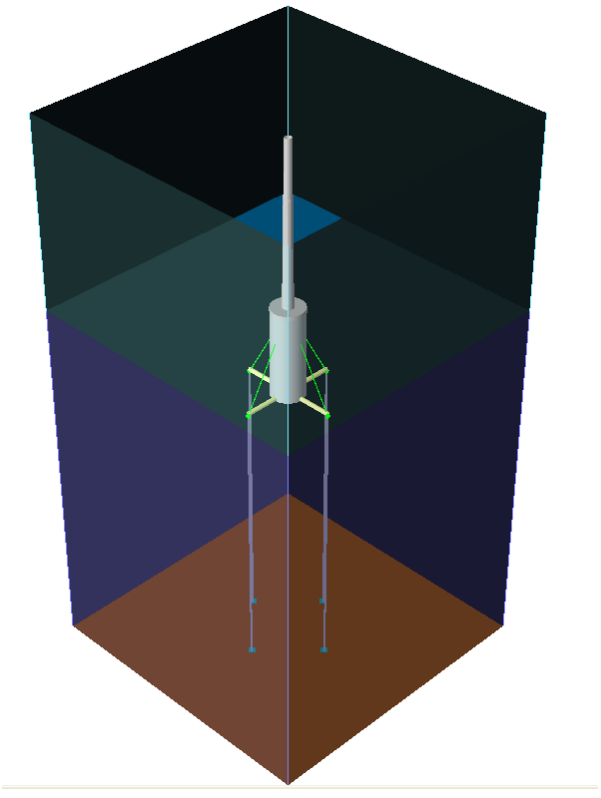

Figure 31 - TLP

The next two tables state the main parameters of the floater and mooring configuration. The values presented are the sum of all parts of the system, so they include the tower and wind turbine.

Table 14 - Main parameters of the TLP

Draft	47.89 m
Diameter	18 m
Mass	9296.9 tonne
Displacement	12180 m^3
COG from SWL [m]	(0.001, 0, -32.59)
Roll inertia about origin	18.59E+06 kgm^2
Pitch inertia about origin	18.57E+06 kgm^2
Yaw inertia about origin	0.3852E+06 kgm^2
Location of hub from SWL [m]	(0, 0, 90)
Water Depth	200 m

Table 15 - Mooring overview, TLP

Mooring Configuration	8 (4 pairs)
Depth to fairleads, anchors	47.89 m, 200 m
Radius to fairleads, anchors	27 m, 27 m
Unstrecthed line length	151.7 m
Line diameter	0.127 m
Line mass density	116 kg/m
Line extensional stiffness	1.5E+06 kN

For more information regarding the TLP concept the reader is referred to the report by Lygren (29).

8.2 Semi Submersible

The Semi Submersible (SS) is based on Principle powers Windfloat design. The platform is composed of three columns, with heave plates at each column for additional damping in heave, pitch and roll. The wind turbine structure is located at one main column as shown in Figure 32.

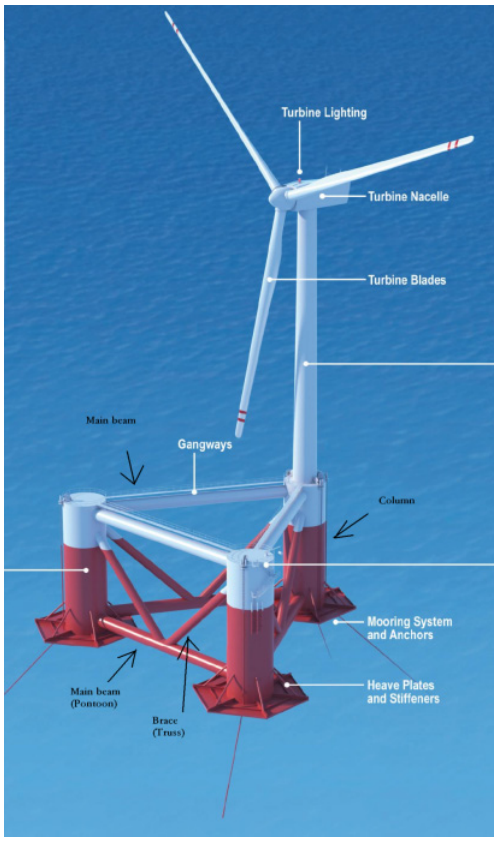

Figure 32 - Semi-Submersible (SS)

Two mooring lines are attached at the main column, and one is attached at each of the sub-columns. The Principle Power design also included an active ballast system which is not considered here.

The main parameters of the concept and mooring configuration are summarized in the following tables. As for the TLP, the values are related to the full system with the wind turbine attached.

Table 16 - Main parameters of SS

Draft	17 m
Column Diameter	10 m
Mass	4640 tonne
Displacement	4504 m^3
COG from SWL [m]	(-0.28, 0, 3.73)
Roll inertia about origin	5.65E+06 kgm^2
Pitch inertia about origin	5.59E+06 kgm^2
Yaw inertia about origin	3.26E+06 kgm^2
Location of hub from SWL [m]	(26.56, 0, 89)
Water Depth	325 m
Number of columns	3
Other info	Heave plates on columns

Table 17 - Mooring overview, TLP

Mooring Configuration	4 x catenary lines
Depth to fairleads, anchors	0 m, 325 m
Unstrecthed line length	1486 m
Line diameter	0.38 m
Line mass density	168 kg/m
Line extensional stiffness	1.53E+06 kN

For more information regarding this floating wind turbine concept the reader is referred to the report by Chenyu (30).

8.3 Results & Discussion

The results from the comparison study consist of combined statistical plots for a number of DOFs. These are placed in the appendix 3. In addition, time series and density spectrums can be viewed in the two reports mentioned earlier (30)(29). The DVD following this thesis will also contain these time series and spectrums in the same format as the ones that are presented in the appendix for the Spar.

In the following discussion three abbreviations will be used to make the discussion easier to follow. All references to the Spar concept will be stated as SP, and similarly, all references for the Semi-Submersible and tension leg platform will be stated as SS and TLP, respectively. The following table and graph shows the location of the three platform's natural frequencies.

Table 18 - The natural periods/frequencies of all the three concepts

	Spar		**Semi-Sub**		**TLP**	
	$T_{SP:i}$ [s]	$\omega_{SP:i}$ [rad/s]	$T_{SS:i}$ [s]	$\omega_{SS:i}$ [rad/s]	$T_{T:i}$ [s]	$\omega_{T:i}$ [rad/s]
Surge	125.27	0.0502	134.70	0.0466	65.00	0.0967
Sway	125.20	0.0502	147.60	0.0426	65.00	0.0967
Heave	31.30	0.2007	20.50	0.3065	2.40	2.6180
Roll	31.15	0.2017	45.10	0.1393	3.68	1.7074
Pitch	31.14	0.2018	44.30	0.1418	3.68	1.7074
Yaw	8.22	0.7644	63.10	0.0996	14.80	0.4245

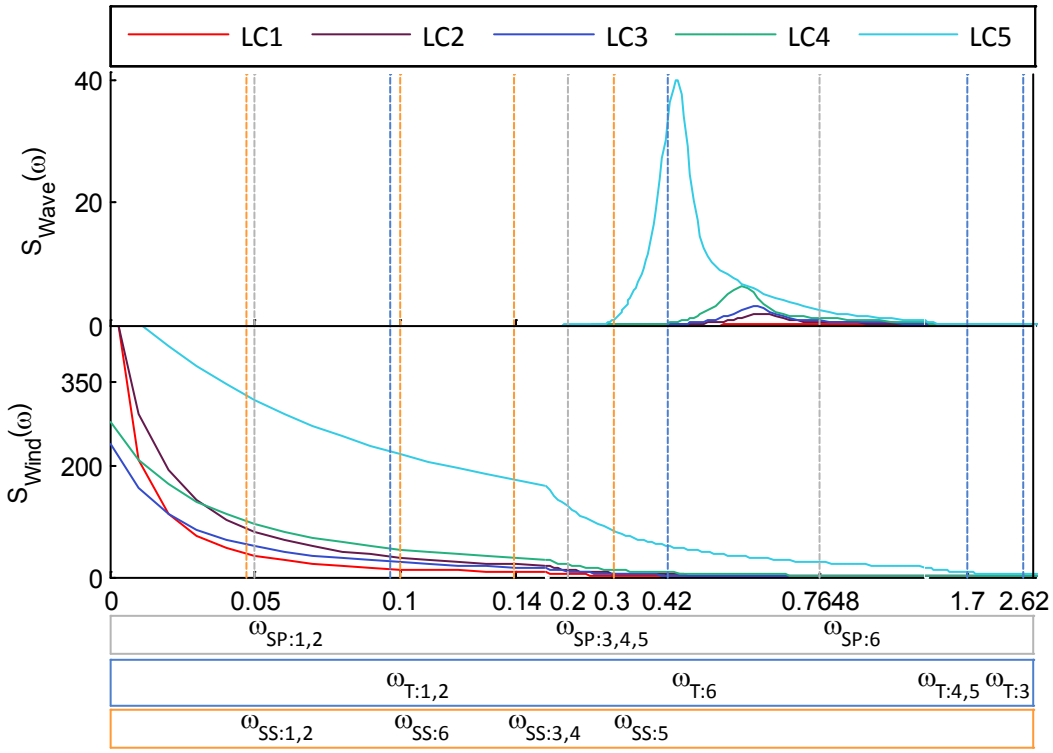

Figure 33 - Approx. locations of natural periods of the concepts. Sp: Spar, T: TLP, SS: Semi-Sub

8.3.1 Non-Directionality

8.3.1.1 Below Rated

Mean positions of surge and pitch for all the floaters follow the magnitude of the mean thrust force. SS has the largest surge mean values and the largest pitch mean values.

Below rated surge motion is mainly thrust induced, and all the floaters have maximum surge STD in LC2, when also thrust STD is at its maximum. Surge STD is largest for SP in all load cases.

Both SP and TLP have their COGs located a considerable distance from the origin (-77 m and -33 m, respectively). This means that the surge motions studied here will include a portion due to pitch, since we are studying motions at the origin. SP is more influenced by this than TLP, since the TLP has restricted pitch motions, and SP has the lowest COG. SS has its COG placed 3.73 m above SWL, so the pitch contribution at the origin is limited.

SS has a larger pitch STD than SP for LC1 and LC2. The pitch motion is here mainly thrust induced, and both floaters have natural frequencies that are excited by thrust. Figure 33 indicates that $\omega_{SS:5}$ is placed in a position where wind speed density is higher than for $\omega_{SP:5}$. This could be a contributor to the greater oscillatory motion of SS for these load cases. The TLP has its pitch natural frequency $\omega_{T:5}$ positioned at high frequencies, where both wind and waves have low spectral density. TLP pitch motions are for LC1 and LC2 mainly wave induced motions around the peak frequency of the wave spectrum, with some contribution around $\omega_{T:5}$ at 1.7 rad/s.

The statistics show that the floaters have limited heave motions. In LC1-LC2, SP has the largest heave STD, but this motion will be influenced by pitch which is large for SP. Heave for SS is influenced in the WF part and has limited pitch influences. SS also have heave plates at each column that provides damping. The TLP also has limited heave motions due to the large stiffness of the tethers. This result in $\omega_{T:3}$ being positioned at a HF of 2.6 rad/s, and the small motions we see in LC1-LC2 are mainly due to pitch displacements.

Sway and roll motions for both SS and TLP are near zero in LC1 and LC2. In the discussion of the results of SP it was pointed out that the gyro moment about the z-axis can produce yaw motion when both wind and wave are aligned. The wave and thrust forces may then contribute to motions in the two DOFs, sway and roll, since the floater has a non-zero yaw angle at a given time. We see this effect is present in the statistics and spectrums for SP. SS do also show small yaw and roll motions in

LC2. Even though the roll motion is small, it has frequencies around $\omega_{SS:6}$ (0.1 rad/s). The yaw gyro moment is, for the TLP, not strong enough to make the floater yaw, so this effect is not present in any of the cases with the rotor active.

SS and SP both utilize catenary mooring lines. These two concepts can hence be compared also on the behaviour of the mooring lines, while it is harder to make any comparisons with the TLP. Comparison plot with line #2 will be used here since this is the line that has the largest tensions.

SS has a lower mean tension in all the load cases compared to SP. As a general trend we see that the TLP and SS has increased STD with sea state severity and that SP follows the same pattern as it has for surge. SS has the larger STD in LC1-LC5 than SP. The large STD of SS leads to larger max tension than SP in LC5, even though SS has more than 2/3 lower mean tension than SP. Both SS and the TLP show some negative tension in LC5. Having negative tension (compression) for a TLP is considered dangerous since it may result in a line snapping when the tether goes back to a position where it again is tensioned. Compression for SS may be some error in the analysis and should be investigated further.

Nacelle accelerations could be a governing factor for the mechanical components of the wind turbine. It is therefore an interesting parameter to compare between the different concepts. It is the surge displacement of the hub that governs the acceleration, at least for the non-directional cases. Also the wave induced displacements of the nacelle can dominate for accelerations, compared to low frequent displacements. This is because the acceleration amplitude is proportional to the displacement frequency squared for harmonic motions ($\ddot{x} = -\omega^2 A_x \sin \omega t$). For LC1 the TLP has a quite large STD in nacelle acceleration compared to the others. This results in a maximum value of 1.26 m/s^2, and the TLP spectrum for this DOF shows that it is dominated by the WF part and a peak at $\omega_{T:5}$. SP and SS have a low STD in LC1, and the spectrums show that it is only the LF parts that contribute. The drop in acceleration STD for the TLP from LC1 to LC2 could be related to the WF part, which moves further away from $\omega_{T:5}$ in LC2 (change in wave peak period). Inspection of the spectrum values of the wave height at $\omega_{T:5}$ reveals that there was a decrease from LC1 to LC2 from 0.03 to 0.01. This may be the main contributor to a less pronounced resonance peak in pitch for the TLP in LC2, and lesser nacelle acceleration STD.

8.3.1.2 Rated and Above

The mean surge values for all the floaters are at their maximum for LC3 at rated speed. This is also when the thrust mean force is highest. SS has the highest means followed by SP and then the TLP.

There is a large difference in mean pitch value between SS and SP, with 10.8 degrees and 5.2 degrees, respectively. SS has in its original design an active ballast system, which could be used to reduce this mean pitch value, but this is not included here. The mean pitch value for the TLP is 0.18 degrees in LC3. Both mean surge and pitch are reduced from LC3 through LC5 when the mean thrust force also reduces.

All the STDs in surge are reduced from LC2 to LC3. In LC3 the wind speed spectrum shows that the density around the lower frequencies, including around the surge natural periods of the floaters, are lower due to reduced turbulence intensity. This is believed to be the main contribution to the reduction in surge STD from LC2 to LC3, even though the magnitude of the thrust force is increased. The sea state severity has increased, but for surge the increase in WF is limited for all the floaters. The change in pitch motion is different for the floaters from LC2 to LC3. SP and the TLP have increased pitch motion while SS decreases. As explained earlier for SP, this increase in pitch is due to the combined effect of resonant pitch motions and negative damping above rated. The decrease of STD in pitch for SS could be related to the same effect mentioned for the surge reduction. The pitch SS spectrum has lower density values below $\omega_{SS:5}$ than in LC2, but the peak at $\omega_{SS:5}$ has increased.TLP has increased pitch motion with sea state severity, which is obvious when looking at the spectral values for the different load cases in the WF part.

LC4 is characterized by increased sea state severity, increased spectral density in the wind speed, and lower thrust magnitudes around the mean relative velocity compared to LC3 (Figure 33 and Figure 11). Both surge and pitch oscillations decrease from LC3 for SP and SS. For the TLP also the surge decreases since this motion is mostly LF, while pitch motion increases since this motion is excited mostly around $\omega_{T:5}$ and the wave spectral peak. SP has here about 5 % larger STD in pitch than SS, but due to SS's large mean of 6.9 degrees, the maximum values of SP are only around 2/3 of SS's maximum values.

LC5 has the most severe sea state and the highest wind speeds. Since the rotor is shut off in this case, the wind force on the rotor is mainly a drag force, and the magnitudes are low. Waves are now the largest influence on surge and pitch motions for all the floaters, and the STDs for these DOFs increase for all floaters from LC4 to LC5. The TLP experiences its largest values in both surge and pitch in LC5.

The TLP heave motions above rated are still limited. The largest motions occur in LC5, when there are high wave amplitudes and high peak period. The maximum heave amplitude for LC5 is about 10 times larger than the maximum of LC4. SS also gets larger heave motions with increased sea state severity, and maximum heave amplitude of 4 m for LC5.

From LC2 to LC5 all floaters experience an increase in nacelle acceleration with increased sea state severity. SS has the lowest STD and max values for the above rated cases, as well as below rated. SP and TLP show similar STD values for LC2-LC4. Even though the STDs of SP and TLP are very close in LC4, we see a large difference in max and min acceleration with SP experiencing the largest values. The max and min values here may not be completely reliable since they are based on one seed, and the differences in max and min might be reduced if we were to run several seeds (which is the case for SP).

Even though the differences in statistics of the accelerations are not so large for SP and TLP, the governing frequency of the accelerations are. Performing a zero crossing analysis of the hub acceleration time series showed that the TLP hub acceleration changes signs the most over a 1 hour simulation period.

Table 19 - Number of hub acceleration direction changes per minute

	LC1	LC2	LC3	LC4	LC5
Spar	22	14	13	14	11
Semi-Sub	24	17	18	17	17
TLP	31	33	32	32	32

As Table 19 shows, the changes from load case to load case are quite small, except for SP and SS from LC1 to LC2. For a given load case the TLP has over twice the amount of changes in acceleration. These changes in acceleration will contribute to the fatigue of the turbine components, and during its lifetime the number of cycles for the TLP will be near twice that of SP.

8.3.2 Directionality

The mean surge and pitch positions do not change significantly with increasing directionality for LC3 and LC4. Some lower means are visible in the 90 degree cases in LC5 for all the floaters.

The trend of pitch STD with increasing load case is unchanged, except for LC90-5, where the pitch motions are lower for all the floaters. In LC3 there are no large changes in STD with increasing degree, except some for the TLP. The TLP seems to be the one that changes the most with directionality in a given load scenario. The change from LC5 to LC90-5 is largest for the TLP, followed

by SS. This indicates that SP is least influenced by waves and more influenced by thrust force than the other concepts.

The surge trend is the same as for pitch. The largest changes with directionality occur for LC5. STD of all the floaters then decreases by a large factor in the 90 degree case compared to the 0 degree case. For SP and TLP the changes are likely to be connected to the effect of waves working in the y -direction and not exciting surge motion, combined with the decreased pitch motions.

The TLP and SS have increased roll STD with increasing sea state severity and increasing directionality. This is not true for SP. SP does show an increase in STD with increasing degree, but roll motions drop from a peak value in LC30/90-3 to a lower value in LC30/90-4 while they increase for LC30/90-5. In all the directional cases of LC5, SS has larger roll motions than SP.

The sway comparison plot shows that the different floaters have comparable sway STDs. For LC3, SP have the largest sway motions in all the directional cases. However, as also the statistics show, roll STD is large and this will affect sway at the origin for SP. The same trend continues for LC4 and LC5, and SP has visibly larger sway motion, especially in LC90-5.

The main observations for the yaw motions of the floaters are that they increase with increased directionality, and that for the TLP and SS, they also increase with increased sea state severity, while this is not the case for SP. The reasons for the large yaw motions of SP have been described earlier. The same severity of motion is not visible for the other floaters. None of these two floaters have the yaw natural period in the WF part, where the roll motions are large in the offset cases. This limits the yaw responses. Additionally SS have large potential damping in yaw due to its asymmetrical shape and the TLP has limited roll motions so the yaw moment from the thrust is small.

In terms of power production and looking at all the load cases run there is not many big differences. If we were to point on some differences it would be for LC3 were the mean power production for the TLP, SP and SS in kW were, 4569, 4554 and 4478 respectively. The difference between the TLP and SP amount to about 2 % of the turbine rated power.

9 Conclusions

Load and response analysis:

- In the operational conditions studied, the floater surge and pitch motions are dominated by wind- and not wave loads.
- Surge STD is largely influenced by how turbulent the wind is below rated.
- Pitch motions are large both at and above rated, and the use of notch filter is an effective way to reduce these pitch motions.
- The floater experiences limited heave motions in all the load cases.
- Situations where wind and wave have different angle of attack may cause unwanted yaw motions due to several coupled effects. The yaw induced moment from thrust when the floater rolls is of greatest concern.
- The mooring lines are mostly influenced by surge motion in the LF part, except for the extreme sea state when the wind turbine is not operating. In that case the WF part dominates.
- In operational conditions the largest mooring line tension is found in LC3, where the thrust mean value is at its largest. The largest STD of mooring line tension is found in LC2, when surge STD is large. Both the STD and max value of tension in LC5 are large and mainly wave induced.

Stochastic variation:

- 5 and 7 seeds for the mean values in LC3 and LC4, respectively, give convergence to 3 significant digits for most DOFs.
- LC4 needs a larger number of simulations to obtain stable STD's for the different DOFs compared to LC3. More than 10 seeds are needed to obtain great accuracy in STD for pitch.
- 10 or more seeds are needed for great accuracy in max and min values for the 6 body DOFs in both LC3 and LC4.
- The rigid body motions of the floater do not fit a Gaussian distribution.

Depth change:

- Changing the depth from 320 m to 160 m was found feasible with only minor changes to the mooring line system.

Conclusions comparison part:

I will here sum up some key points from the discussion that could result in negative or positive attributes for the different floaters. For each point I will also present an explanation for why the behaviour is wanted/unwanted.

- SP has the largest surge oscillations, but the max surge values of SS and SP are close due to the large mean of SS. If the floater has large horizontal motions the spacing between wind turbines would have to be greater in a wind farm.

- Below rated, SS has the largest pitch STD's and mean positions. Large motions in mild load cases could lead to difficulties in boarding and performing maintenance on the wind turbine.

- SP has large yaw motions in many load cases. The overall effect of this is uncertain, but excessive motions are unwanted.

- The TLP has a large STD in tension for all cases, which may lead to excessive fatigue contribution. SP has for all cases the lowest STD and the lowest max tension for most cases.

- The negative tensions in some cases for the TLP could be dangerous for the integrity of the floater.

- The pitch natural frequency of the TLP is located at a high frequency. This may lead to relatively high acceleration, STD and maximum, even at mild sea states when the peak period of waves are low.

- SS has the lowest STDs and max values in acceleration for all load cases. The TLP has the largest STD for most cases, while SP has the largest max values for the two most severe load cases. Large accelerations at the hub will give inertia loading on the wind turbine.

- The governing frequency of acceleration is highest for the TLP, which may contribute to reduction of the lifetime of the wind turbine.

- At rated wind speed the TLP has the largest mean power production, followed by SP and then SS.

- All floaters have been subjected to lower water depths, 160 m for SP, 120 m for TLP and 80 m for SS and found feasible. SS has an advantage here, since it may be placed at lower water depths than SS and TLP due to its low draft.

As a final presentation of the comparison a summary table with some of the discussed points has been made. It is hard to quantify which one performs the best in the different categories, since there does not exist or has been found benchmark values for the different categories. The table is hence open for discussion in some cases. + is positive, - negative and 0 represent neutral.

Table 20 - Summary of comparison

	SP	SS	TLP
Minimum distance between turbines in wind parks	-	-	+
Motions below rated, w.r.t. maintenance etc.	0	-	-
Excessive yaw motions	-	+	+
Negative tension	0	-	-
Mooring line fatigue	+	-	-
Acceleration	0	+	-
Frequency of acceleration	+	+	-
Water depth	-	-	+

9.1 Further work

- Further studies on the asymmetric properties of the mooring system should be done to evaluate the effect of on the floater motions, especially for yaw.
- Further studies of the effect of yaw stiffness on the floater, and the influence of the thrust induced moment dependency on relative velocity should be carried out.
- Establish a mooring line model that explicitly includes the delta lines, and investigate if this will reduce the yaw motions.
- Include a flexible tower and the dynamics of the wind turbine control system in the time domain simulations.
- Study economical aspects of the different floaters, since this will be a governing parameter for investment decisions regarding offshore wind turbines.
- Changing the depth from 320 m to 160 m was found feasible. Due to the assumption on the mooring line properties, a similar type of study should be carried out with the use of mooring lines available on the market.
- Collect key data that defines important parameters as e.g. max acceleration allowed for wind turbines, and max relative motion between vessel and turbine allowed for maintenance etc. This could lead to more relevant conclusions, not only on their performance relative to each other, but also on the feasibility of a concept.

10 References

1. **Jonkman, J.** *Definition of the Floating System for Phase IV of OC3.* s.l. : NREL, 2010.

2. *Engineering Challenges for Floating Offshore Wind Turbines.* **Sclavounos, P., Butterfield, S., Musial, W. and Jonkman, J.** s.l. : National Renewable Energy Laboratory and Massachusetts Institute of Technology, 2005.

3. **Jonkman, J. , Butterfield, S., Musial, W. and Scott, G.** *Definition of a 5-MW Reference Wind Turbine for Offshore System Development.* s.l. : NREL, 2009.

4. **Gao, Z.** *Tower model.* 2010.

5. **Jonkman, J.M.** *Dynamics Modeling and Loads Analysis of an Offshore Floating Wind Turbine.* s.l. : NREL, 2007.

6. **Faltinsen, O.M.** *Sea loads on ships and offshore structures.* s.l. : Cambridge University Press, 1990.

7. **Hansen, Martin O. L.** *Aerodynamics of Wind Turbines.* s.l. : Earthscan. 978-1-84407-438-9.

8. **Barr, Alan H.** Caltech. [Internett] [Sitert: 26 May 2011.] http://www.cs.caltech.edu/~cs20/c/esn.pdf.

9. **Marintek.** *SIMO - Theory Manual Version 3.6, rev: 2.* 2009.

10. **(DNV), Det Norske Veritas.** *RP-C205, ENVIRONMENTAL CONDITIONS AND ENVIRONMENTAL LOADS.*

11. **Tipler, Paul A. og Mosca, Gene.** *Physics for scientists and engineers.* 2004. 0-7167-4389-2.

12. **Marintek.** *RIFLEX Theory Manual.* 2008.

13. **(DNV), Det Norske Veritas.** *OS-E301, POSITION MOORING.* 2010.

14. **Pettersen, Bjørnar.** *Marin teknikk 3 - Hydrodynamikk.* s.l. : Institute of marine technology, NTNU, 2007.

15. **Moriarty, P.J. og Hansen, A.C.** *AeroDyn Theory Manual.* s.l. : National Renewable Energy Laboratory, 2005.

16. **DNV.** *DNV-OS-J101 - Design of offshore wind turbine structures.* s.l. : DNV, 2010.

17. **Skaare, Bjørn, Hanson, Tor David og Knauer, Andreas.** *Offshore Wind Turbine Loads in Deep-water Environment.* s.l. : Ewec proceedings?, 2006.

18. **Bewley, Thomas R.** *Numerical Renaissance: Simulation, Optimization and Control.* 2009.

19. **Balchen, Jens G., Andresen, Trond og Foss, Bjarne A.** *Reguleringsteknikk.* s.l. : Institutt for teknisk kybernetikk, NTNU, 2004. 82-471-5147-2.

20. **DNV.** *Sesam HydroD - Theory manual.* 2008.

21. **Software, DNV.** *Wadam User manual.* 2005.

22. **Gao, Z.** *Logaritmic decrement.* 2010.

23. **Matha, D.** *Model Development and Loads Analysis of an Offshore Wind Turbine on a Tension Leg Platform, with a Comparison to Other Floating Turbine Concepts.* s.l. : University of Colorado, 2010.

24. **Johannessen, Kenneth, Stokka, Meling T og Haver, Sverre.** *Joint distribution for wind and waves in the Northern North Sea.* Stavanger : The International Society of Offshore and Polar Engineers, 2001. 1-880653-51-6.

25. Wikipedia. [Internett] [Sitert: 11 June 2011.] http://en.wikipedia.org/wiki/Moving_average.

26. **George W. Collins, II.** *Fundamental Numerical Methods and Data Analysis.* 2003.

27. **Greco, Marilena.** Lectures notes on Sea Loads, NTNU. Trondheim : s.n., 2010.

28. **Libbrecht G, Kenneth.** Measurements and Significant Figures. [Internett] [Sitert: 11 June 2011.] http://www.ligo.caltech.edu/~vsanni/ph3/SignificantFiguresAndMeasurements/SignificantFiguresAndMeasurements.pdf.

29. **Lygren, Jon Erik L.** *Dynamic response analysis of a TLP floating .* Trondheim : NTNU, 2011.

30. **Chenyu, Luan.** *Dynamic response analysis of a Semi-Submersible floating wind turbine.* Trondheim : NTNU, 2011.

31. **Ormberg, Harald, Passano, Elizabeth og Luxcey, Neil.** *Global analysisof a floating wind turbine using an aero-hydro-elastic model.* s.l. : MARINTEK, 2010.

32. **Matha, D.** *Model Development and Loads Analysis of an Offshore Wind Turbine on a Tension Leg Platform, with a Comparison to Other Floating Turbine Concepts.*

33. *A generic 5 MW Windfloat for numerical tool validation & comparison against a generic Spar.* **Roddier, Dominique, et al.** Rotterdam : OMAE, 2011.

11 Appendix

APPENDIX 1

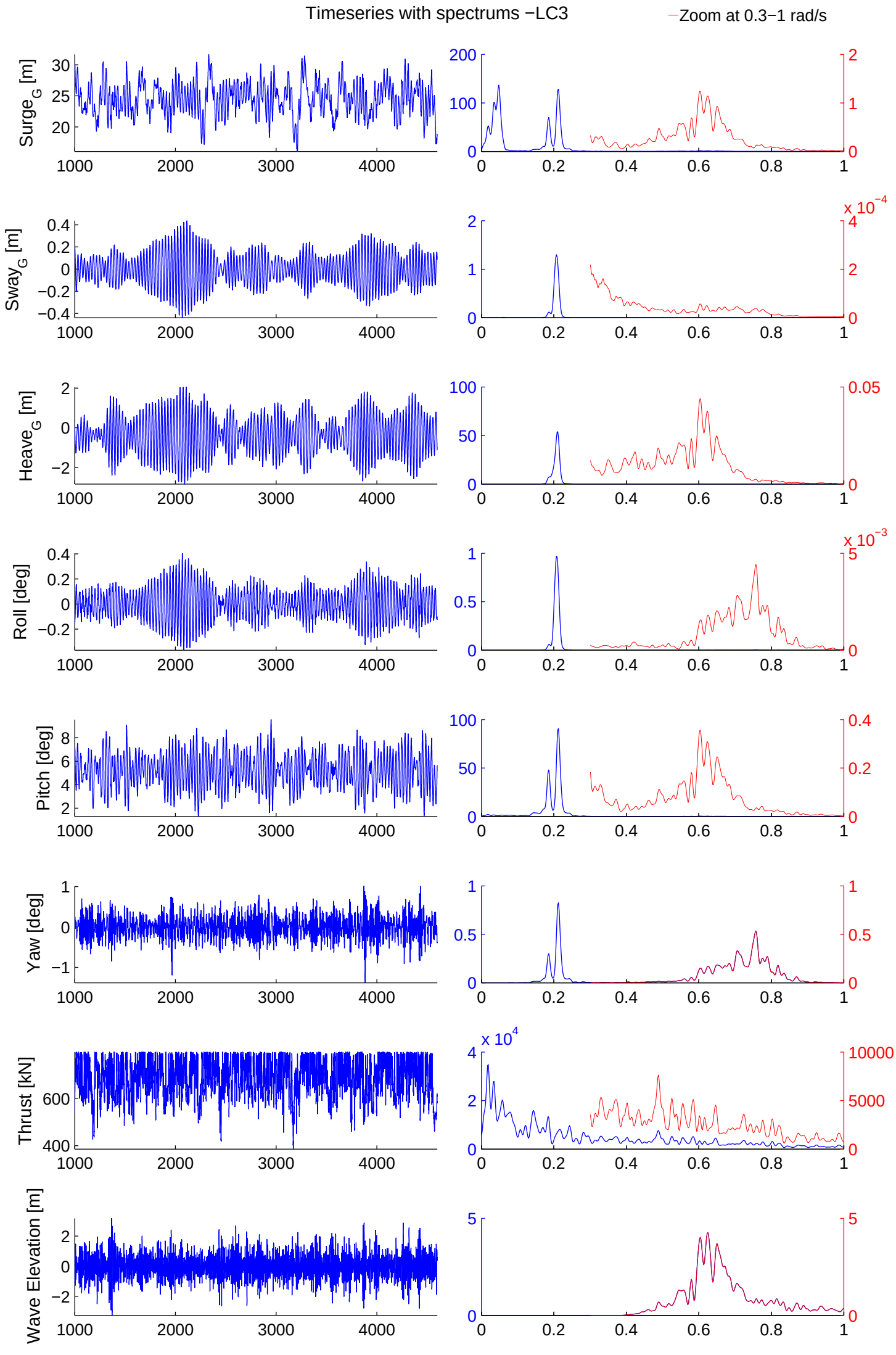
Timeseries with spectrums −LC3
Zoom at 0.3−1 rad/s
Surge_G [m]
Sway_G [m]
Heave_G [m]
Roll [deg]
Pitch [deg]
Yaw [deg]
Thrust [kN]
Wave Elevation [m]
x 10^-4
x 10^-3
x 10^4

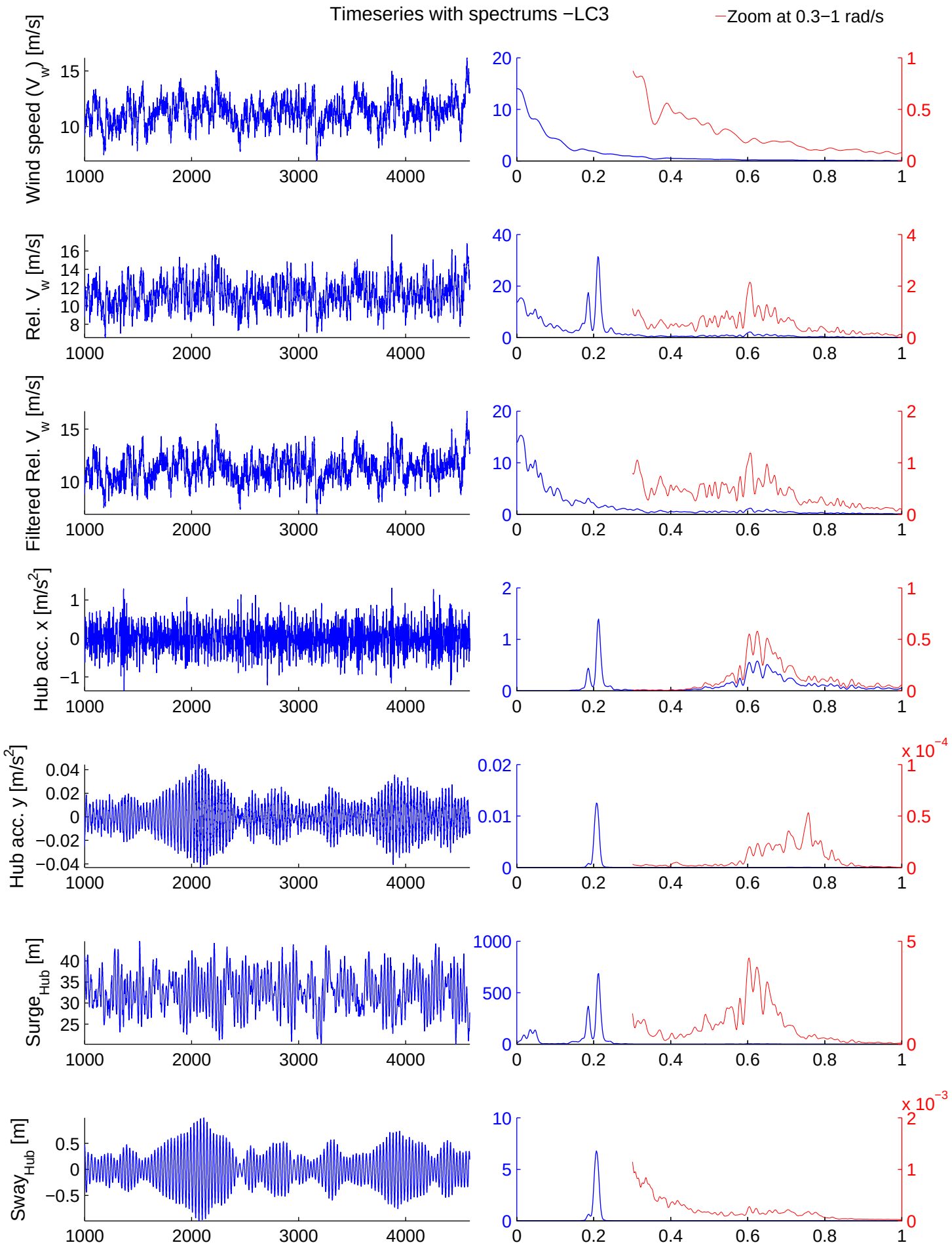
Timeseries with spectrums −LC3
Zoom at 0.3−1 rad/s
Wind speed (V_w) [m/s]
Rel. V_w [m/s]
Filtered Rel. V_w [m/s]
Hub acc. x [m/s^2]
Hub acc. y [m/s^2]
Surge_Hub [m]
Sway_Hub [m]
x 10^-4
x 10^-3

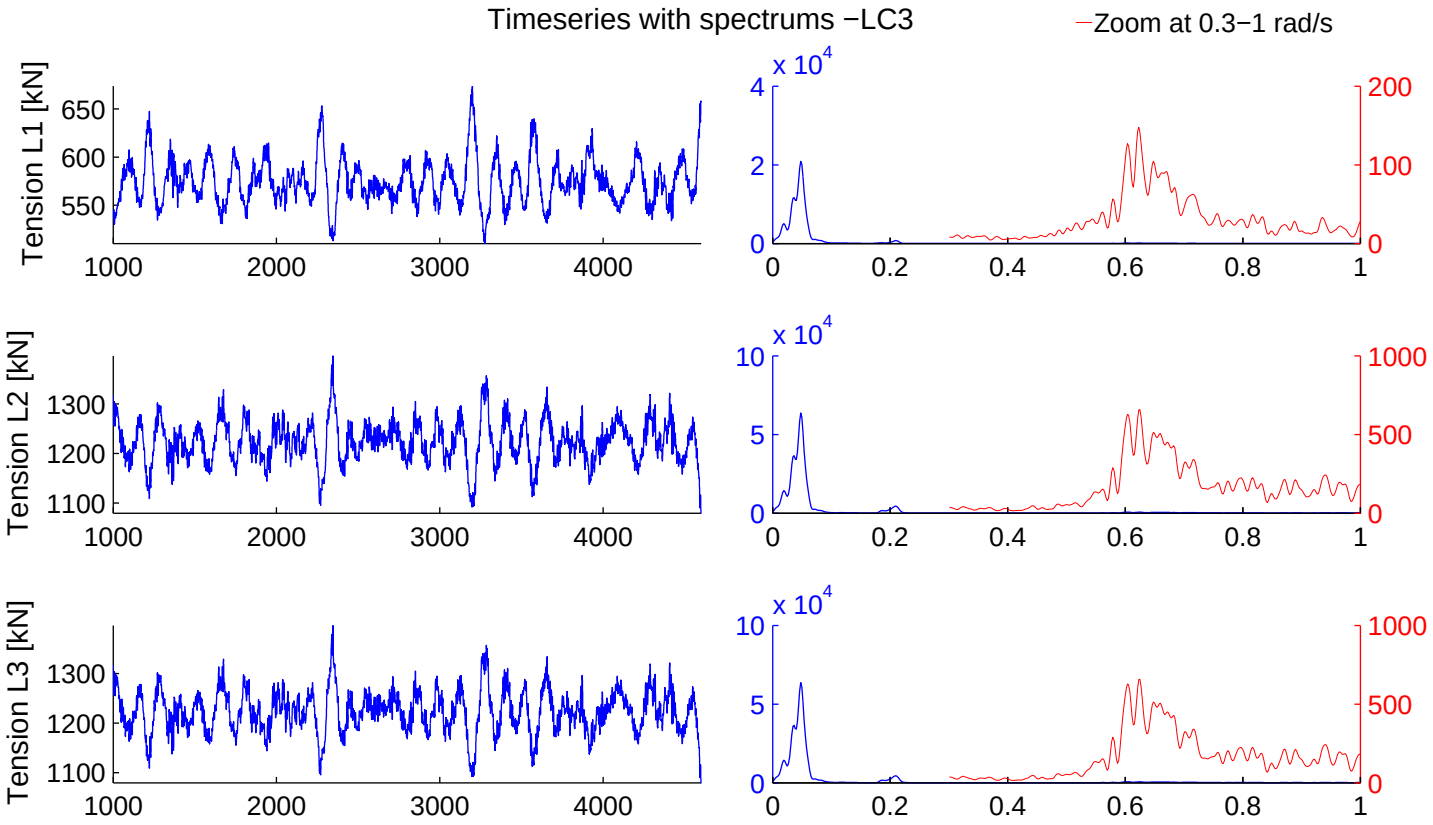
Timeseries with spectrums −LC3
Zoom at 0.3−1 rad/s
Tension L1 [kN]
Tension L2 [kN]
Tension L3 [kN]
x 10^4

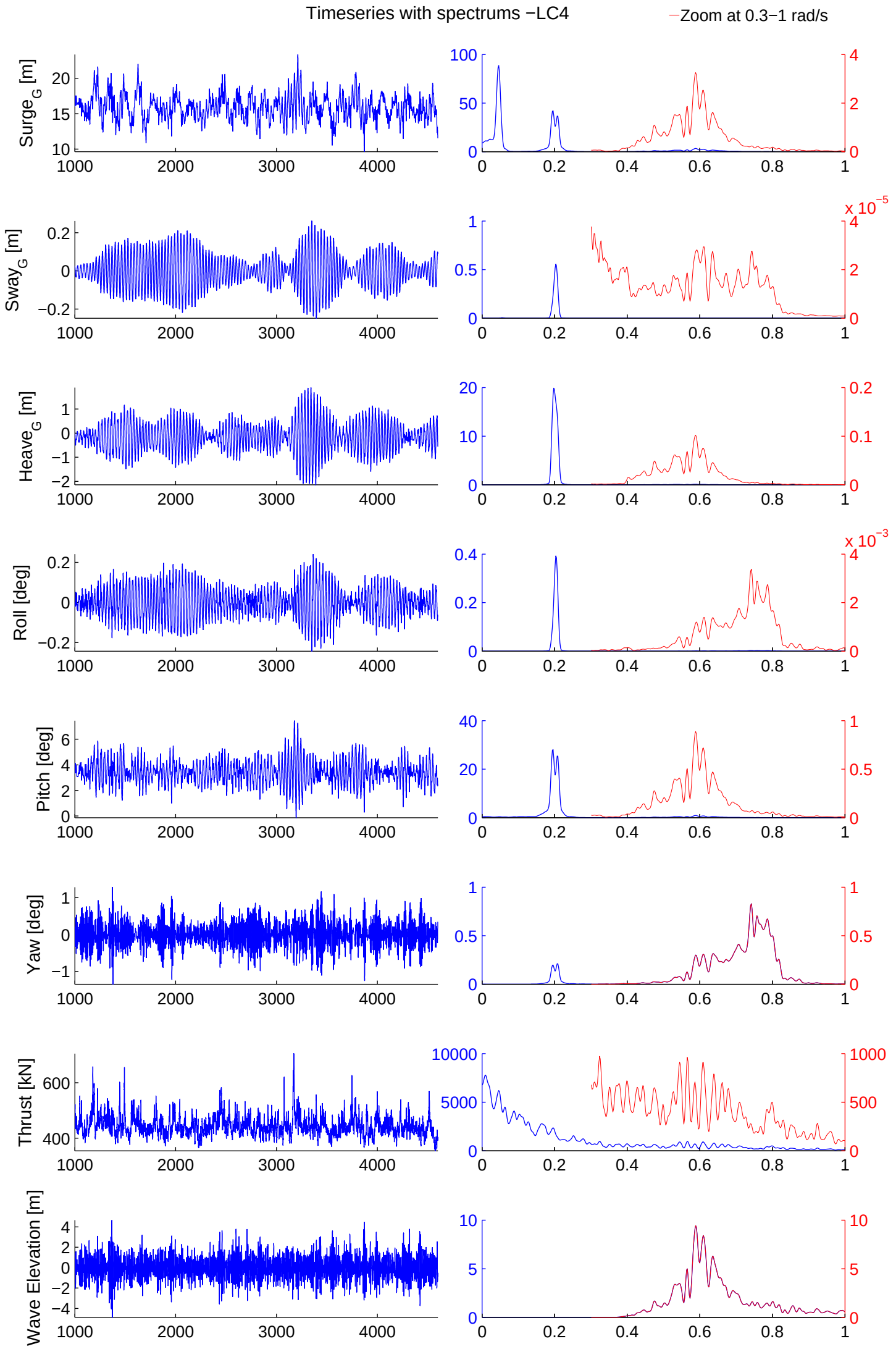
Timeseries with spectrums −LC4
Zoom at 0.3−1 rad/s
Surge_G [m]
Sway_G [m]
Heave_G [m]
Roll [deg]
Pitch [deg]
Yaw [deg]
Thrust [kN]
Wave Elevation [m]
x 10^-5
x 10^-3

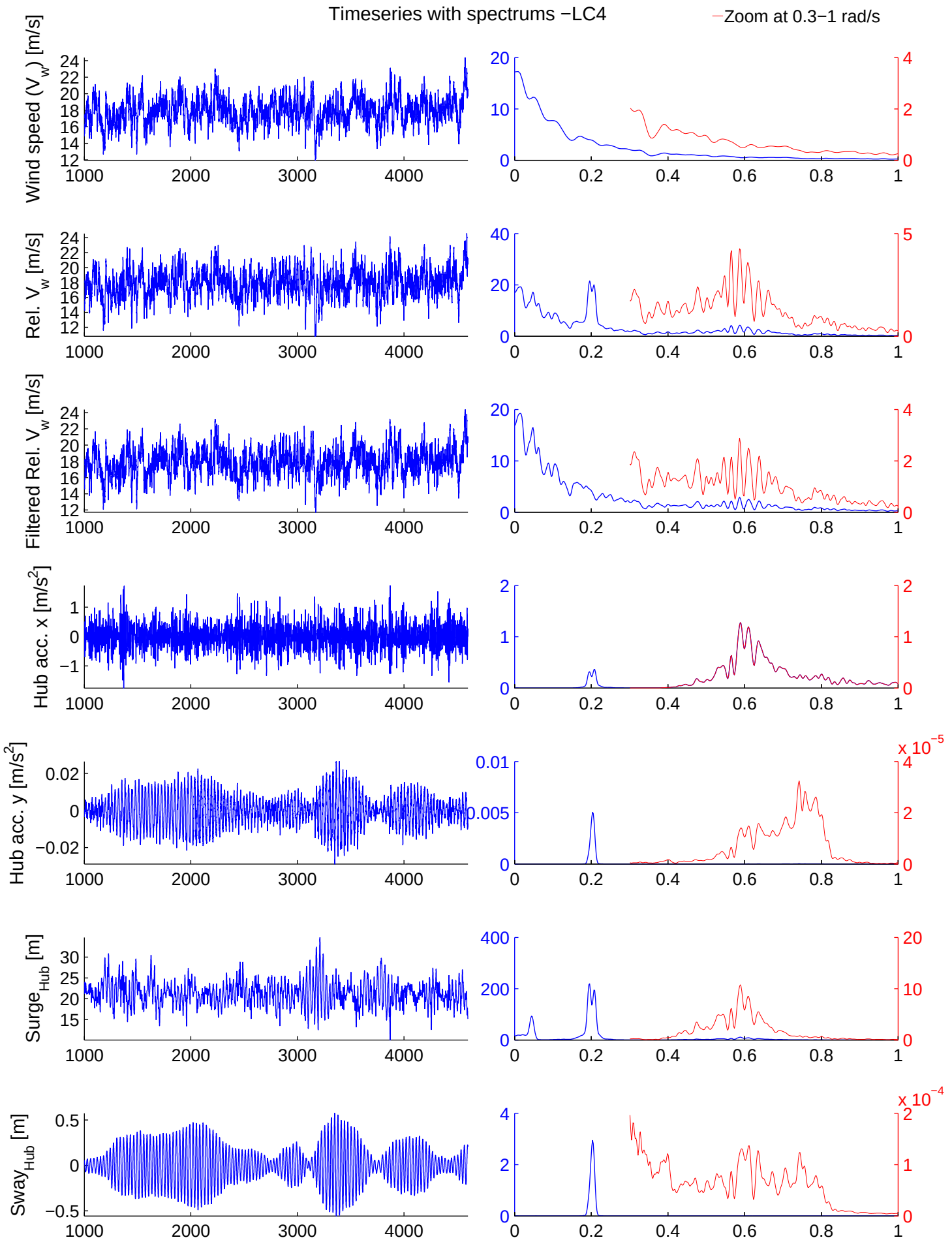
Timeseries with spectrums −LC4
Zoom at 0.3−1 rad/s
Wind speed (V_w) [m/s]
Rel. V_w [m/s]
Filtered Rel. V_w [m/s]
Hub acc. x [m/s^2]
Hub acc. y [m/s^2]
Surge_Hub [m]
Sway_Hub [m]
x 10^-5
x 10^-4

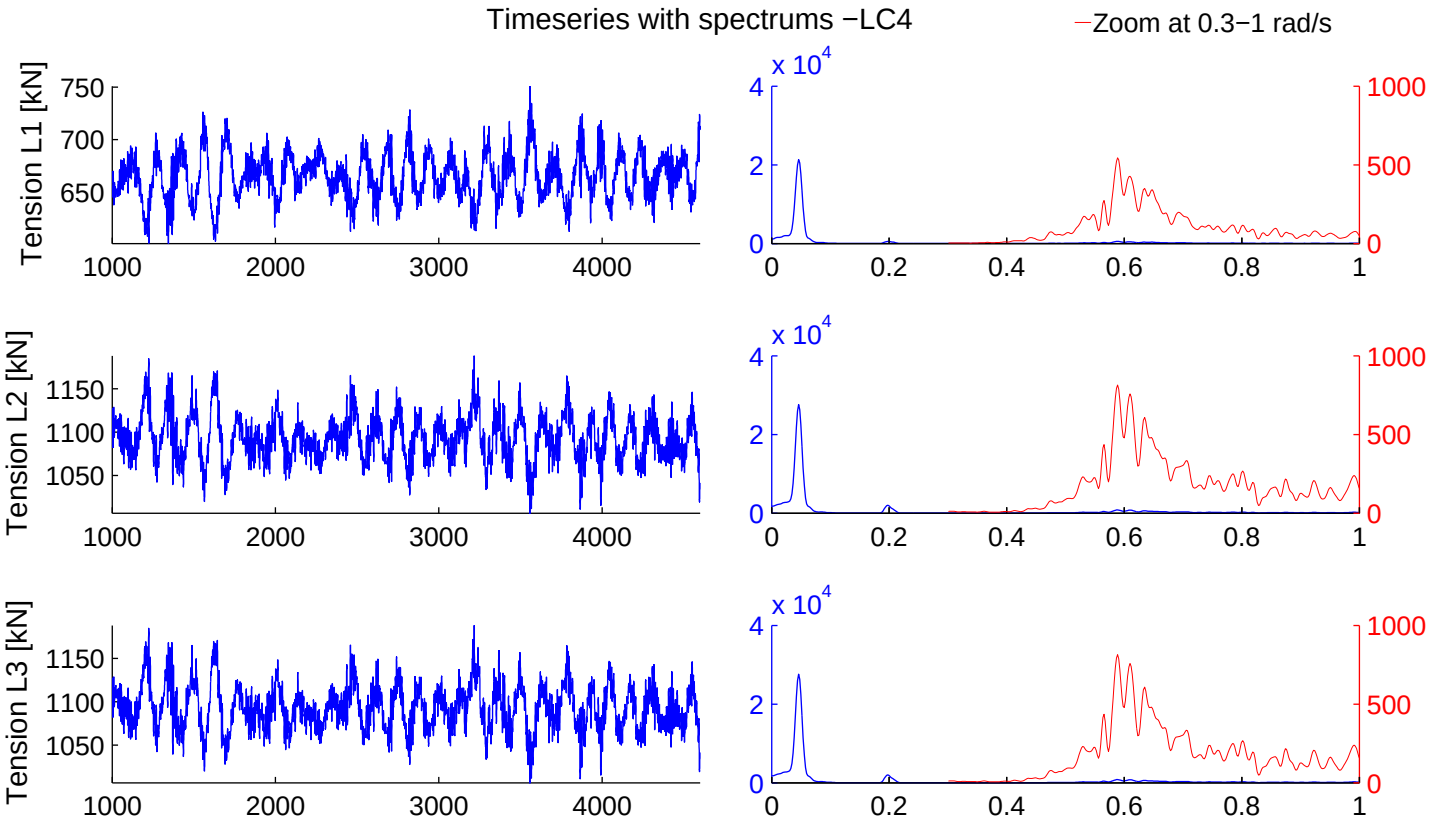
Timeseries with spectrums −LC4
Zoom at 0.3−1 rad/s
Tension L1 [kN]
Tension L2 [kN]
Tension L3 [kN]
x 10^4

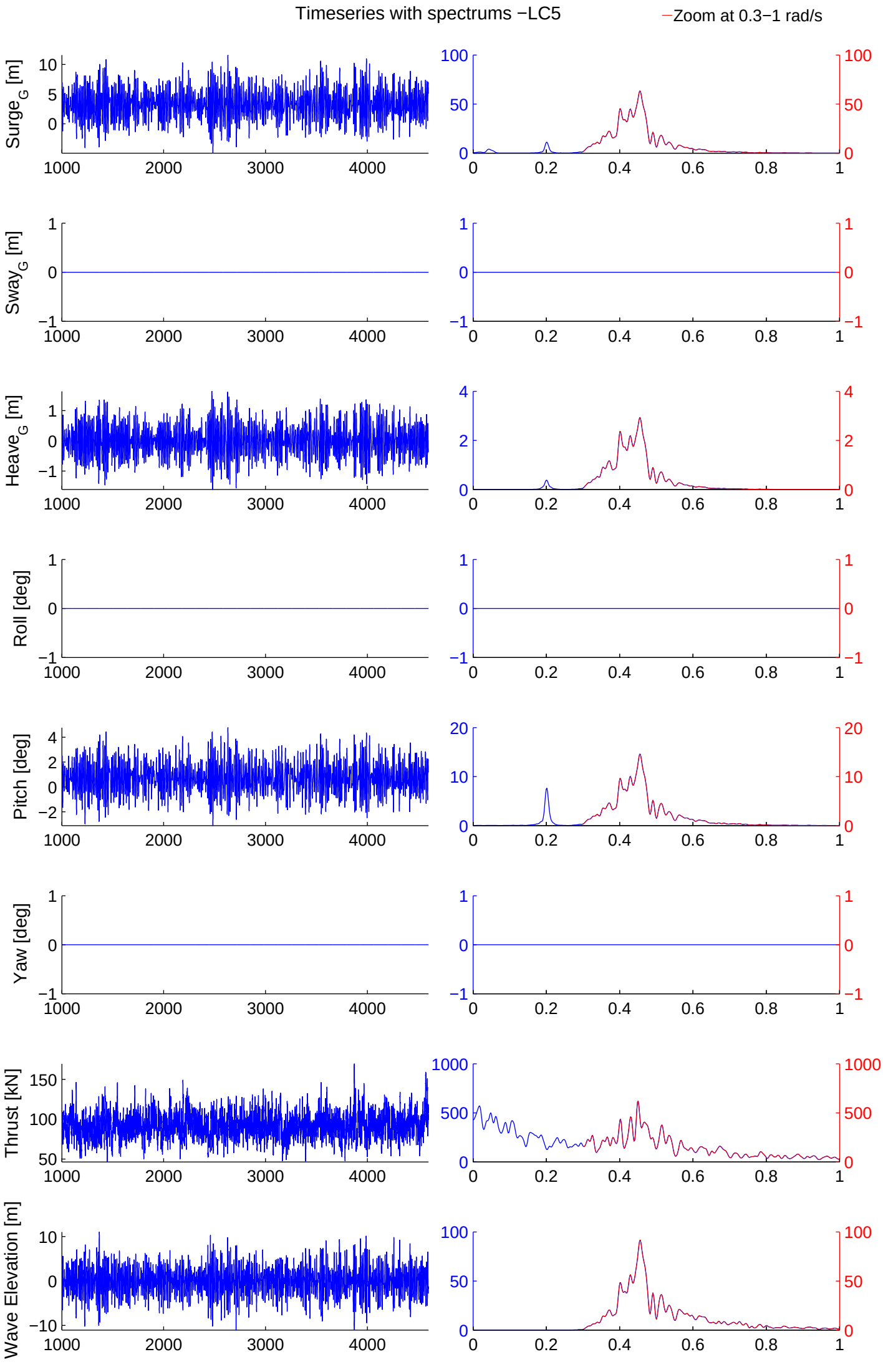
Timeseries with spectrums −LC5
Zoom at 0.3−1 rad/s
Surge_G [m]
Sway_G [m]
Heave_G [m]
Roll [deg]
Pitch [deg]
Yaw [deg]
Thrust [kN]
Wave Elevation [m]

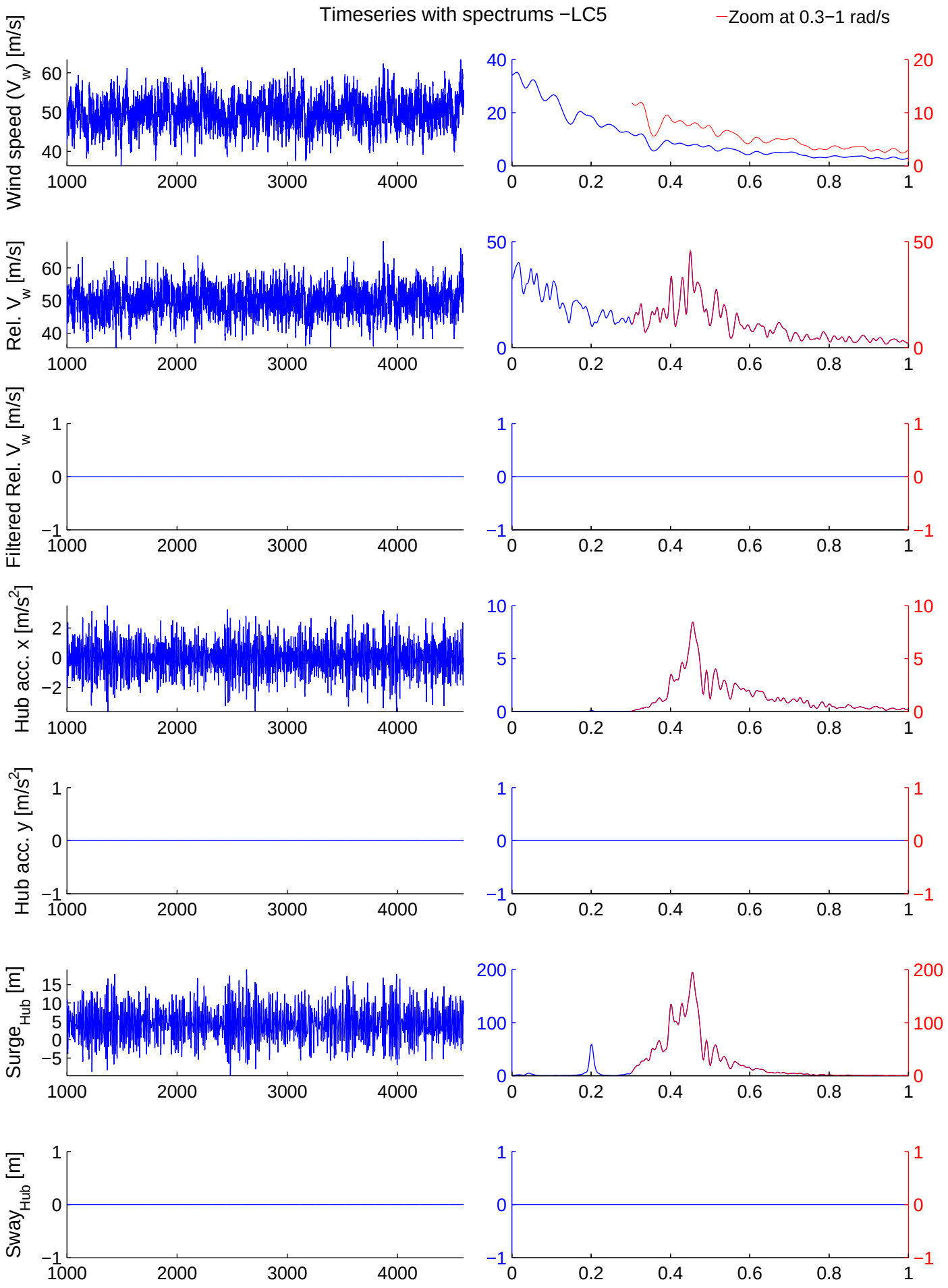
Timeseries with spectrums −LC5
Zoom at 0.3−1 rad/s
Wind speed (V_w) [m/s]
Rel. V_w [m/s]
Filtered Rel. V_w [m/s]
Hub acc. x [m/s^2]
Hub acc. y [m/s^2]
Surge$_{Hub}$ [m]
Sway$_{Hub}$ [m]

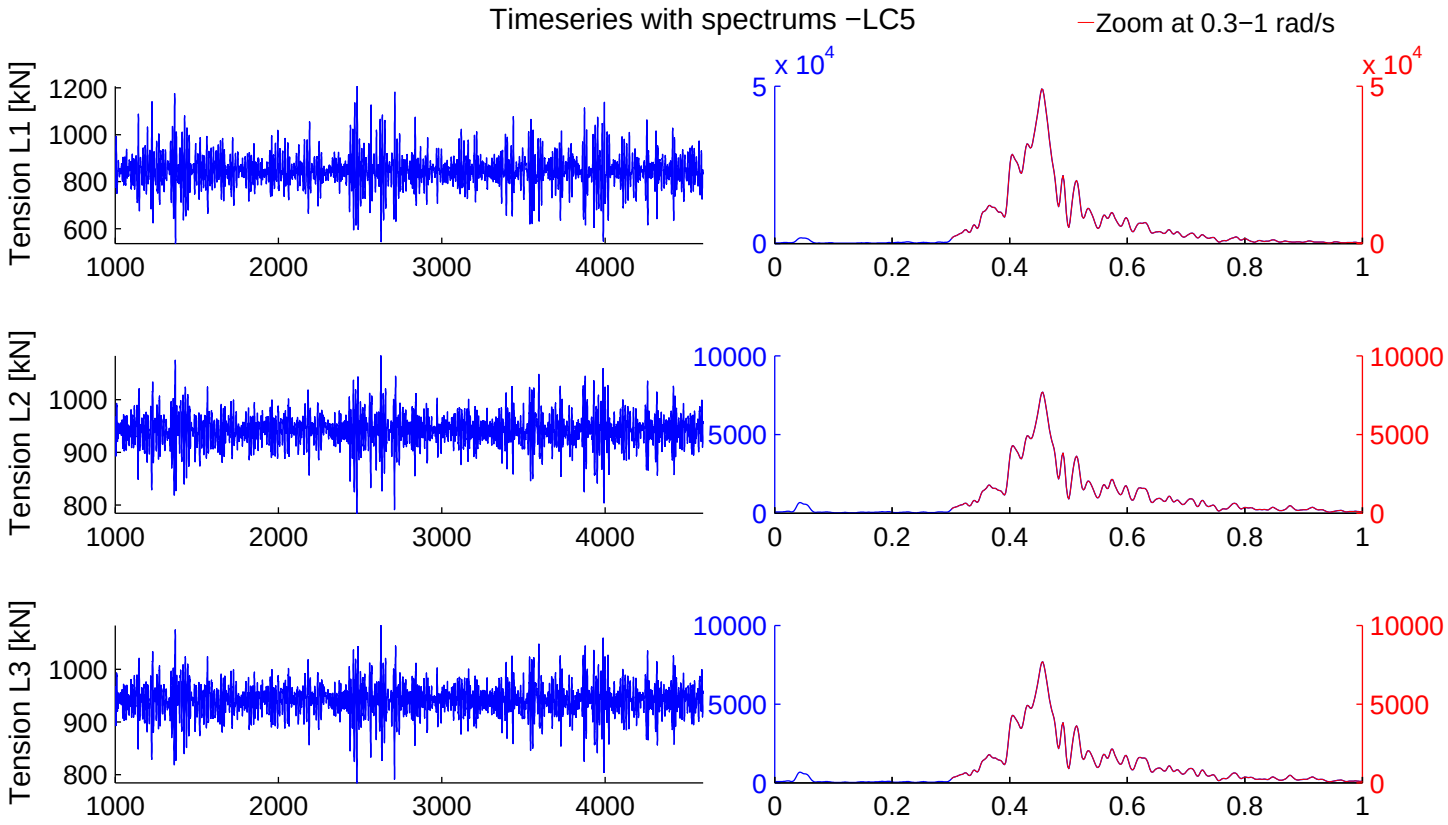
Timeseries with spectrums −LC5
Zoom at 0.3−1 rad/s
Tension L1 [kN]
Tension L2 [kN]
Tension L3 [kN]
x 10^4
1200
1000
800
600
1000
900
800
5
0
10000
5000
0
1000
2000
3000
4000
0.2
0.4
0.6
0.8
1

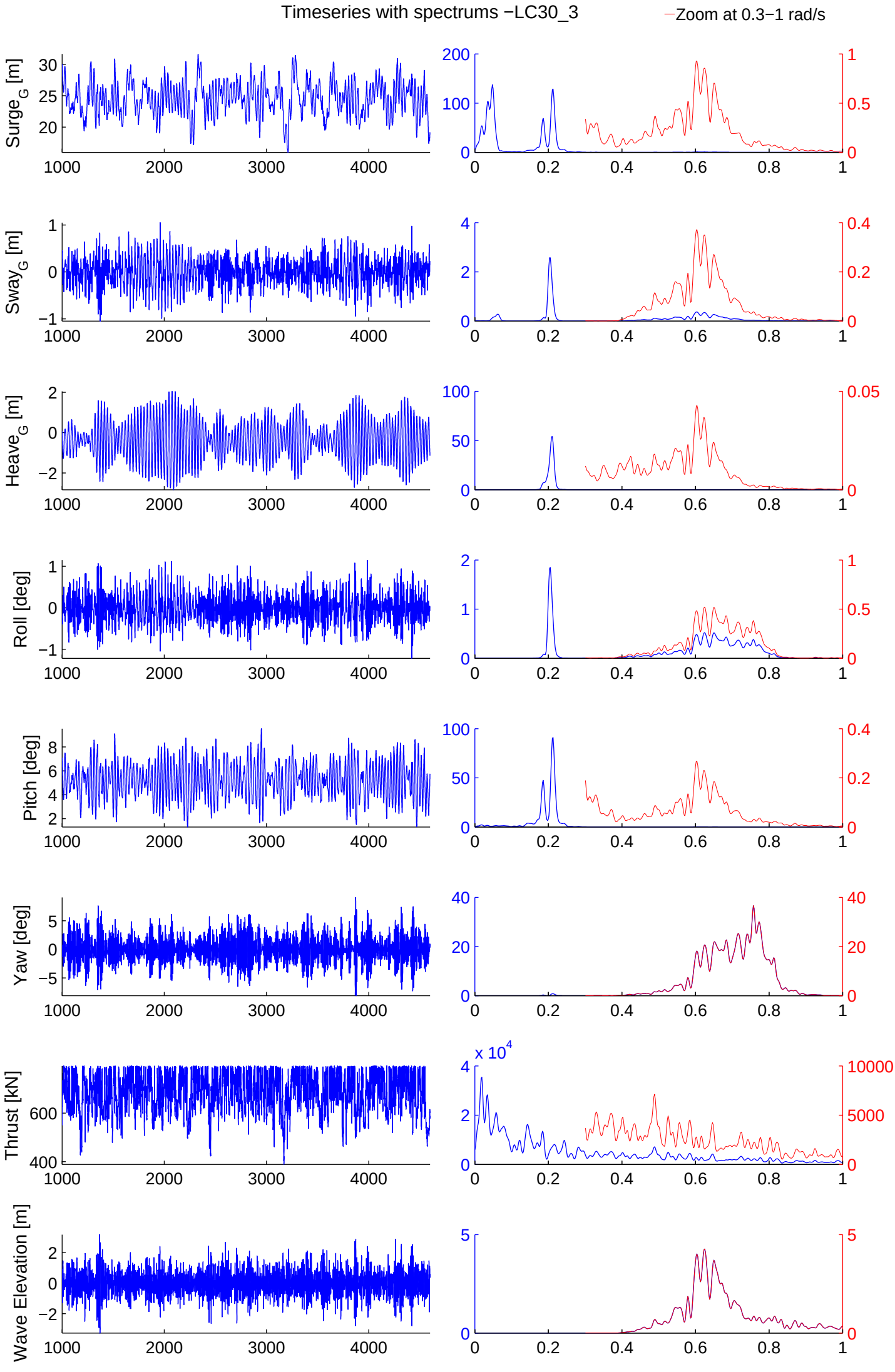
Timeseries with spectrums −LC30_3
Zoom at 0.3−1 rad/s
Surge_G [m]
Sway_G [m]
Heave_G [m]
Roll [deg]
Pitch [deg]
Yaw [deg]
Thrust [kN]
Wave Elevation [m]
x 10^4

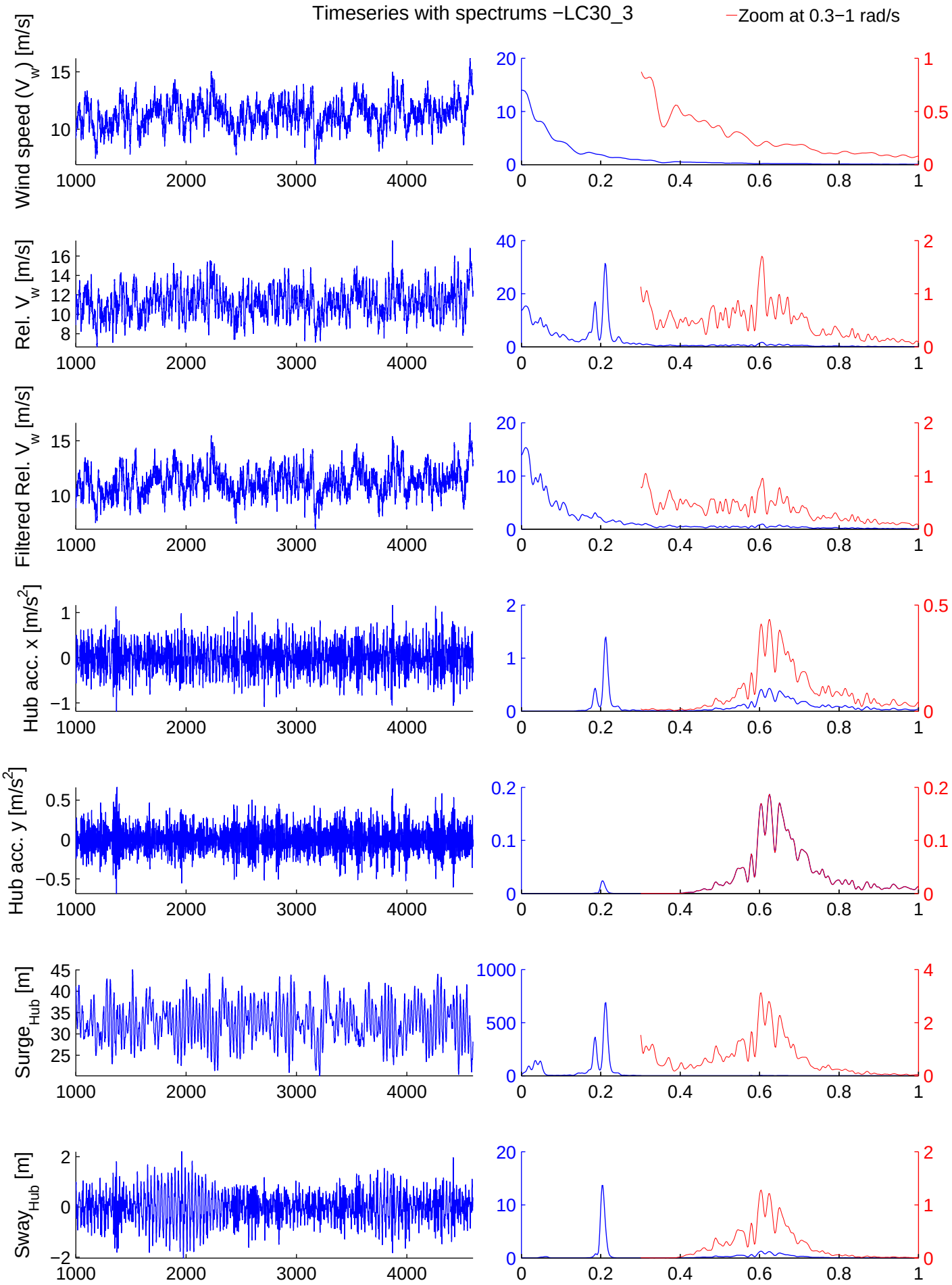
Timeseries with spectrums −LC30_3
Zoom at 0.3−1 rad/s
Wind speed (V_w) [m/s]
Rel. V_w [m/s]
Filtered Rel. V_w [m/s]
Hub acc. x [m/s^2]
Hub acc. y [m/s^2]
Surge_Hub [m]
Sway_Hub [m]

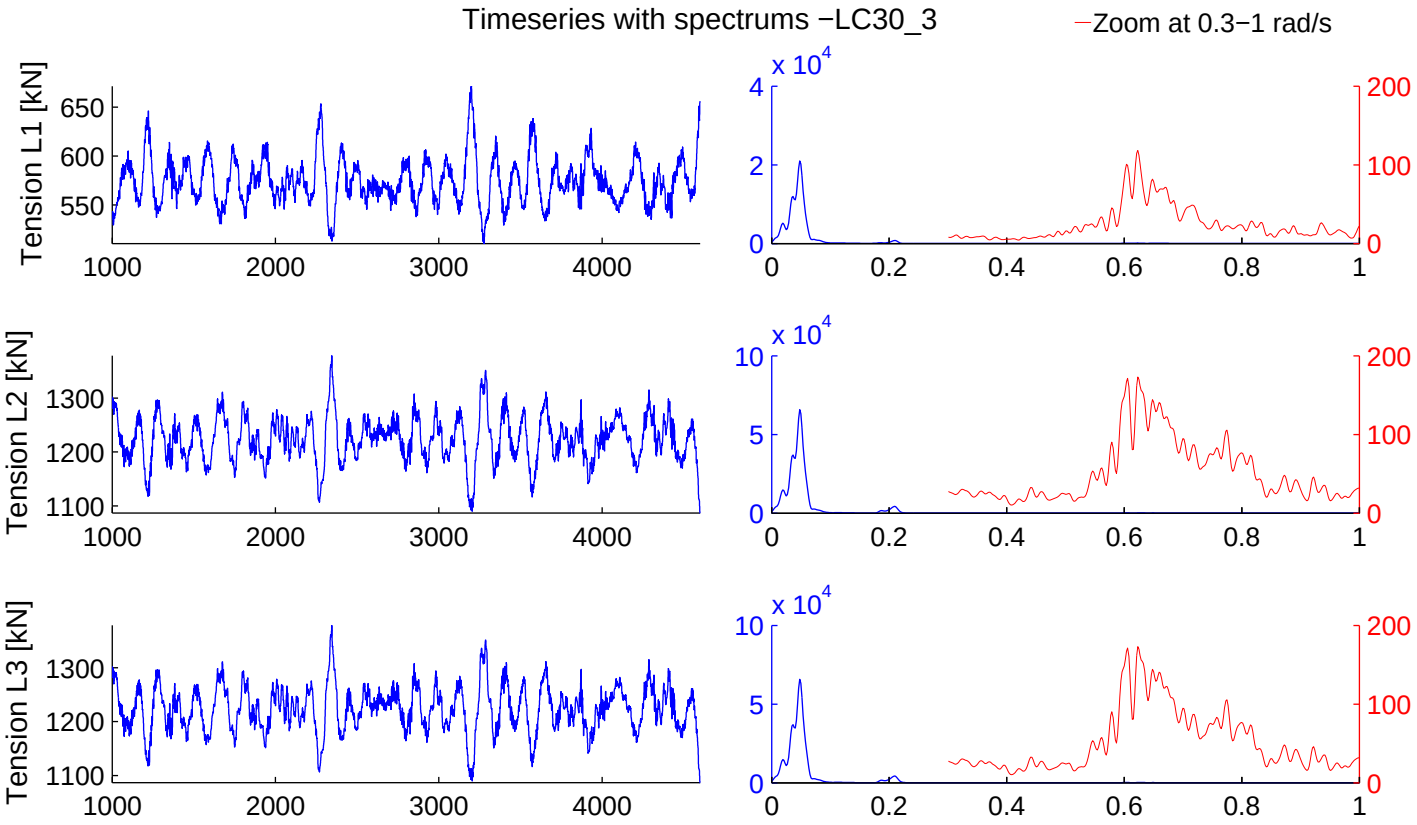
Timeseries with spectrums −LC30_3
Zoom at 0.3−1 rad/s
Tension L1 [kN]
Tension L2 [kN]
Tension L3 [kN]
x 10^4

APPENDIX 2

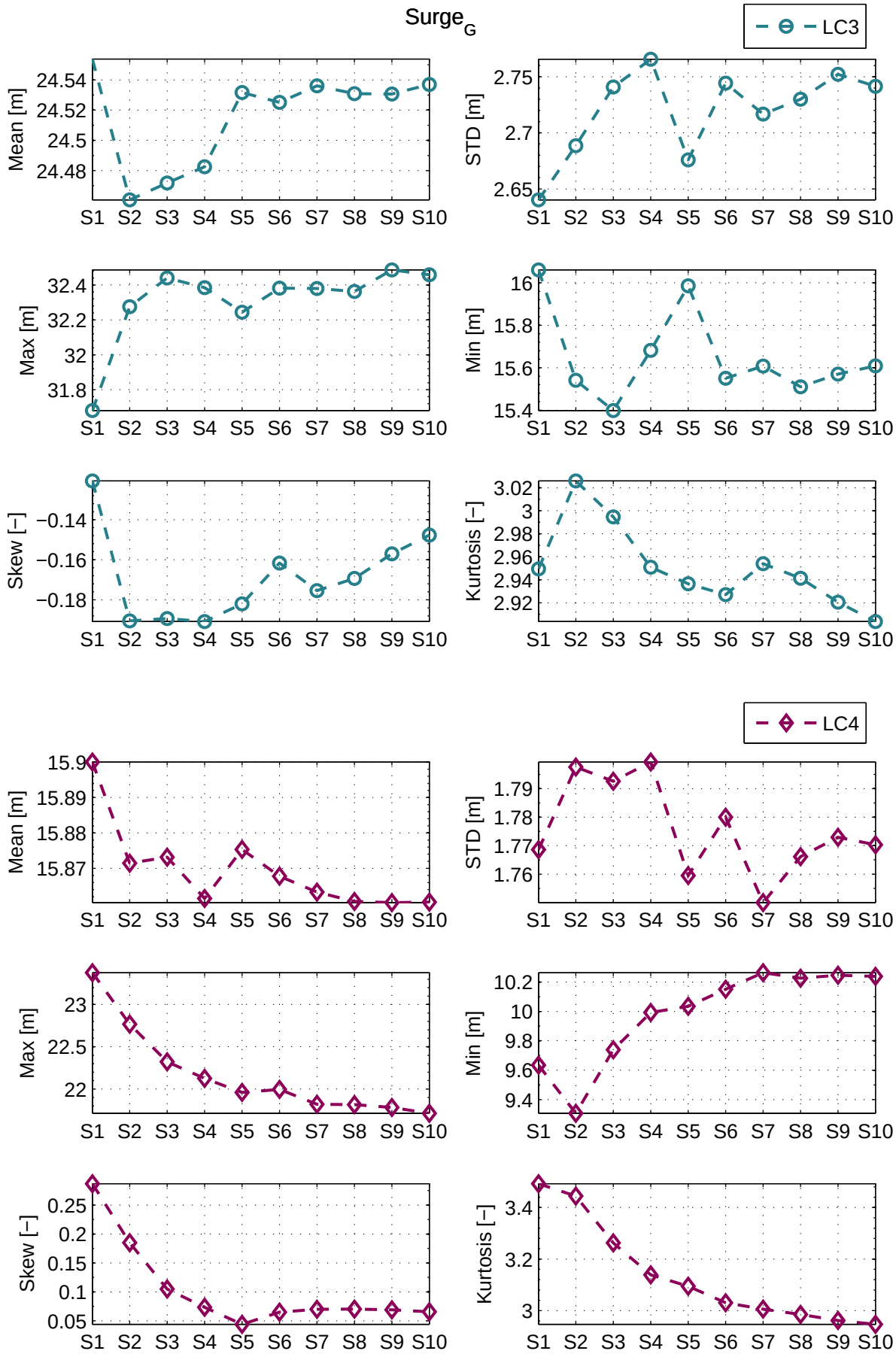
Surge_G
LC3
Mean [m]
24.54
24.52
24.5
24.48
STD [m]
2.75
2.7
2.65
Max [m]
32.4
32.2
32
31.8
Min [m]
16
15.8
15.6
15.4
Skew [–]
−0.14
−0.16
−0.18
Kurtosis [–]
3.02
3
2.98
2.96
2.94
2.92
S1 S2 S3 S4 S5 S6 S7 S8 S9 S10
LC4
Mean [m]
15.9
15.89
15.88
15.87
STD [m]
1.79
1.78
1.77
1.76
Max [m]
23
22.5
22
Min [m]
10.2
10
9.8
9.6
9.4
Skew [–]
0.25
0.2
0.15
0.1
0.05
Kurtosis [–]
3.4
3.2
3

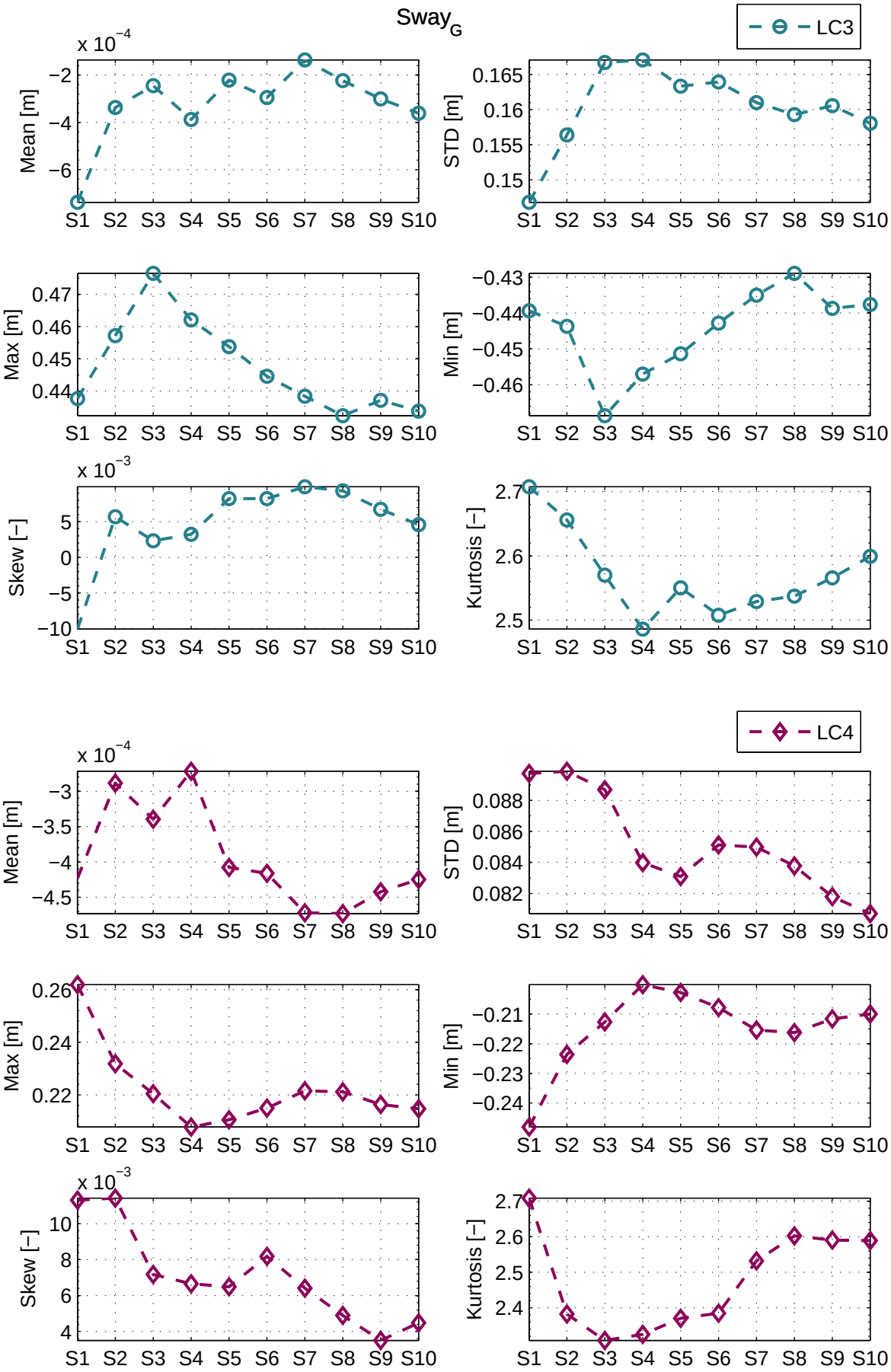
Sway_G
LC3
LC4
Mean [m]
STD [m]
Max [m]
Min [m]
Skew [−]
Kurtosis [−]
x 10^−4
x 10^−3
S1 S2 S3 S4 S5 S6 S7 S8 S9 S10

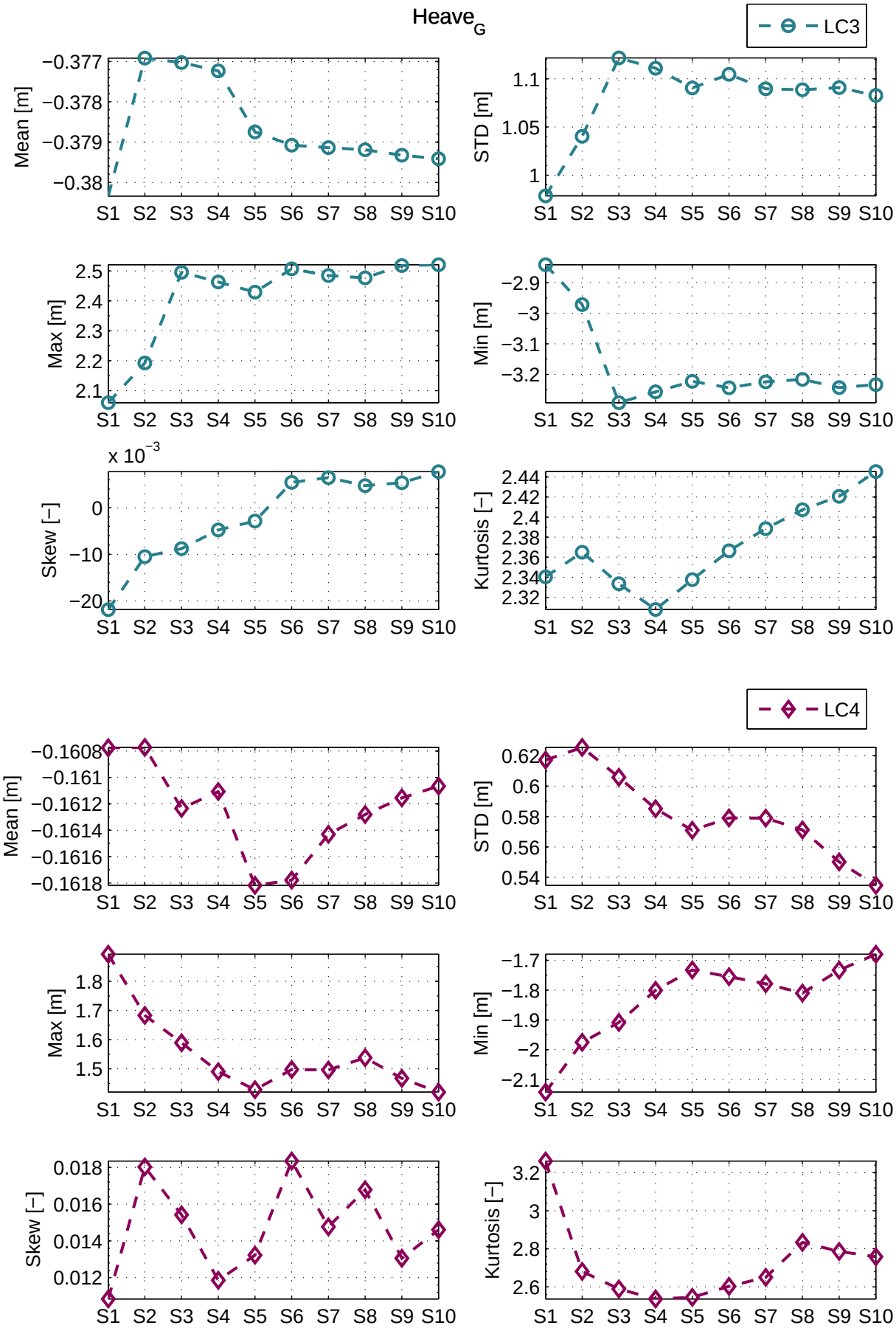
Heave$_G$
LC3
Mean [m]
−0.377
−0.378
−0.379
−0.38
STD [m]
1.1
1.05
1
Max [m]
2.5
2.4
2.3
2.2
2.1
Min [m]
−2.9
−3
−3.1
−3.2
Skew [−]
x 10^{-3}
0
−10
−20
Kurtosis [−]
2.44
2.42
2.4
2.38
2.36
2.34
2.32
S1 S2 S3 S4 S5 S6 S7 S8 S9 S10
LC4
Mean [m]
−0.1608
−0.161
−0.1612
−0.1614
−0.1616
−0.1618
STD [m]
0.62
0.6
0.58
0.56
0.54
Max [m]
1.8
1.7
1.6
1.5
Min [m]
−1.7
−1.8
−1.9
−2
−2.1
Skew [−]
0.018
0.016
0.014
0.012
Kurtosis [−]
3.2
3
2.8
2.6
S1 S2 S3 S4 S5 S6 S7 S8 S9 S10

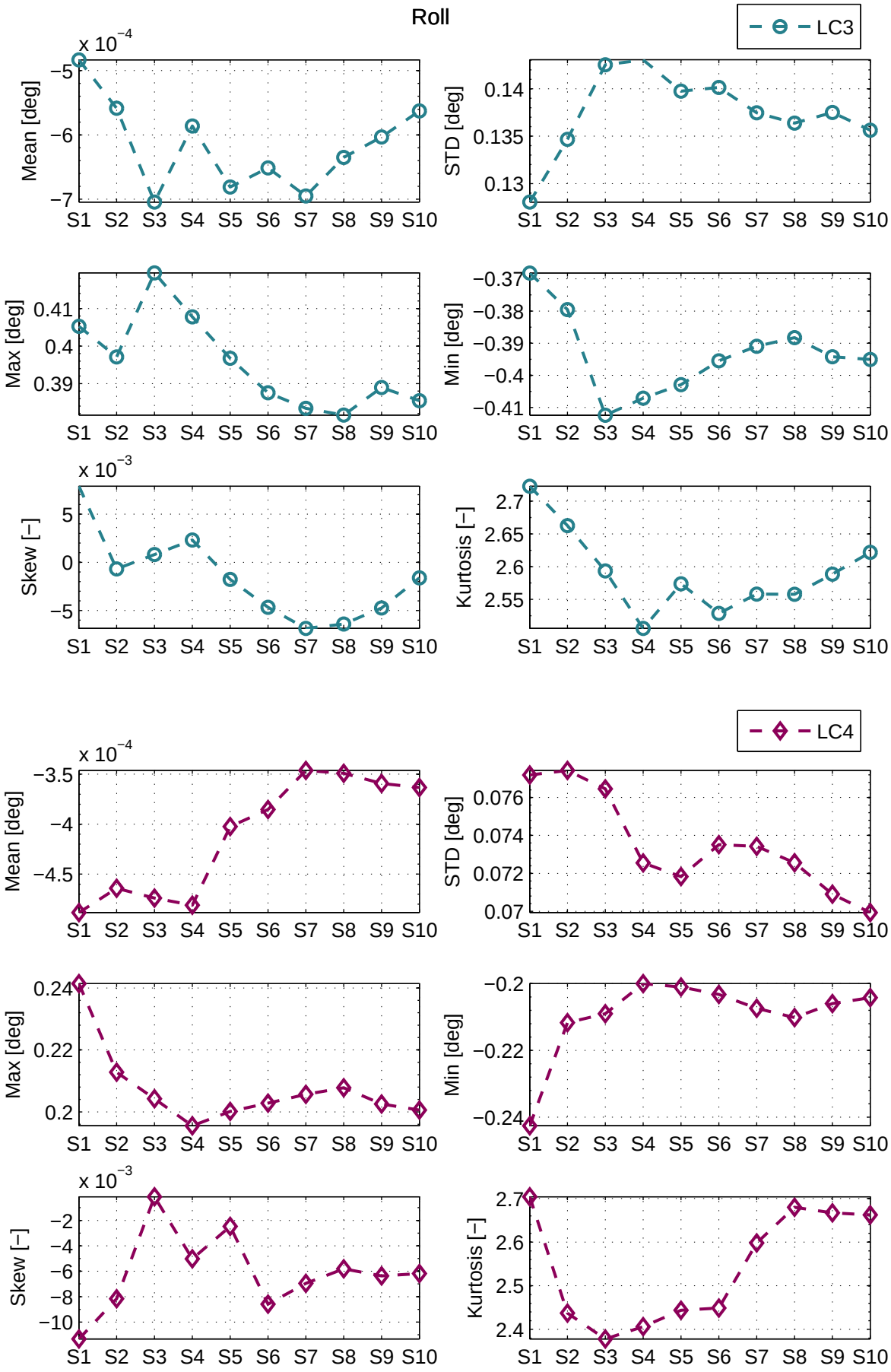
Roll
LC3
LC4
Mean [deg]
STD [deg]
Max [deg]
Min [deg]
Skew [–]
Kurtosis [–]
x 10^-4
x 10^-3
S1 S2 S3 S4 S5 S6 S7 S8 S9 S10

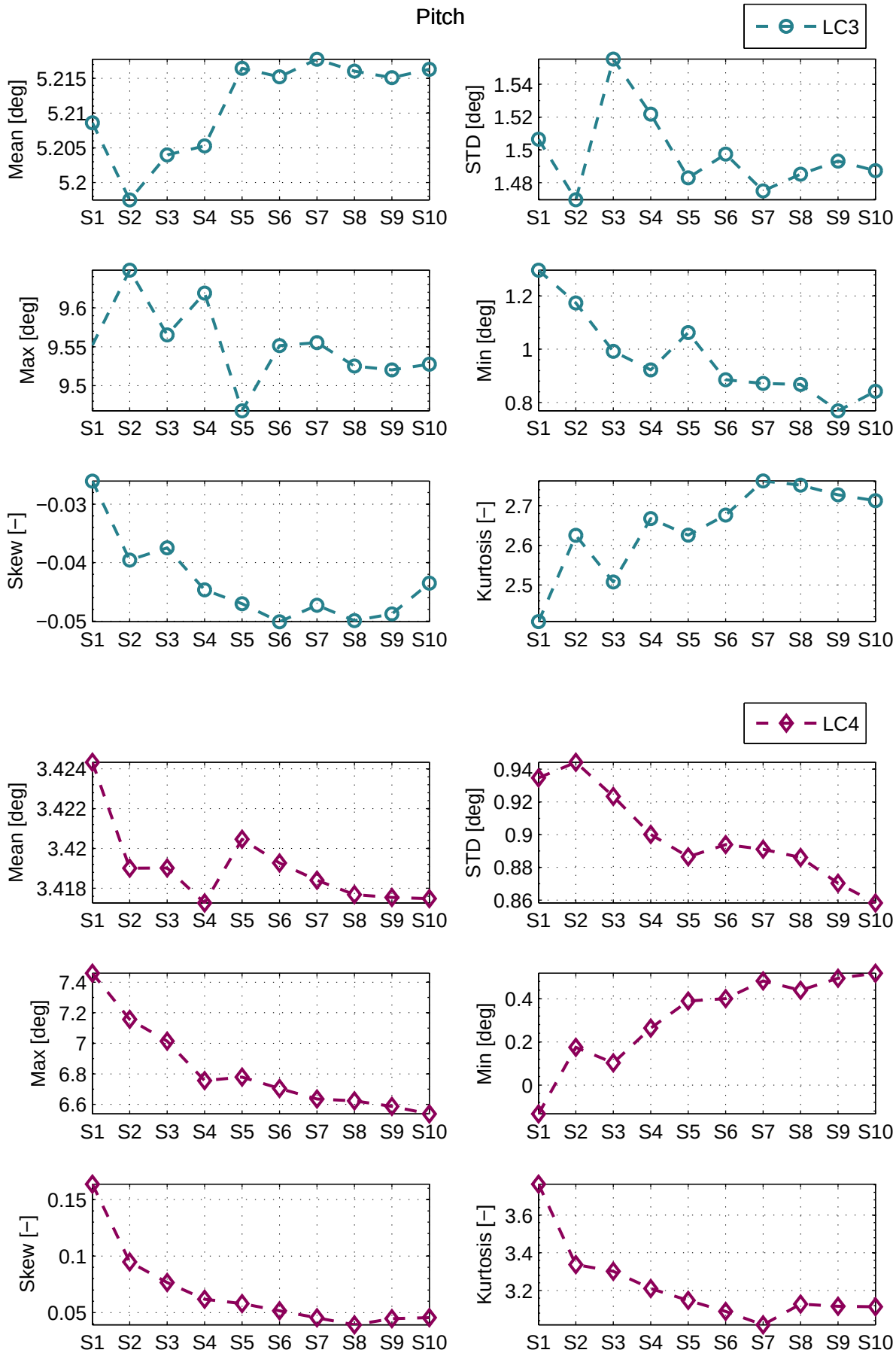
Pitch
LC3
Mean [deg]
5.215
5.21
5.205
5.2
STD [deg]
1.54
1.52
1.5
1.48
Max [deg]
9.6
9.55
9.5
Min [deg]
1.2
1
0.8
Skew [−]
−0.03
−0.04
−0.05
Kurtosis [−]
2.7
2.6
2.5
S1 S2 S3 S4 S5 S6 S7 S8 S9 S10
LC4
Mean [deg]
3.424
3.422
3.42
3.418
STD [deg]
0.94
0.92
0.9
0.88
0.86
Max [deg]
7.4
7.2
7
6.8
6.6
Min [deg]
0.4
0.2
0
Skew [−]
0.15
0.1
0.05
Kurtosis [−]
3.6
3.4
3.2

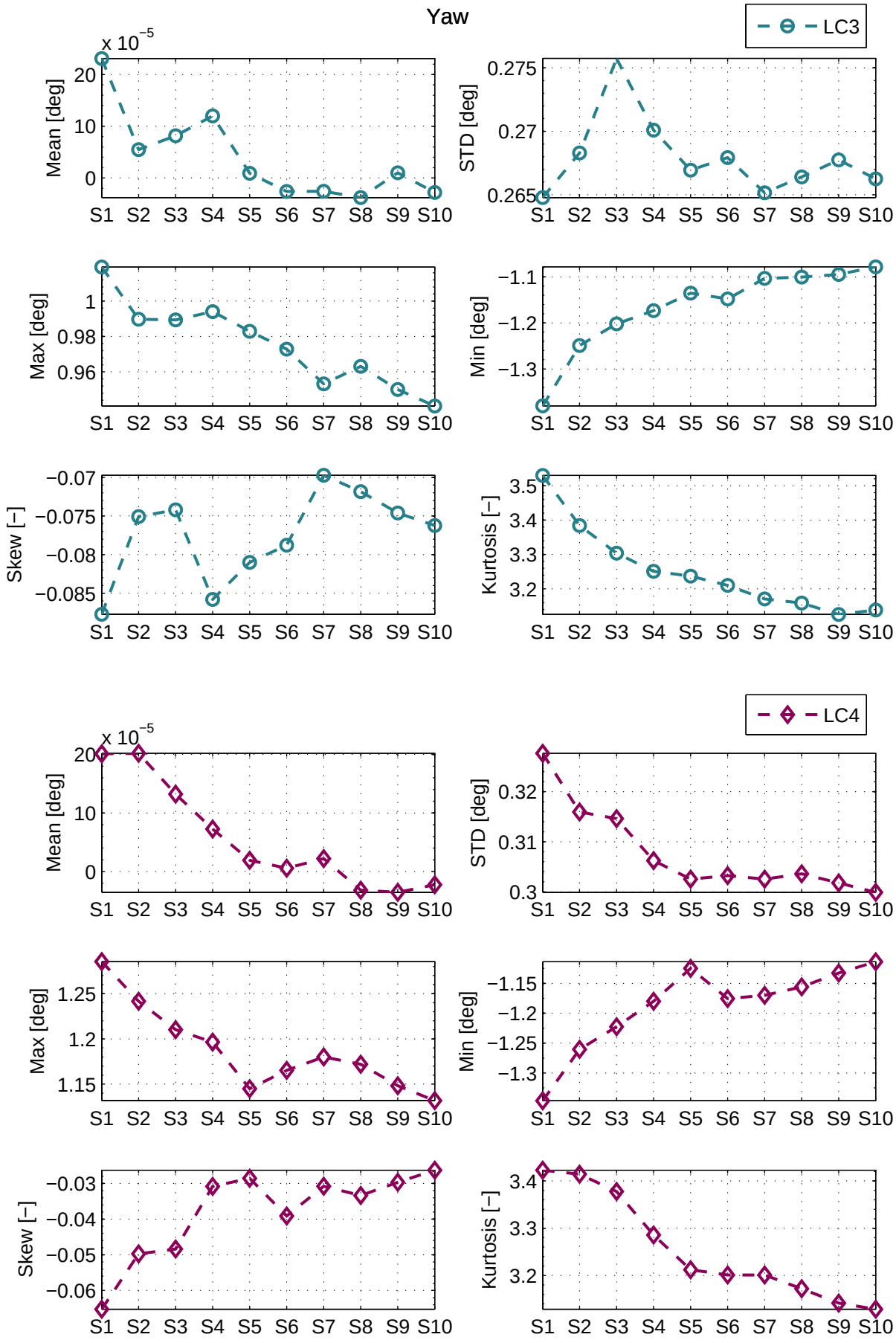
Yaw
LC3
x 10^-5
Mean [deg]
STD [deg]
Max [deg]
Min [deg]
Skew [–]
Kurtosis [–]
LC4
S1 S2 S3 S4 S5 S6 S7 S8 S9 S10

APPENDIX 3

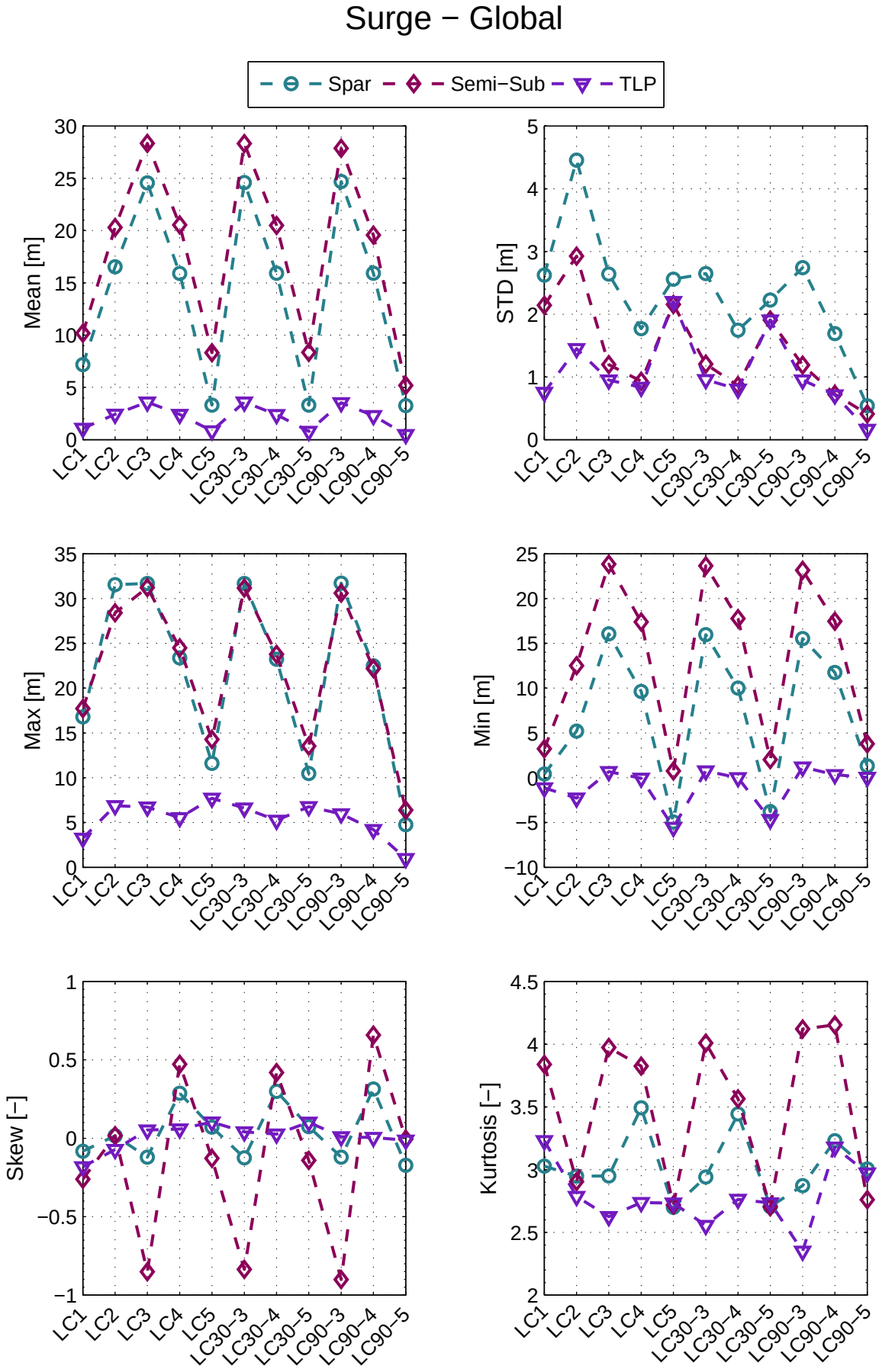
Surge − Global
Spar
Semi−Sub
TLP
Mean [m]
STD [m]
Max [m]
Min [m]
Skew [−]
Kurtosis [−]
LC1
LC2
LC3
LC4
LC5
LC30−3
LC30−4
LC30−5
LC90−3
LC90−4
LC90−5

Sway − Global

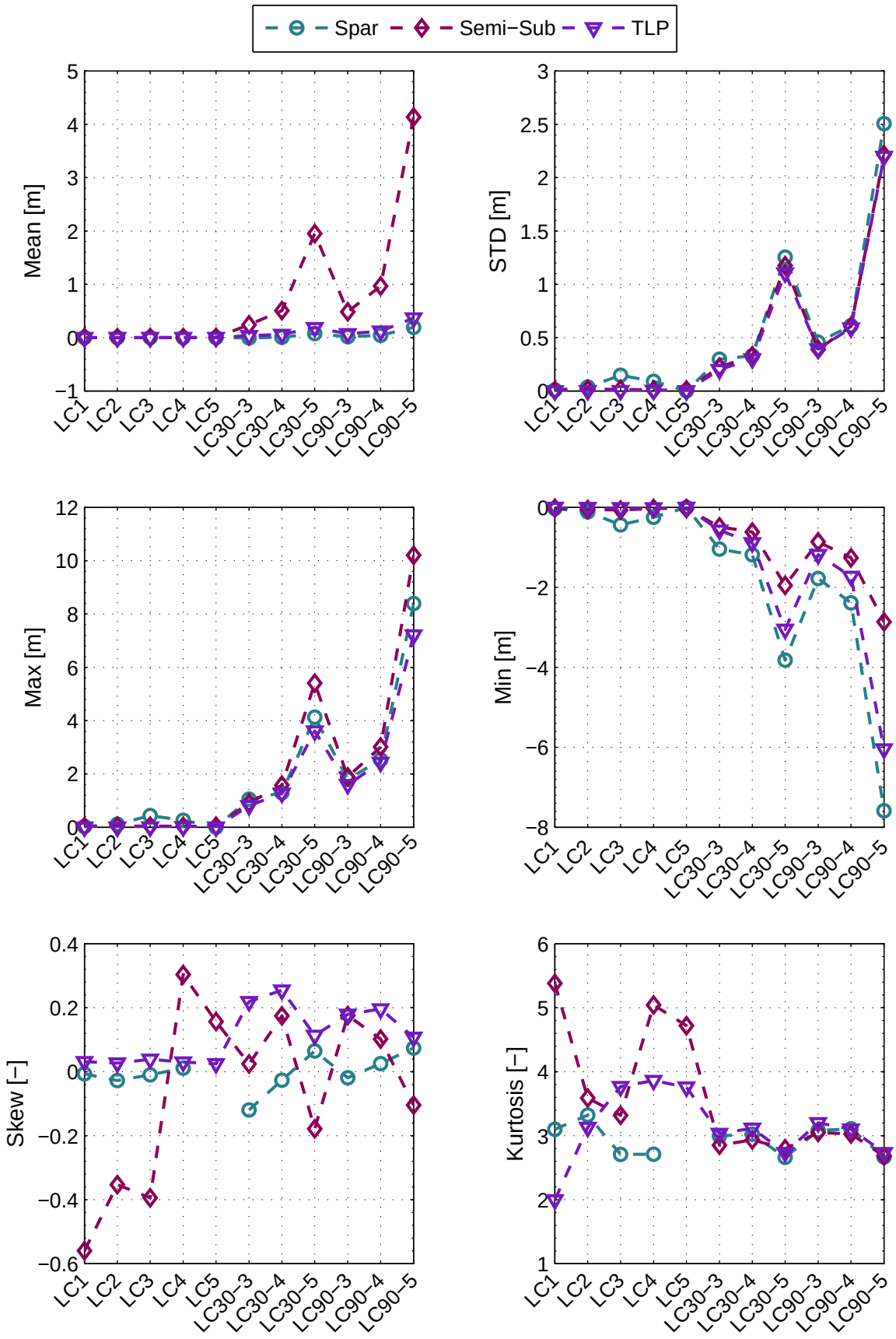
Spar
Semi−Sub
TLP
Mean [m]
STD [m]
Max [m]
Min [m]
Skew [−]
Kurtosis [−]
LC1
LC2
LC3
LC4
LC5
LC30−3
LC30−4
LC30−5
LC90−3
LC90−4
LC90−5

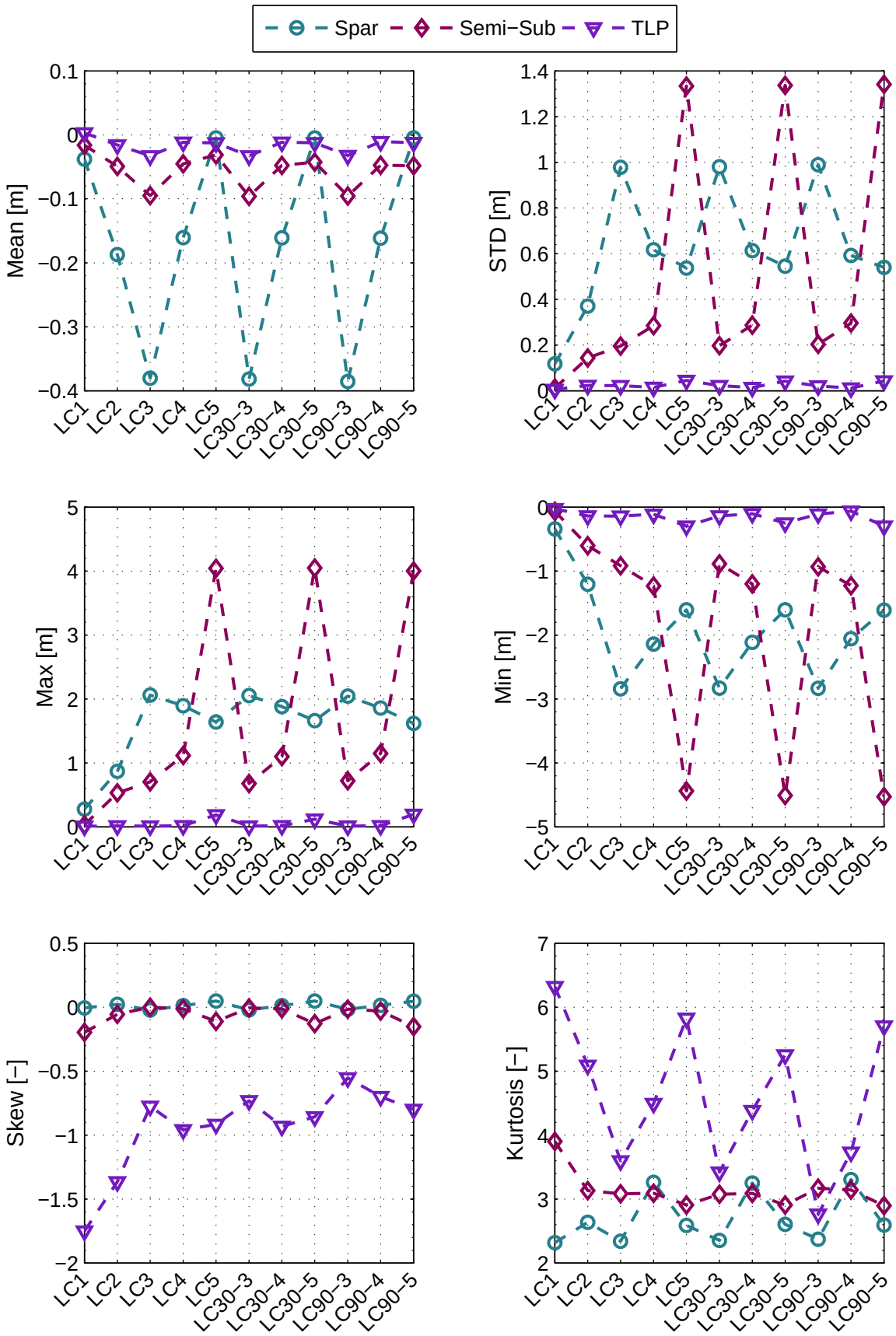
Heave − Global
Spar
Semi−Sub
TLP
Mean [m]
STD [m]
Max [m]
Min [m]
Skew [−]
Kurtosis [−]
LC1
LC2
LC3
LC4
LC5
LC30−3
LC30−4
LC30−5
LC90−3
LC90−4
LC90−5

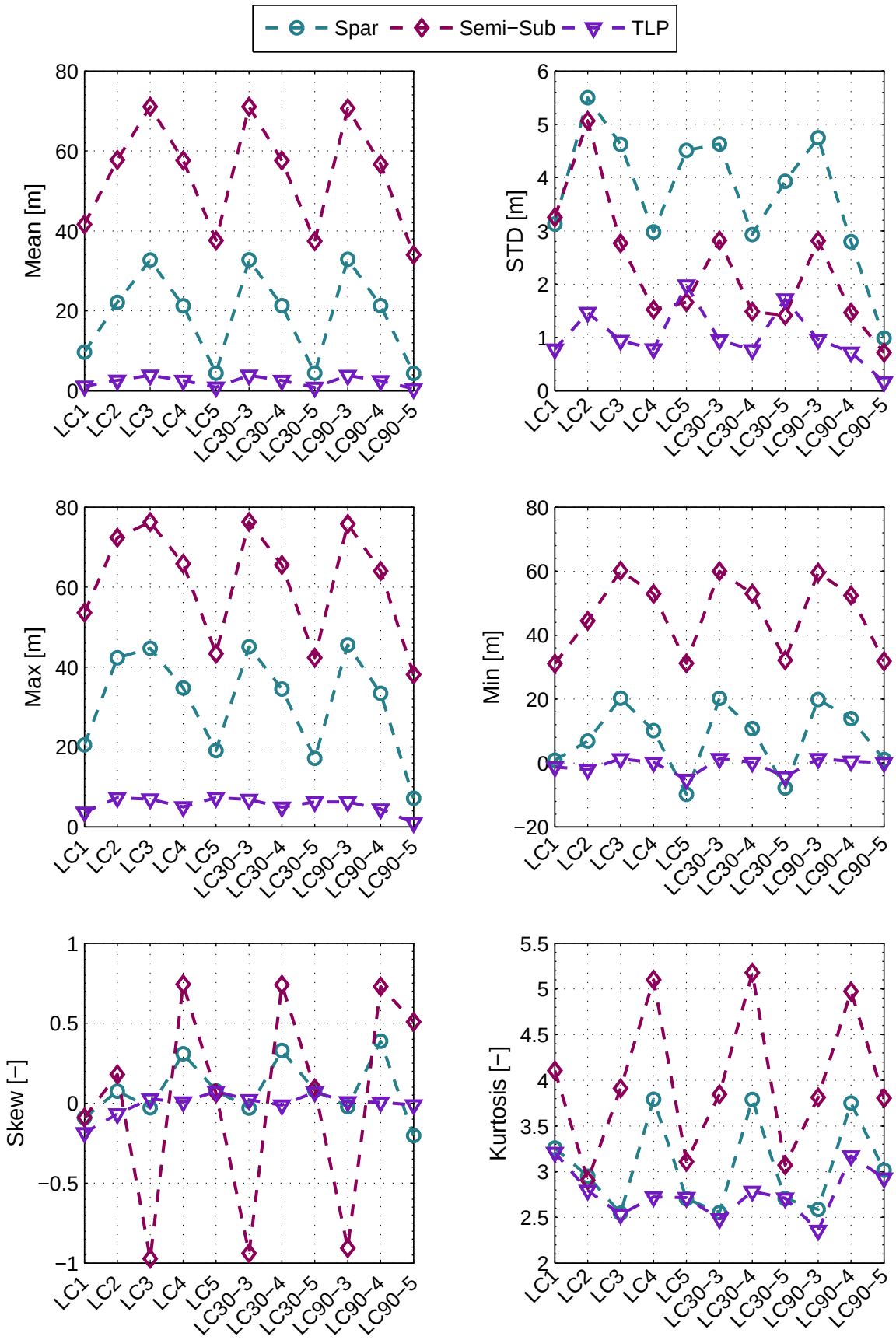
Surge − Nacelle
Spar
Semi−Sub
TLP
Mean [m]
STD [m]
Max [m]
Min [m]
Skew [−]
Kurtosis [−]
LC1
LC2
LC3
LC4
LC5
LC30−3
LC30−4
LC30−5
LC90−3
LC90−4
LC90−5

Sway − Nacelle

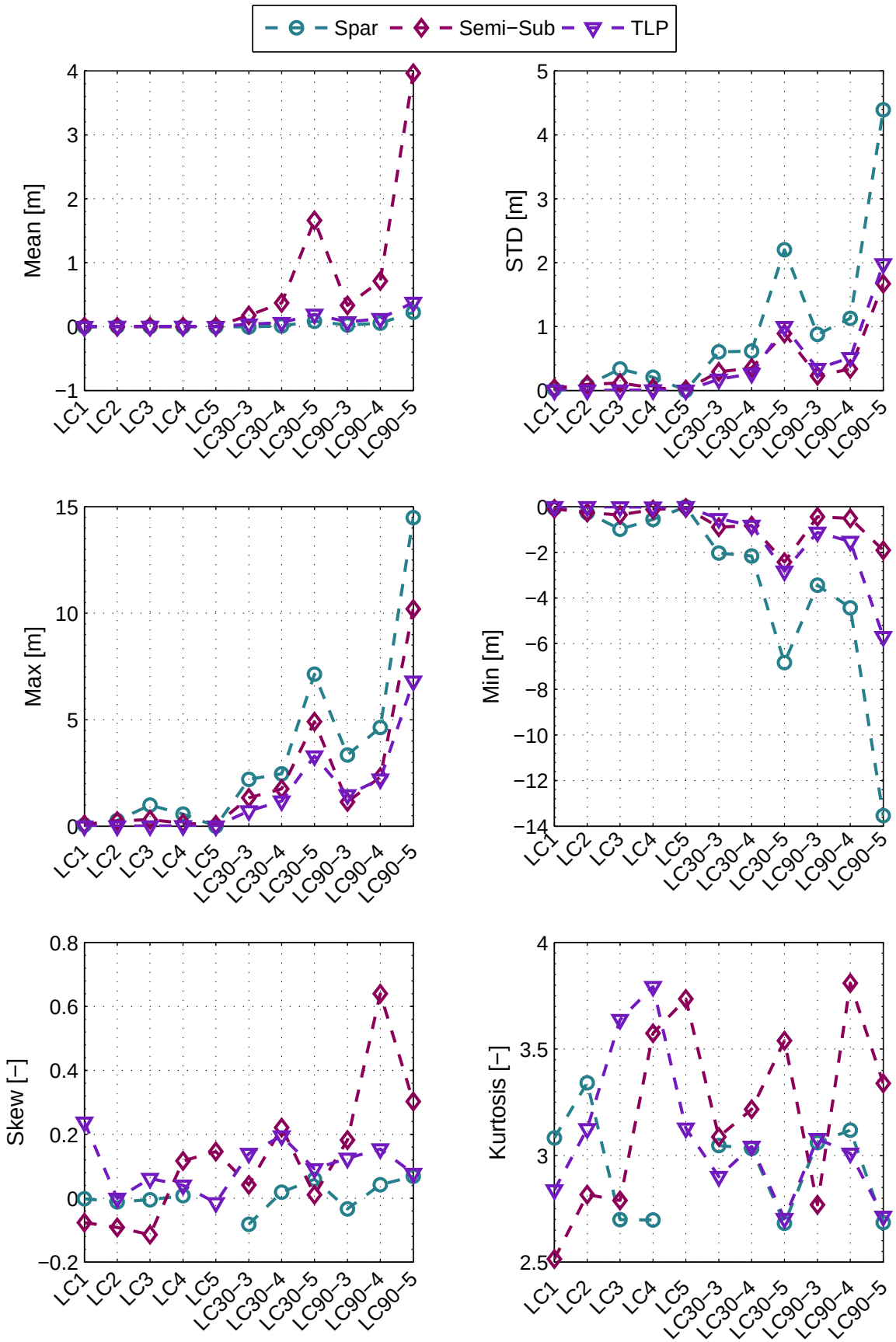

Roll

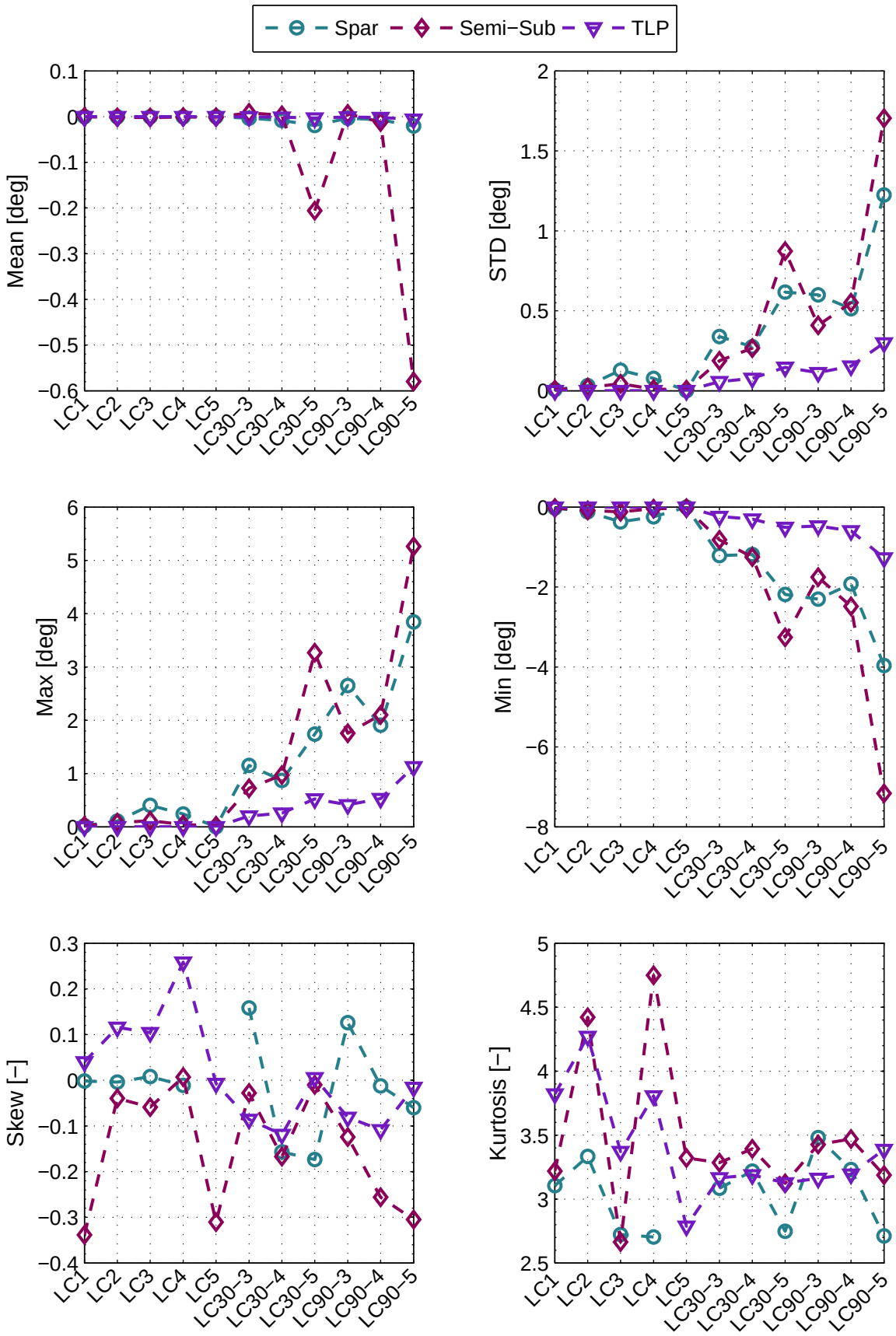
Spar
Semi−Sub
TLP
Mean [deg]
STD [deg]
Max [deg]
Min [deg]
Skew [−]
Kurtosis [−]
LC1
LC2
LC3
LC4
LC5
LC30−3
LC30−4
LC30−5
LC90−3
LC90−4
LC90−5

Pitch

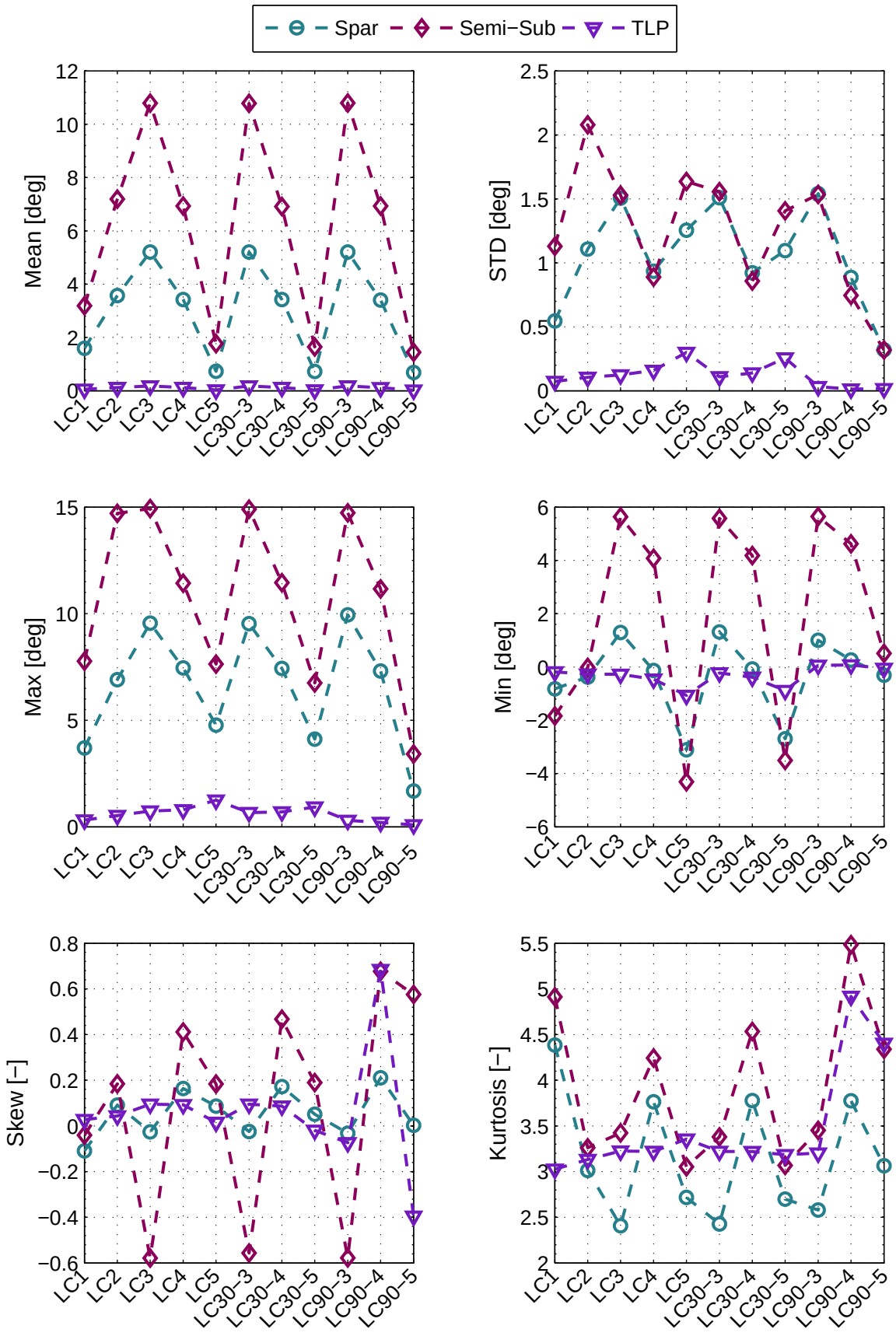
Spar
Semi−Sub
TLP
Mean [deg]
STD [deg]
Max [deg]
Min [deg]
Skew [−]
Kurtosis [−]
LC1
LC2
LC3
LC4
LC5
LC30−3
LC30−4
LC30−5
LC90−3
LC90−4
LC90−5

Yaw

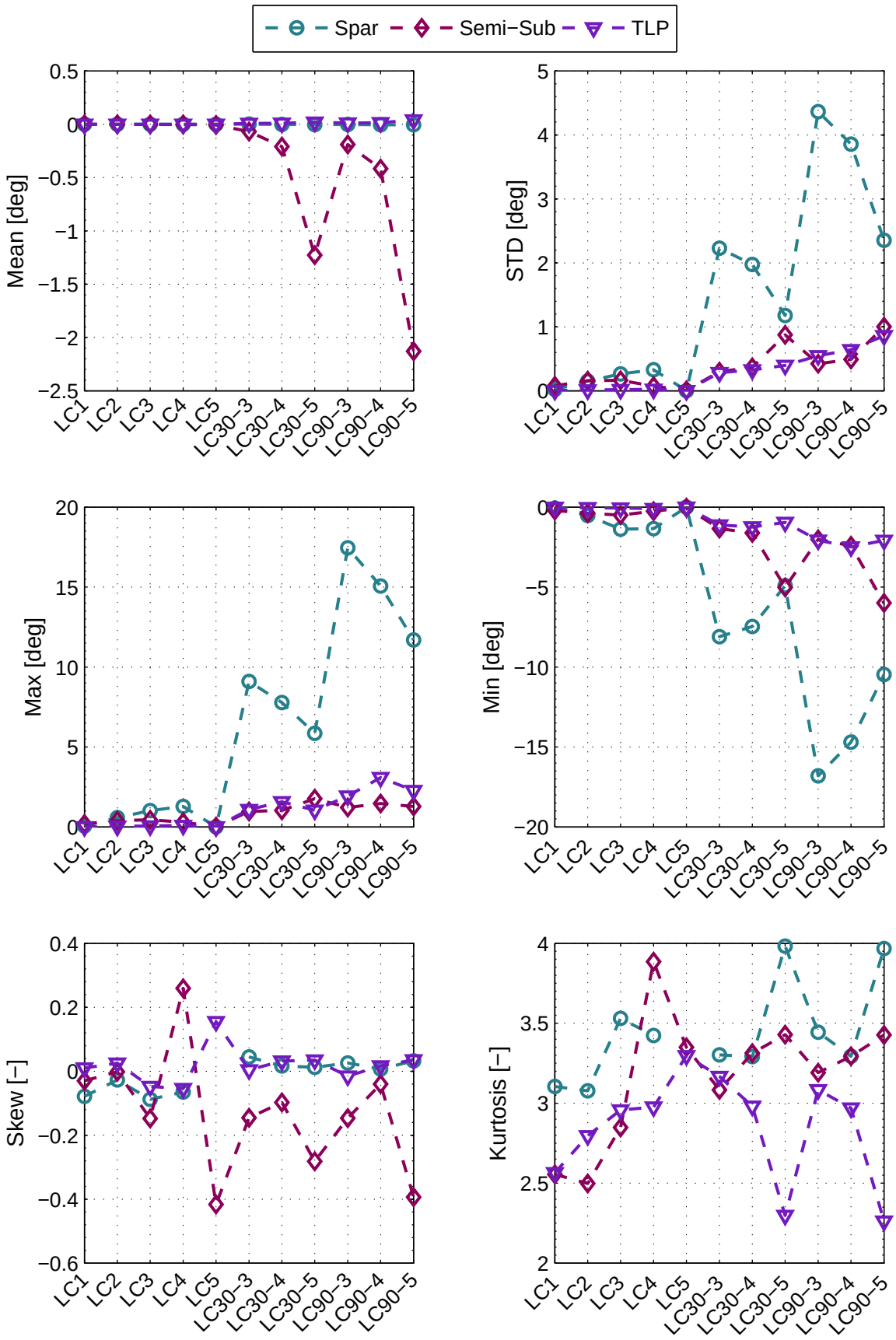
Spar
Semi−Sub
TLP
Mean [deg]
STD [deg]
Max [deg]
Min [deg]
Skew [−]
Kurtosis [−]
LC1
LC2
LC3
LC4
LC5
LC30−3
LC30−4
LC30−5
LC90−3
LC90−4
LC90−5

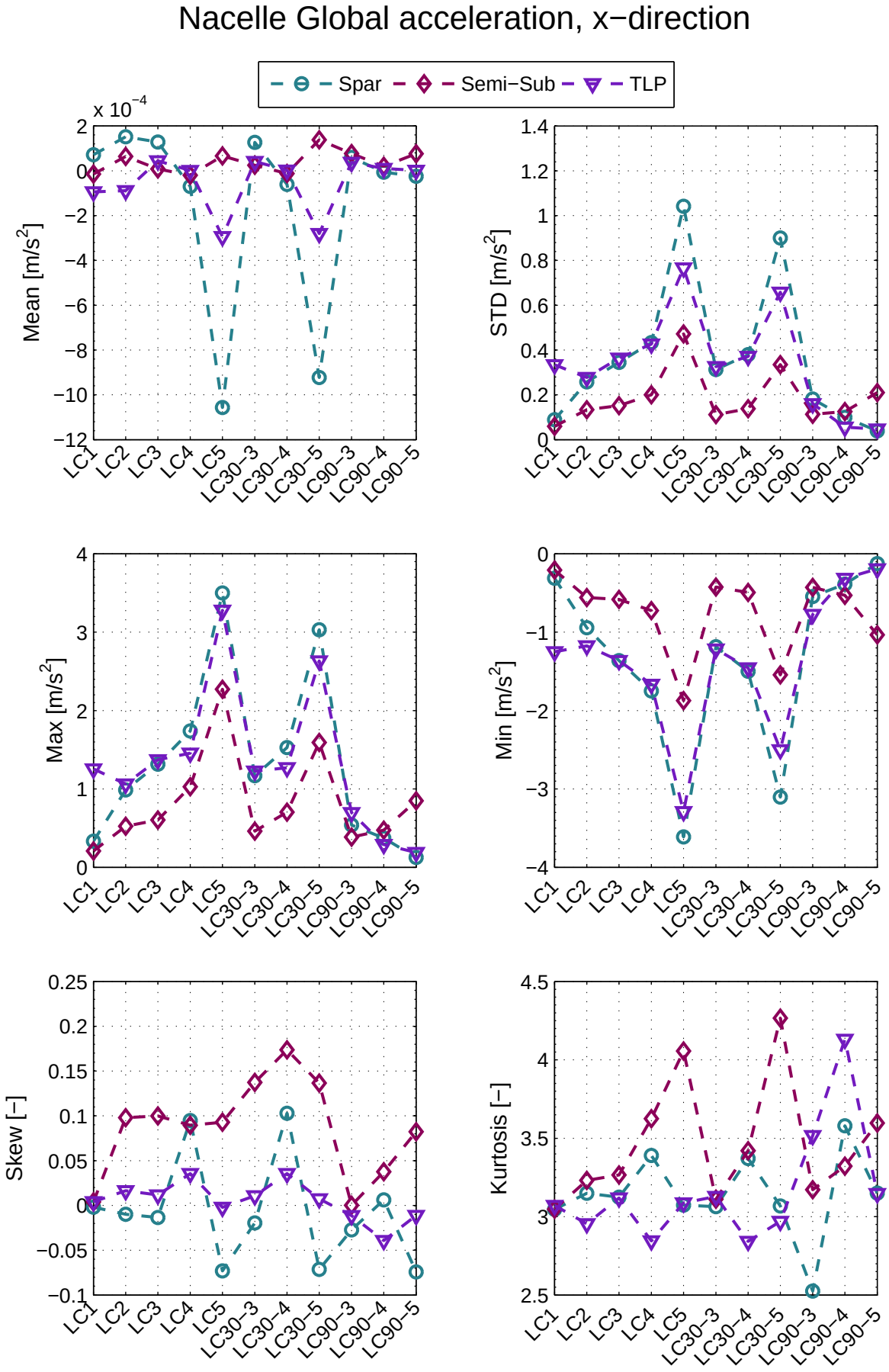
Nacelle Global acceleration, x−direction
Spar
Semi−Sub
TLP
x 10^−4
Mean [m/s^2]
STD [m/s^2]
Max [m/s^2]
Min [m/s^2]
Skew [−]
Kurtosis [−]
LC1
LC2
LC3
LC4
LC5
LC30−3
LC30−4
LC30−5
LC90−3
LC90−4
LC90−5

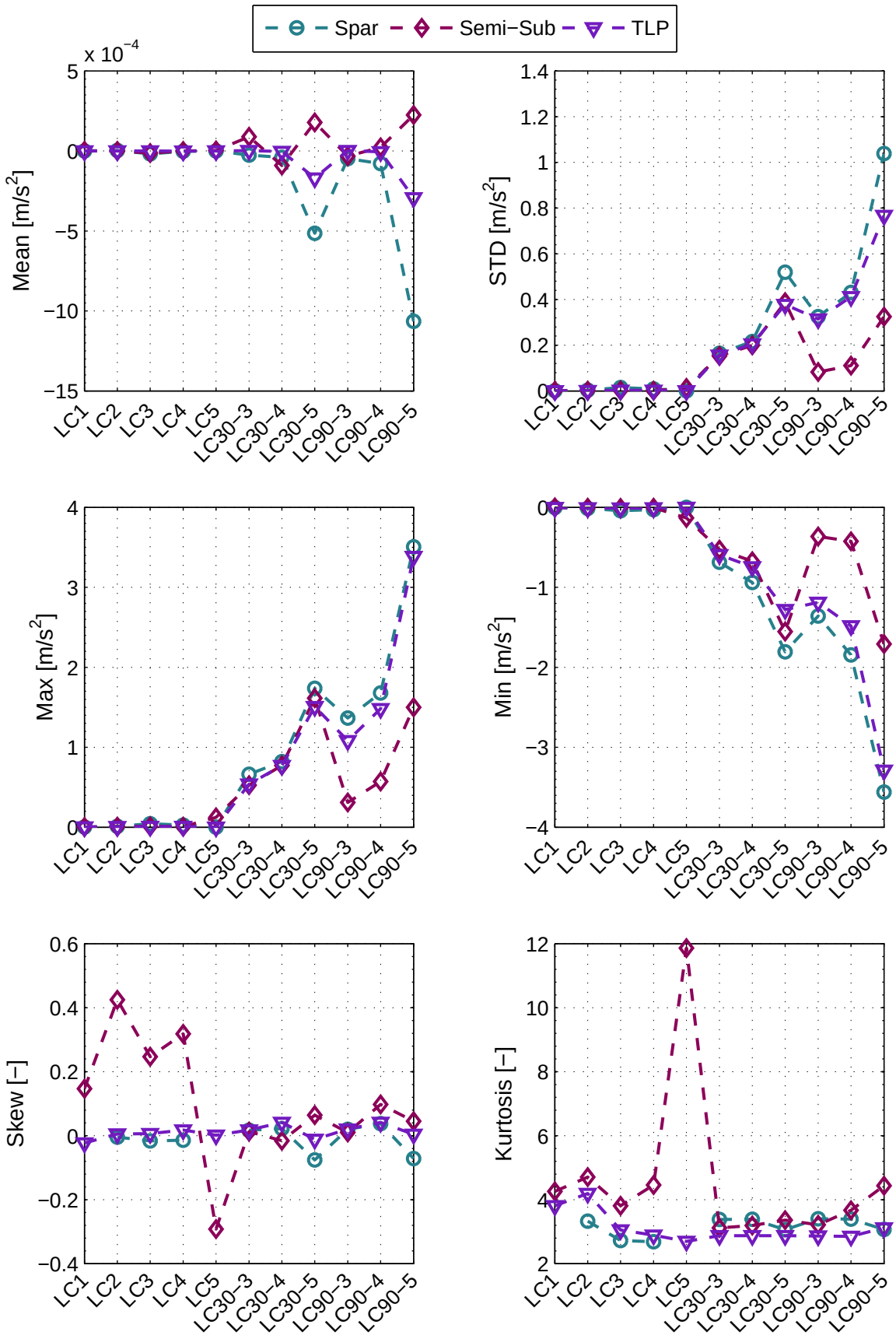
Nacelle Global acceleration, y−direction
Spar
Semi−Sub
TLP
x 10^−4
Mean [m/s^2]
STD [m/s^2]
Max [m/s^2]
Min [m/s^2]
Skew [−]
Kurtosis [−]
LC1
LC2
LC3
LC4
LC5
LC30−3
LC30−4
LC30−5
LC90−3
LC90−4
LC90−5

Wind speed

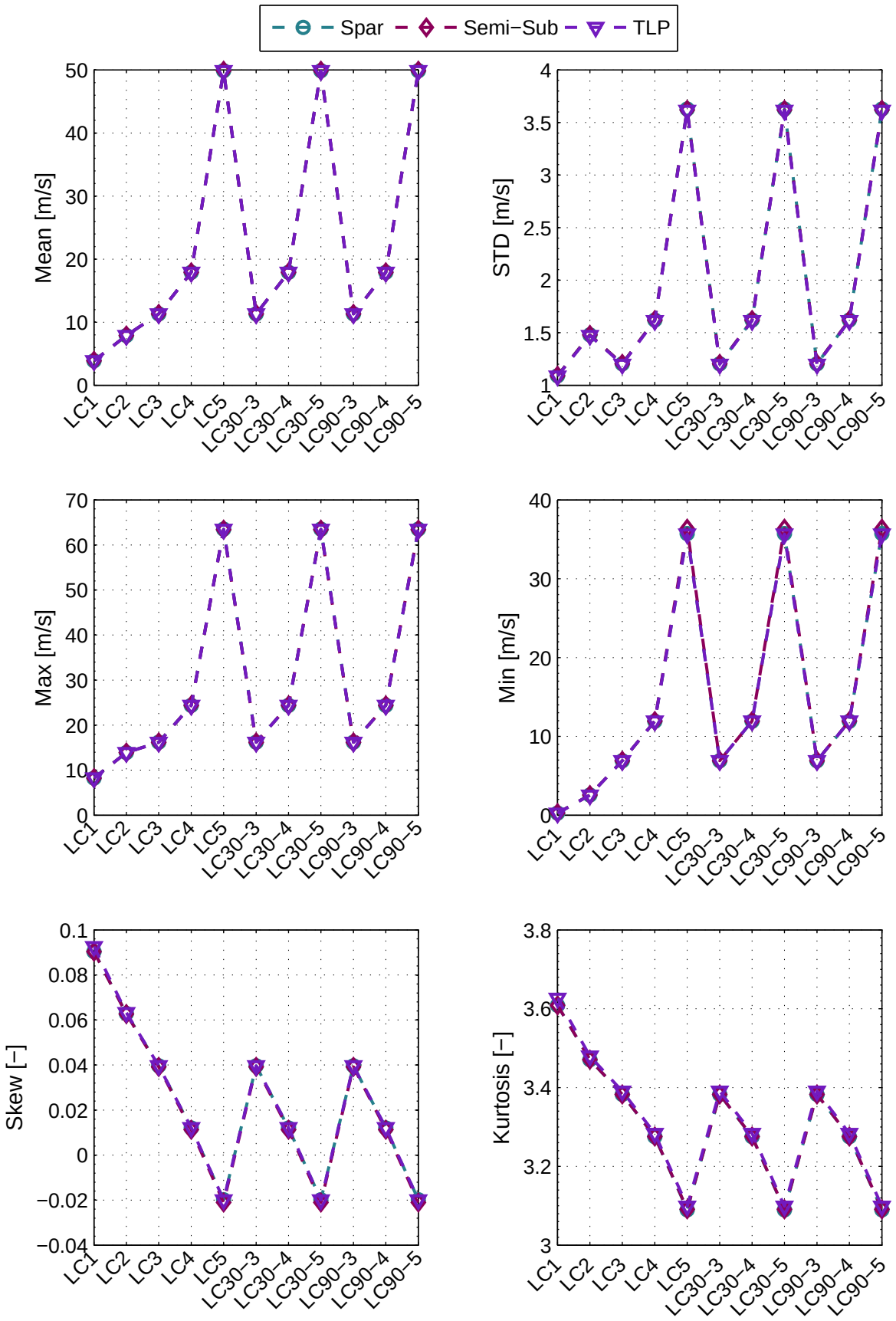
Spar
Semi−Sub
TLP
Mean [m/s]
STD [m/s]
Max [m/s]
Min [m/s]
Skew [−]
Kurtosis [−]
LC1
LC2
LC3
LC4
LC5
LC30−3
LC30−4
LC30−5
LC90−3
LC90−4
LC90−5

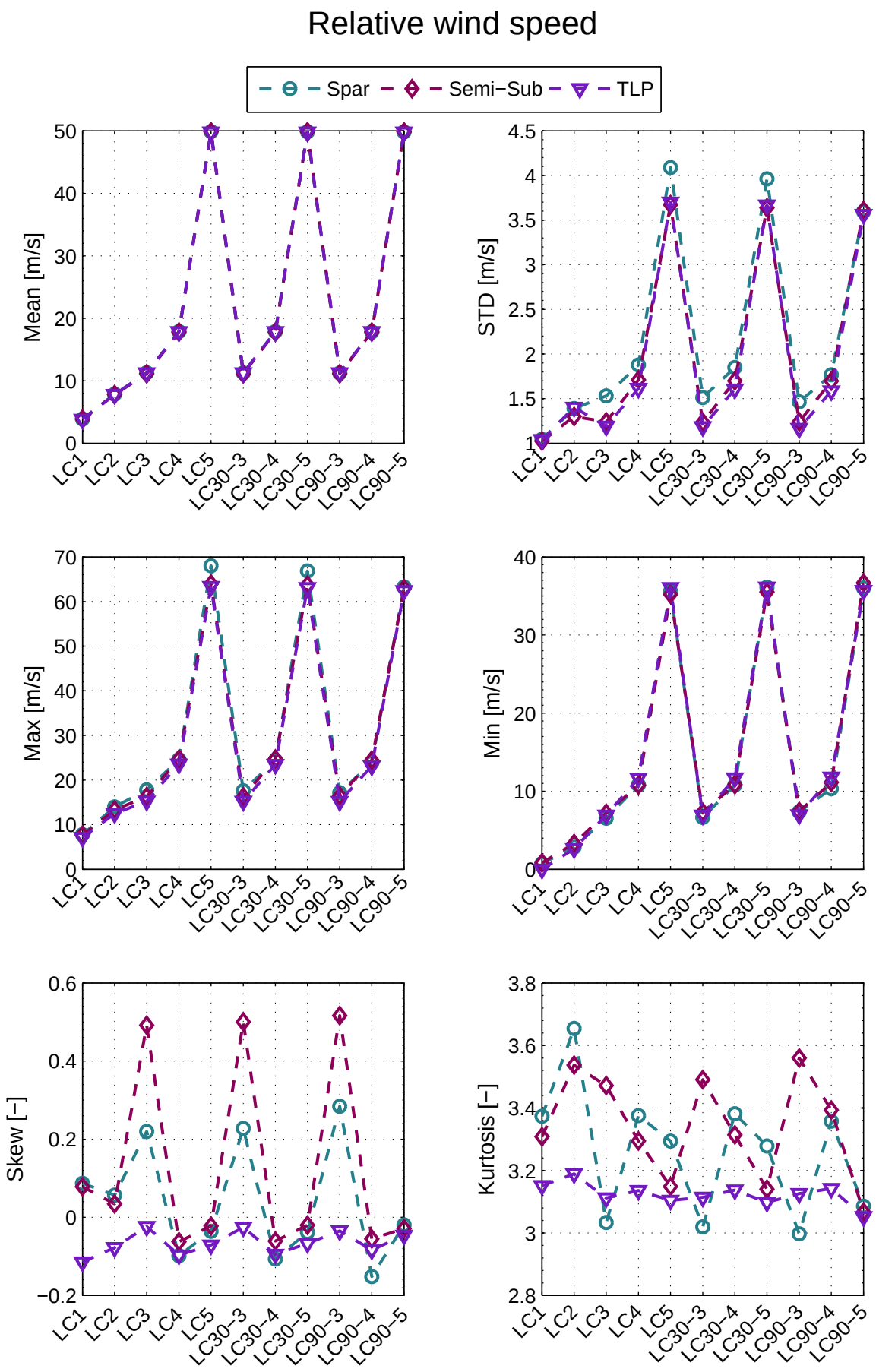
Relative wind speed
Spar
Semi−Sub
TLP
Mean [m/s]
STD [m/s]
Max [m/s]
Min [m/s]
Skew [−]
Kurtosis [−]
LC1
LC2
LC3
LC4
LC5
LC30−3
LC30−4
LC30−5
LC90−3
LC90−4
LC90−5

Filtered relative wind speed

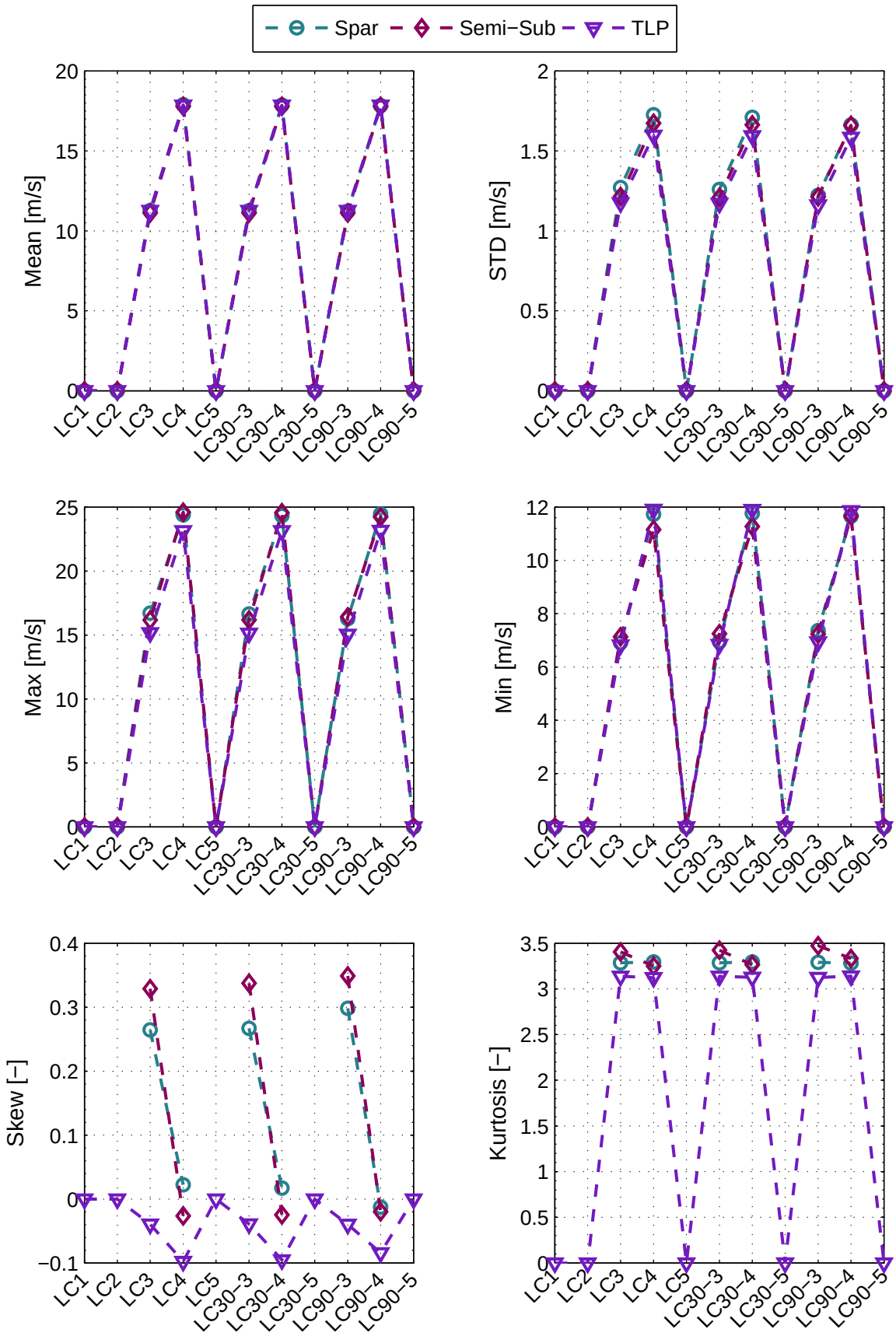

Thrust

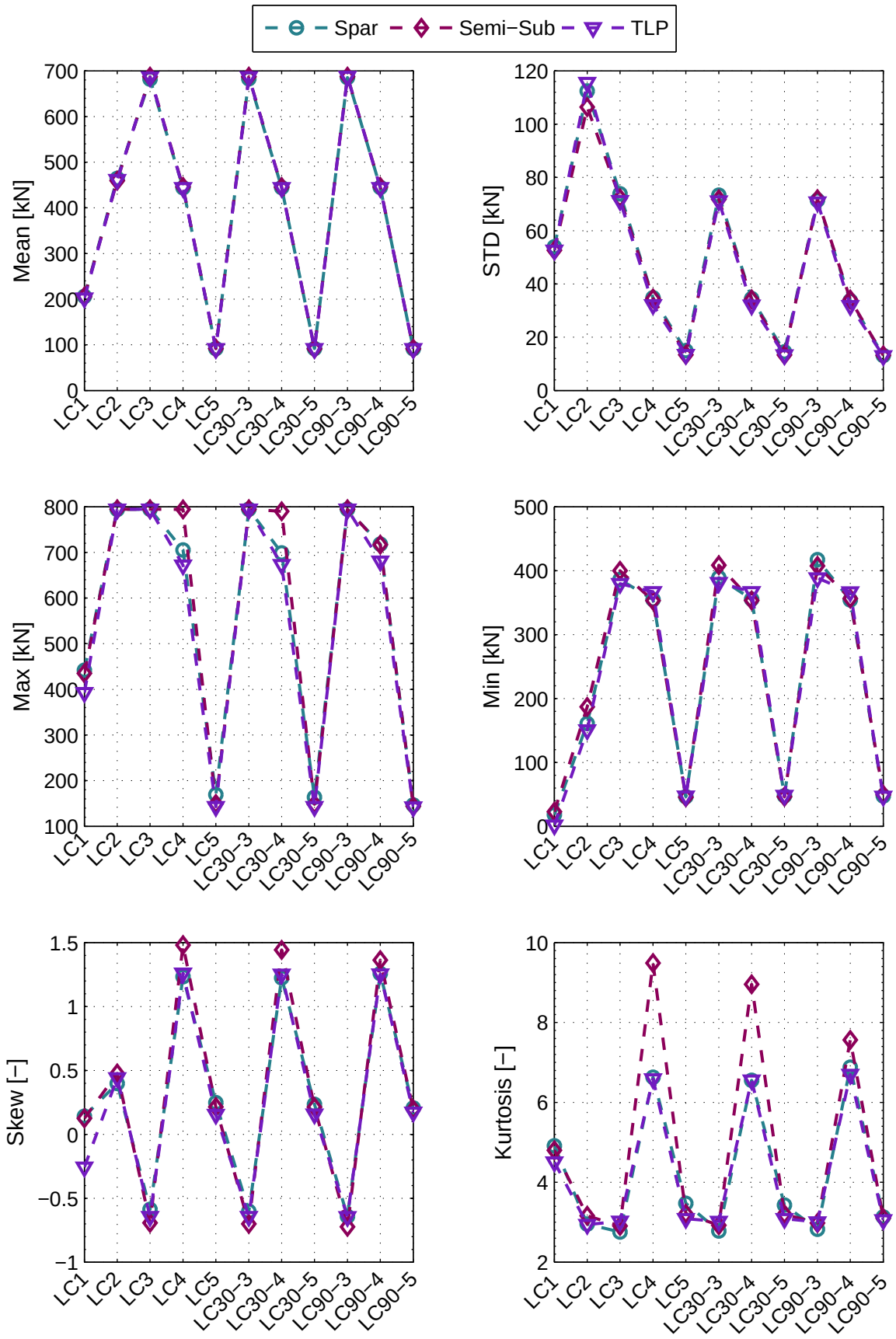
Spar
Semi−Sub
TLP
Mean [kN]
STD [kN]
Max [kN]
Min [kN]
Skew [−]
Kurtosis [−]
LC1
LC2
LC3
LC4
LC5
LC30−3
LC30−4
LC30−5
LC90−3
LC90−4
LC90−5

Power

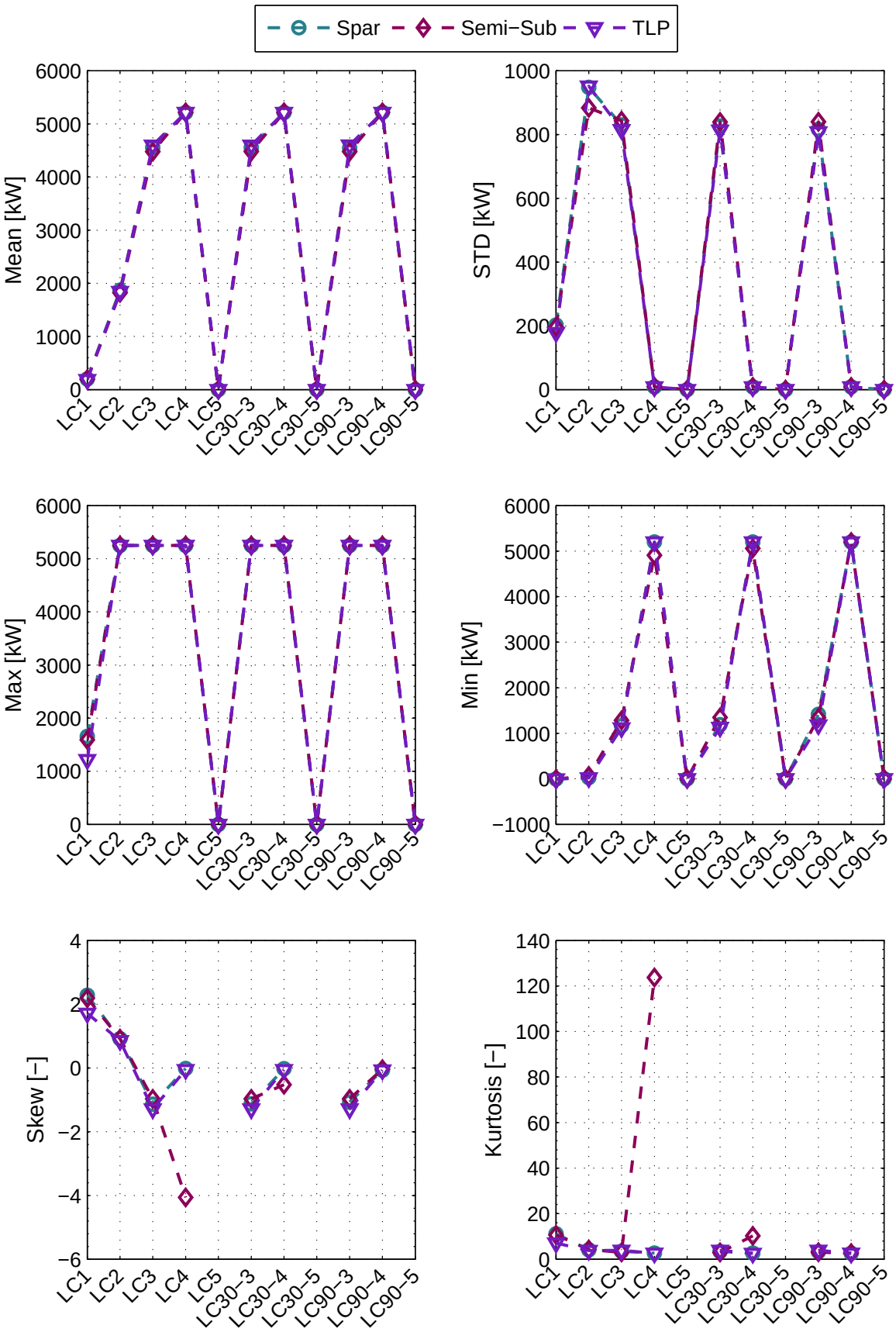
Spar
Semi−Sub
TLP
Mean [kW]
STD [kW]
Max [kW]
Min [kW]
Skew [−]
Kurtosis [−]
LC1
LC2
LC3
LC4
LC5
LC30−3
LC30−4
LC30−5
LC90−3
LC90−4
LC90−5

Tension Line #1

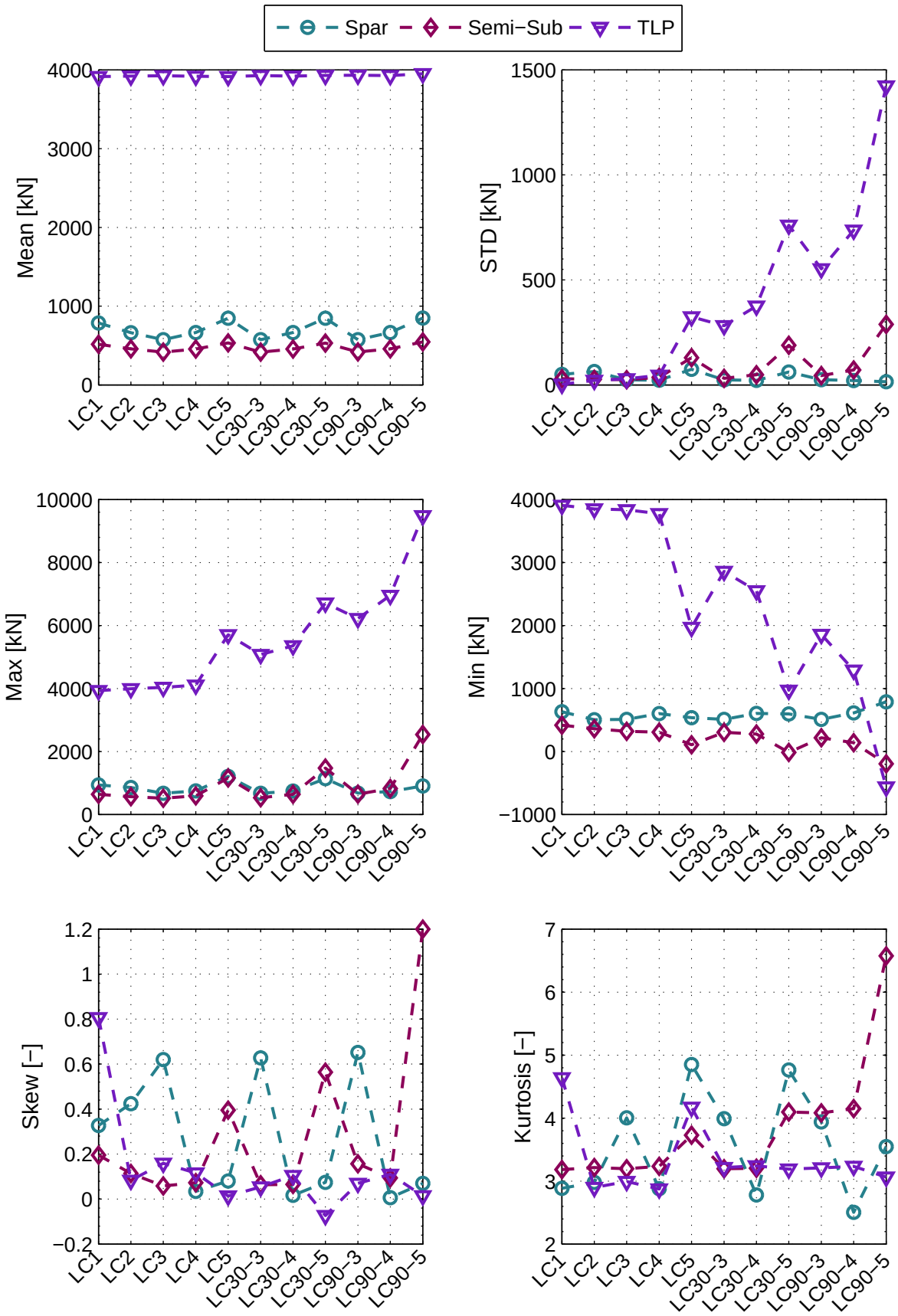

Tension Line #2